EVAPORATION AND DISINTEGRATION OF HEATED THIN LIQUID SHEETS

A Thesis
Presented to
The Academic Faculty

by

Aaron W. Howell

In Partial Fulfillment
of the Requirements for the Degree
Doctor of Philosophy in
Mechanical Engineering

George W. Woodruff School of Mechanical Engineering
Georgia Institute of Technology
August 2015

EVAPORATION AND DISINTEGRATION OF HEATED THIN LIQUID SHEETS

Approved by:

Dr. Cyrus K. Aidun, Advisor
George W. Woodruff School of
Mechanical Engineering
Georgia Institute of Technology

Dr. Marc K. Smith
George W. Woodruff School of
Mechanical Engineering
Georgia Institute of Technology

Dr. Yogendra Joshi
George W. Woodruff School of
Mechanical Engineering
Georgia Institute of Technology

Dr. Preet Singh
Material Science & Engineering
Georgia Institute of Technology

Dr. Richard Vuduc
Computational Science & Engineering
Georgia Institute of Technology

Date Approved: May 11, 2015

ACKNOWLEDGEMENTS

I would like to express my sincere gratitude to my advisor Dr. Aidun for the continuous guidance and insight through my Ph.D. study and research. I am grateful to the Renewable Bioproducts Institute for the Paper Science and Engineering Fellowship which provided funding for this project. And final thanks to my wife, Erin, for her patience, help, and encouragement.

TABLE OF CONTENTS

ACKNOWLEDGEMENTS . . . . **iii**

LIST OF TABLES . . . . **vii**

LIST OF FIGURES . . . . **viii**

LIST OF SYMBOLS OR ABBREVIATIONS . . . . **xiii**

SUMMARY . . . . **xvii**

1 INTRODUCTION **1**

1.1 Motivation 3

1.2 Falling Film 5

1.3 Liquid Curtain 7

1.3.1 Hydrodynamics 7

1.3.2 Stability 7

1.3.3 Breakup 8

1.3.4 Heat Transfer 9

1.4 Outline 11

2 RESEARCH METHODOLOGY **12**

2.1 Numerical Setup 12

2.1.1 Governing equations 13

2.1.2 Surface Evaporation 15

2.1.3 Black Liquor Properties 16

2.1.4 Boundary Conditions 20

3 NUMERICAL IMPLEMENTATION **22**

3.1 Numerical Algorithm 22

3.1.1 Discretization of PDEs 22

3.1.2 Boundary Conditions 25

3.1.3 PISO Algorithm 26

3.2 Liquid Curtain Mesh 27
3.3 Validation Cases 28
    3.3.1 Film Hydrodynamics 28
    3.3.2 Surface Evaporation Model 30
4 FALLING FILM EVAPORATION 33
4.1 Background 33
4.2 Mathematical Model 34
    4.2.1 Important Parameters 36
    4.2.2 Boundary Conditions 38
4.3 Numerical Validation 39
    4.3.1 Heat Transfer Coefficient 40
4.4 Analysis of Simulation Results 42
    4.4.1 Streamwise Film Temperatures 42
    4.4.2 Film Evaporation 47
    4.4.3 Black Liquor Falling Film 53
        4.4.3.1 Effect of Dry Solids 54
    4.4.4 Solitary Wave Temperature Profile 57
        4.4.4.1 Temperature Profile 62
        4.4.4.2 Evaporation Rate 64
5 LIQUID CURTAIN EVAPORATION 68
5.1 Background 68
5.2 Mathematical Model 69
    5.2.1 Important Parameters 70
    5.2.2 Boundary Conditions 73
5.3 Numerical Validation 73
    5.3.1 Velocity Profile of Liquid Curtain 74
    5.3.2 Heated Liquid Curtain Thermal Profile 79
5.4 Analysis of Simulation Results 81

5.4.1 Curtain Breakup 81
5.4.2 Heat Transfer from Surrounding Gas 84
5.4.3 Black Liquor Liquid Curtain 90
5.4.3.1 Effect of Dry Solids 90
5.4.3.2 Evaporation Rate 90
6 COMPARISON OF EVAPORATION METHODS 95
6.1 Background 95
6.2 Evaporator Comparison 95
6.3 3-D Effects 101
7 CONCLUSIONS 104
7.1 Conclusions 104
7.1.1 Falling Film Evaporation 104
7.1.2 Liquid Curtain Heat Transfer and Evaporation 105
7.1.3 Comparison of Evaporation Methods 106
7.2 Future Recommendations 107
7.2.1 Exploiting Liquid Curtain Breakup 107
7.2.2 Falling Film Heated by Steam 108
7.2.3 Crystal Fluid-Solid Interaction 108
7.2.4 Crystallization Model 109
REFERENCES 110

LIST OF TABLES

2.1 Parameter values for black liquor series ABAFX011,12 [34]. 18

3.1 Fluid properties used in Stephan problem simulation. 31

4.1 Simulations to study the effect of forcing frequency on the hydrodynamics and temperature of a falling film. 44

4.2 Simulations series to study the effect of dry solids content on black liquor hydrodynamics. 54

4.3 Simulation series to study the effect of dry solids content on black liquor film surface evaporation. 62

4.4 Parameters for cases investigating the effect of non-Newtonian viscosity on heat transfer to a falling film. 64

5.1 Simulations designed to study effect of inlet velocity and gas/liquid velocity ratio on liquid curtain hydrodynamics. 84

5.2 Cases intended to study heat transfer from steam to falling liquid curtain. Liquid inlet temperature: 372.5 K, density: 994.0 kg/m^3, dynamic viscosity: 0.000 719 kg/m s, surf tension: 0.0589 N/s. The inlet thickness is 0.000 89 m. 85

5.3 Simulations to be run to investigate heat transfer into black liquor. . 90

LIST OF FIGURES

1.1 Liquor cycle in the kraft papermaking process. 4

1.2 Diagram of falling film. 6

1.3 Diagram of liquid curtain. 10

2.1 Fit to experimental data values for glass transition temperature from black liquor series. 18

2.2 Fit to experimental data values for zero shear rate viscosity from black liquor series. 18

2.3 Non-Newtonian viscosity of black liquor at high dry solids content for various temperatures. 19

2.4 Non-Newtonian viscosity of black liquor at high dry solids content for various dry solids content. 19

2.5 Simulation values of black liquor viscosity compared to experimental data. 20

2.6 Diagram of steam condensing on inner wall of evaporator. 21

3.1 Representation of a mesh cell with one neighboring cell visible [36]. . 23

3.2 Diagram of mesh expansion ratio [37]. 28

3.3 Thickness of falling film from simulation compared to experiments. . 29

3.4 Velocity of falling film from simulation compared to experiments. . . 29

3.5 Domain for Stefan's first problem. 30

3.6 Numerical and analytical values of the location of the liquid-vapor interface over time for the Stefan problem. 32

4.1 Diagram of falling film. 35

4.2 Mesh for falling film simulations. Domain inlet is shown. Gravity pulls to the right. 39

4.3 Mesh for falling film simulation. Image of shows region 0.8 m downstream. Gravity pulls to the right. 40

4.4 Heat transfer coefficient to falling liquid film. 41

4.5 Comparison of average Nusselt number for black liquor flow to physical experiment correlations and Nusselt flat film theory [39]. 42

4.6 The effect of Reynolds number and forcing frequency on the interface of heated falling liquid film. 43

4.7 Average liquid temperature along the streamwise location of the falling film for Reynolds numbers and forcing frequencies. 45

4.8 Average surface temperature along the streamwise location of the falling film for Reynolds numbers and forcing frequencies. 46

4.9 Evaporation rates at streamwise locations for excess wall temperature values. 47

4.10 Snapshot of simulation that shows the interface and the location on the interface where evaporation occurs. 48

4.11 Wall heat flux along the streamwise direction. 49

4.12 Calculated steam consumption in the streamwise direction. 50

4.13 Global steam consumption rates for evaporator lengths of increasing size for a Newtonian falling film. 51

4.14 Global liquid mass evaporation rates for evaporator lengths of increasing size for a Newtonian falling film. 52

4.15 Steam efficiency for evaporator lengths of increasing size for a Newtonian falling film. 52

4.16 Challenges with simulating black liquor flows while with fixed Reynolds number. Increasing Nusselt film values with dry solids content. Dashed line shows tube diameter for a typical falling film evaporator. 53

4.17 Snapshots of interface profiles for black liquor falling films with dry solids content: 50 %, 55 %, 60 %. For all flows the mass flow rate is 1 kg/s m. Lines detached from the interface are segments of fluid that have become detached from the bulk film. 55

4.18 Snapshots of interfacial temperature profiles for black liquor flow. . . 56

4.19 Crosswise temperature profile at various stations around a solitary wave far down the simulation domain. 58

4.20 Fast moving wave overtaking a slower moving wave. 59

4.21 Streamwise velocity profiles at various locations around a large solitary wave before and it crests and over takes the region in front. Film is moving the right. Gravity vector points to the right. Dotted teal line indicates location of the interface. Image on top occurs 0.01 seconds before image on bottom. 50 % dry solids content. 60

4.22 Temperature profiles around a large solitary wave before and after it crests and over takes the region in front. Dotted teal line indicates the film interface. The film is moving to the right and the gravity vector points to the right. 50 % dry solids content. See Figure 4.21 for velocity profiles at same locations. The black dashed line represents the division between fluid that was in the capillary wave and fluid that was in the front region. 61

4.23 Average temperature profile for black liquor falling film with varying dry solids content. 62

4.24 Surface temperature along the streamwise location for black liquor falling film with varying dry solids content. 63

4.25 Average evaporation rate for black liquor falling film for varying dry solids content. 64

4.26 Global steam consumption rates for evaporator lengths of increasing size for a black liquor falling film. 65

4.27 Global liquid mass evaporation rates for evaporator lengths of increasing size for a black liquor falling film. 66

4.28 Steam efficiency for evaporator lengths of increasing size for a black liquor falling film. 67

5.1 Diagram of liquid curtain. 71

5.2 Liquid curtain breakup length as a function of the mesh cells crosswise length. 74

5.3 Mesh for liquid curtain simulation. Domain entrance shown. Gravity acts to the right. 75

5.4 Mesh for liquid curtain simulation. Area shown is the breakup location of the curtain. Droplet is forming at the tip of the film and it will break away sometime later. 75

5.5 Liquid curtain with droplet forming at tip. Strand of liquid separated from curtain is capped on end with thick liquid regions. 76

5.6 Two-dimensional simulation of Newtonian fluid falling from a slot with negligible inlet velocity. Dashed line indicates time-average breakup location. 78

5.7 Analytical temperature model from Equations 5.30–5.34. 81

5.8 Images of simulated heated liquid curtain. Dashed line indicates time-average breakup location. 82

5.9 Simulation of heated liquid curtain. Dashed line indicates time-average breakup location. 83

5.10 Average breakup location of isothermal liquid curtain with respect to velocity ratio for various Weber numbers. 85

5.11 Mean streamwise velocity of liquid curtain. Simulation compared to free fall analytical solution of Brown. 86

5.12 Evaporation rates at streamwise locations for various velocity ratios. Dotted lines indicate the average breakup location. 87

5.13 Snapshot of simulation that shows the interface and the location on the interface where evaporation occurs. 87

5.14 Global steam consumption rates for evaporator lengths of increasing size for a Newtonian liquid curtain. 88

5.15 Global liquid mass evaporation rates for evaporator lengths of increasing size for a Newtonian liquid curtain. 88

5.16 Steam efficiency for evaporator lengths of increasing size for a Newtonian liquid curtain. 89

5.17 Variation of breakup location of black liquor liquid curtain with dry solids content. 91

5.18 Average evaporation rate of black liquor liquid curtain as it varies in the streamwise direction. 92

5.19 Global steam consumption rates for evaporator lengths of increasing size for a black liquor liquid curtain. 92

5.20 Global liquid mass evaporation rates for evaporator lengths of increasing size for a black liquor liquid curtain. 93

5.21 Steam efficiency for evaporator lengths of increasing size for a black liquor liquid curtain. 94

6.1 Evaporation rate along streamwise direction for falling film and liquid curtain simulations. 96

6.2 Comparison of Newtonian falling film and liquid curtain global steam consumption rates for evaporator lengths of increasing size. 97

6.3 Comparison of Newtonian falling film and liquid curtain global liquid mass evaporation rates for evaporator lengths of increasing size. . . . 98

6.4 Comparison of Newtonian falling film and liquid curtain steam efficiency for evaporator lengths. 98

6.5 Comparison of black liquor falling film and liquid curtain global steam consumption rates for evaporator lengths of increasing size. 100

6.6 Comparison of black liquor falling film and liquid curtain global liquid mass evaporation rates for evaporator lengths of increasing size. . . . 100

6.7 Comparison of black liquor falling film and liquid curtain steam efficiency for evaporator lengths. 101

LIST OF SYMBOLS OR ABBREVIATIONS

α	Liquid volume fraction used by volume-of-fluid method
a	Interpolation coefficient for discretizing transport equation, and Carreau-Yasuda viscosity model parameter
a_c	Evaporation heat transfer coefficient
A_i	Airy function
a_T	Shift factor for the Carreau-Yasuda model calculated from the William-Landel-Ferry relation
β	Angle between the falling film surface plane and horizontal
bl	Subscript denotes black liquor values
B_i	Bairy function, pair to the Airy function, A_i
b_P^{n-1}	Grouping of explicit terms that can be directly calculated from previous time step for cell P
Cr	Courant number
c_p	Specific heat
$C_{p,E}$	Excess heat capacity
$C_{p,s}$	Heat capacity of black liquor solids
$C_{p,w}$	Heat capacity of water
δT	Offset value relating glass transition temperature and absolute reference temperature
$\Delta T_{\mathbf{sat}}$	Difference between falling film wall temperature and saturation temperature of the liquid
δ	Half film thickness of falling liquid curtain
$\vec{d}$	Separation between the centroid of cell P and N
DS	Mass fraction of dissolved solids in black liquor
ϵ	Forcing frequency perturbation amplitude
$_x$	Fractional distance from the cell face, f, to the cell center of N
Fr	Froude number

$\vec{F}_{CSF}$	Continuum Surface Force, body force that accounts for the normal component of surface tension
f	Frequency of perturbation force
FF	Abbreviation for Falling Film
$\dot{\gamma}$	Shear rate
$\vec{g}$	Gravity vector
g	Subscript denoting values of gas or steam
h	Crosswise length of liquid sheet
h_N	Crosswise length of liquid sheet from Nusselt flat film theory
h_e	Enthalpy of vaporization
I	Subscript denotes interface values
inlet	Subscript for parameters at the inlet face of the domain
j_e^h	Evaporation heat flux density
Ka	Kapitza number
κ	Surface curvature
k	Thermal conductivity
λ	Carreau-Yasuda viscosity model parameter
l	Subscript denoted liquid film values
L_{br}	Streamwise breakup location of falling liquid curtain
LC	Abbreviation for Liquid Curtain
$\dot{m}_{\mathbf{2D}}$	Mass flow rate of film normalized by the spanwise length of the domain
$\dot{m}_{\mathbf{stm,cons}}$	Steam consumption, the mass rate of steam condensed into a liquid
μ	Dynamic viscosity
$\hat{n}$	Surface normal vector
ν	Kinematic viscosity
ν	Shear viscosity
Nu	Nusselt number

ν_0	Zero shear rate viscosity
n	Superscript indicating the time step, and Carreau-Yasuda viscosity model parameter
N	Neighboring cell to control volume P used for discretizing the transport equation, or as a subscript denotes Nusselt film values
Pe	Peclet number
ϕ	Generic scalar variable associated with the each cell
ϕ_e	Evaporation coefficient
p	Pressure
P	Control volume cell used for discretizing the transport equation
PISO	Pressure Implicit with Splitting of Operators
$\dot{q}''$	Wall heat flux
Re	Reynolds number
Re_C	Critical Reynolds number
ρ	Fluid density
ρ_w	Density of liquid water
ρ_{25}	Black liquor density at 25 °C
$R_{\textsf{gas}}$	Gas constant of water
$\dot{S}_m$	Source term for species enrichment
$\dot{S}_q$	Source term for heat transfer
$\dot{S}_v$	Source term for the volumetric transfer of liquid to vapor phase
$\dot{S}_v$	Source term for the volumetric transfer of liquid to vapor phase
σ	Surface tension coefficient
$\vec{\mathcal{S}}$	Surface area vector
sat	Subscript denotes saturation values
stm	Subscript denotes steam values
θ	Normalized temperature
$\vec{\tau}$	Strain rate tensor

T	Temperature
t	Time
T_0	Absolute reference temperature for black liquor viscosity model
$T_{\mathbf{avg}}$	Crosswise average temperature of liquid sheet
T_g	Glass transition temperature for black liquor viscosity model
u_N	Film streamwise velocity from Nusselt flat film theory
$u_{\mathbf{avg}}$	Crosswise average velocity of liquid sheet in the streamwise direction
$\vec{v}$	Velocity vector
$\mathcal{V}$	Volume
VOF	Volume of Fluid
We	Weber number
We_C	Critical Weber number
χ_S	Mass fraction of dissolved solids in black liquor
ξ	Mass diffusion coefficient for black liquor
$x_{\mathbf{st}}$	Location of in the streamwise direction at which measurements are recorded

SUMMARY

In this study, a numerical model is used to investigate the evaporation and flow characteristics of heated liquid sheets and films. The liquid is modeled as water and as a non-Newtonian fluid with the rheological properties of black liquor, a byproduct produced by paper mills. In the paper making process, black liquor is concentrated in an evaporator as a falling film, but the effectiveness of the evaporator is reduced due to fouling on heat transfer surfaces.

Two flow arrangements are to be investigated. First, a thin sheet of liquid sliding down a vertical heated plane with a free surface exposed to a gas, known as a falling film. This arrangement is the one currently used in paper mills. In this configuration, the black liquor and steam are separated by the heat transfer surface. Scale builds up on the black liquor side of the surface and causes an increase in the resistance to heat transfer over time. Periodically, the scale must be removed from the evaporator walls. The second arrangement, known as a liquid curtain, is a thin sheet of liquid falling under the influence of gravity heated from all free surfaces by an envelope of hot gas. In this arrangement, the liquid and gas come into direct contact, therefore there is no place for fouling to build up as there is no heat transfer surface. No fouling means a more consistent operation of the evaporator. This type of arrangement is not currently used in paper mills but is being investigated in this work to determine its feasibility.

The fluid system is modeled by solving the conservation equations of mass, momentum, and energy using the finite volume method with a single-fluid volume-of-fluid field to capture the multiphase transport and liquid-gas interface. The computational model is parallelized and run over multiple cores allowing for very refined spatial and temporal discretization.

The fluid system is simulated using the finite volume method with a single-fluid volume-of-fluid field to capture the multiphase transport and liquid-gas interface. The model is used to study the structure of surface waves in the presence of heat transfer and the effect of evaporation on the instability of liquid sheets for both water and black liquor. This study investigates how the breakup of a liquid curtain is affected by flow parameters and how the formation of droplets influences the evaporation characteristics of the liquid curtain. A power-law viscosity model is used to simulate the rheology of black liquor with greater than 50 % dry-solids.

Results from this study are used to compare the energy requirements and evaporation rate of the falling film on a heated surface and the falling liquid sheet heated from both sides by a layer of gas. From this comparison, the feasibility of evaporating black liquor as a falling liquid curtain is determined.

Evaporation from a falling film evaporator has an entrance length through which no evaporation takes place, after which the evaporation rate can grow very rapidly. On the other-hand, liquid curtains have a small evaporation rate starting right at the inlet that grows slowly along the streamwise direction. Downstream from the liquid curtains breakup, the evaporation rate peaks, and then drops down to pre-breakup value and continues to grow along the streamwise direction.

It is found that the falling film evaporator has a much higher liquid evaporation rate than evaporating as a liquid curtain. However, the falling film evaporator has an entrance length with no evaporation, and liquid curtains allow for evaporation to start occurring right at the inlet. If reducing length of the evaporator is a priority, liquid curtain evaporators can obtain a higher evaporation rate than falling films within the same distance.

Falling film evaporation has a higher steam efficiency than a liquid curtain evaporator. This is true of both Newtonian fluids and black liquor. However, for short evaporator lengths the rate at which water is removed from a liquid curtain evaporator is much greater, but at the cost of a higher steam consumption rate.

CHAPTER 1

INTRODUCTION

The primary goal of this project is study the hydrodynamics and transport mechanics of heated thin liquid sheets. It is motivated by the desire to identify a method of concentrating black liquor while minimizing the negative effects of scale formation.

To conduct this study, the project will focus on the hydrodynamics and transport mechanics of a Newtonian fluid with the properties of water and a non-Newtonian fluid approximating black liquor. Two principal flow geometries will be considered: a thin sheet of liquid flowing down a vertical heated surface with a free surface exposed to a gas, known as a falling film; and a thin sheet of liquid falling under the affect of gravity, heated from two free surfaces by an envelope of hot gas, known as a liquid curtain.

The current method used in the paper industry to evaporate black liquor is to have the liquor flow down a heated surface as a falling film. This method of heat transfer is effective, but it is also suffers from soluble scale fouling due to the crystallization of dissolved salts in the black liquor. When a salt that has formed in the black liquor comes into contact with the heated surface it will attach to the wall. Attached salts affect the flow of black liquor and increase the resistance to heat transfer. Salts that do not come in contact with the surface travel with the black liquor as it flows out of the evaporator and into the recovery boiler where the salts are incinerated. It is preferable to send the crystallized salts to the recovery boiler instead of the salts accumulating on the wall of the evaporator.

If it were possible to remove the heat transfer surface, there would be no location for the scale to form. Problems associated with scale include the need to periodically clean the wall of the evaporator, and an increase in heat transfer resistance over time as scale accumulates. Eliminating the opportunity for scale to occur prevents these problems and allows for a more consistent operation of the evaporator. This study will investigate heat transfer, evaporation, and wave structure of black liquor and water as a heated falling film and heated liquid curtain.

The first studies of liquid sheets were conducted by Taylor, who noticed that under certain conditions a sheet would experience instabilities and disintegrate [1, 2, 3]. Early work by Squire found that the growth rate of sheet instabilities is directly related to the density of the surrounding air [4]. The instability of a liquid sheet falling between two guide wires, a liquid curtain, has been explored by more recent authors such as Lin et al. who found that for a viscous liquid surrounded by a viscous gas, the sheet is absolutely unstable when the Weber number is below a critical value that depends on the Reynolds number [5, 6, 7, 8]. And the sheet is convectively unstable when the Weber number is greater than this critical value. The amplification of the convective instabilities can be suppressed by an increase in surface tension, an increase in viscosity of liquid or gas, or by a decrease of the density of the gas.

The breakup of a sheet as it separates into strands and droplets has a strong effect on the transport of heat. The breakup of black liquor sheets into strands and droplets has been studied by Spielbauer and Aidun [9, 10]. These studies found that there were two mechanisms that lead to the destruction of liquid sheets: the wave mechanism and the perforation mechanism. The wave mechanism causes drops to form with a discrete number of diameters, whereas the perforation mechanism predicts drops to form over a range of sizes. They concluded that since black liquor sprays form droplets of a wide variety of diameters, the perforation mechanism is the likely cause of black liquor sheet destruction. Although several researchers have focused on the hydrodynamics of liquid curtains, very little work has been done dealing with heat transfer to liquid curtains. One study of heated liquid curtains was conducted by

McCarthy and Merson who developed an equation for the temperature profile in a falling liquid curtain that is surrounded by steam [11]. However, the developed model was only valid while the sheet was intact.

This research specifically aims to:

- Investigate the effect of heat transfer and evaporation on instability and wave structure in Newtonian fluids for a falling film and a falling liquid curtain.
- Examine the effect of the non-Newtonian properties of black liquor on the instability and wave structure for a heated falling film and heated falling liquid curtain.
- Investigate the effect of heat transfer and evaporation of the breakup of falling liquid curtain.
- Determine if the concentrating of black liquor as a liquid curtain is comparable to the condensing of black liquor as a falling film.

These goals will be accomplished by solving the conservation laws using numerical simulations over a fine mesh.

1.1 Motivation

Black liquor is a viscous, shear thinning fluid that is a byproduct of the kraft paper-making process. It contains primarily energy dense lignin, 33 %, 31 % carboxylic acid, 28 % inorganics, and 8 % other components. Paper mills burn black liquor in order to utilize its energy. This recovery process allows kraft paper mills to be nearly energy neutral. Liquor in the kraft process moves through a cycle, shown in Figure 1.1. Wood to be pulped and white liquor go into the digester where they are cooked. Pulp and weak black liquor exit the digester. The pulp is moved on to the paper mill to form paper, and the weak black liquor moves through a series of concentrators to remove excess water. The strong black liquor from the concentrators is then combusted in the recovery boiler. And smelt from the recovery boiler is dissolved in water to

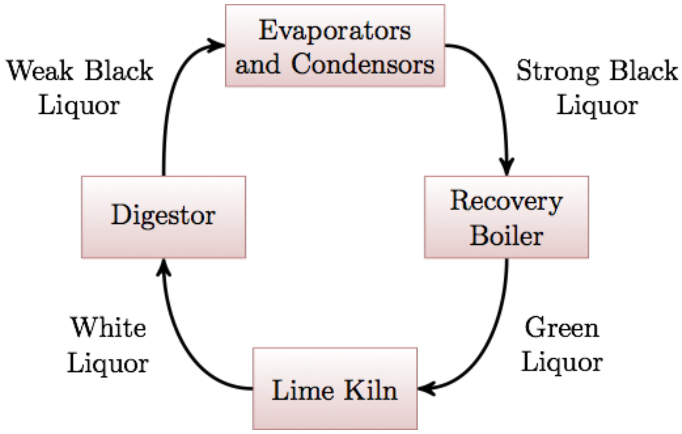

Figure 1.1: Liquor cycle in the kraft papermaking process.

create green liquor. White liquor is created from chemical reactions in the lime kiln to complete the cycle. This work focuses on the concentration of weak black liquor to strong black liquor. The combustion of black liquor in the recovery boiler has its challenges. When black liquor leaves the pulper, it has a concentration of about 15 % total solids. At 15 % total solids, the black liquor is mostly water. In order to be burned in the recovery boiler it needs a concentration of around 75 % total solids. Initially during evaporation, fouling does not occur and the black liquor behaves as a Newtonian fluid. When the black liquor is composed of roughly 50 % total solids, scale starts forming and the non-Newtonian properties of the black liquor becomes more prominent.

The current method of concentrating black liquor involves heating it in a falling film or raising film evaporator. These flow arrangements are subject to fouling on the heat transfer surfaces, reducing the heat transfer effectiveness over time and require increased pumping pressure to move the viscous black liquor. Periodically the scale needs to be cleaned off of the evaporator wall which requires evaporator down time and costly chemicals. Methods of scale removal include: boiling out, hydroblasting, acid or chemical cleaning. The consequences of scale lead to excess costs and higher energy requirements. If black liquor could be evaporated without the use of a heat transfer surface this would completely remove scaling and its negative effects. The objective of this study is to determine if a method of evaporating black liquor by heating it as a falling liquid curtain could be a viable replacement for condensing black liquor as a falling film.

A flow configuration that would allow heat transfer to the black liquor without using a heat transfer surface could be achieved by arranging the black liquor as a falling liquor curtain surrounded by hot steam. Falling liquid curtains are used in industry, typically for coating processes. For liquid sheets consisting of black liquor, the flow and breakup process would be complicated by the formation of salt crystals contributing to perforations in the sheet. Falling liquid sheets are inherently unstable because at a certain length the sheet will develop instabilities and disintegrate. However the surface waves formed at the interface increase transport and are highly desirable. Improving our knowledge of the mode and location of sheet breakup and the effect of surface waves on transport will allow us to have better control over the design of liquid sheet flows. The complex hydrodynamics and lack of previous work on falling liquid curtain transport makes this a suitable topic to study.

1.2 Falling Film

Falling films are thin liquid sheets falling under the influence of gravity with a free surface in contact with gas. A depiction of a falling film is shown in Figure 1.2. The flow becomes unstable when the Reynolds number exceeds a critical value, defined as $Re_C = (5/4)\cot(\beta)$. The angle β measures the angle between the free surface plane and horizontal. The Reynolds number for a falling film is defined as,

$$Re = \frac{\rho_l u_N h_N}{\mu_l} \, . \tag{1.1}$$

Where ρ_l is the liquid density, μ_l is the dynamics viscosity, and u_N, h_N are the average velocity and film thickness according to Nusselt theory respectively [12, 13]. For the case of a vertical falling film, which will be examined in this study, $Re_C = 0$, meaning these flows are exclusively unstable.

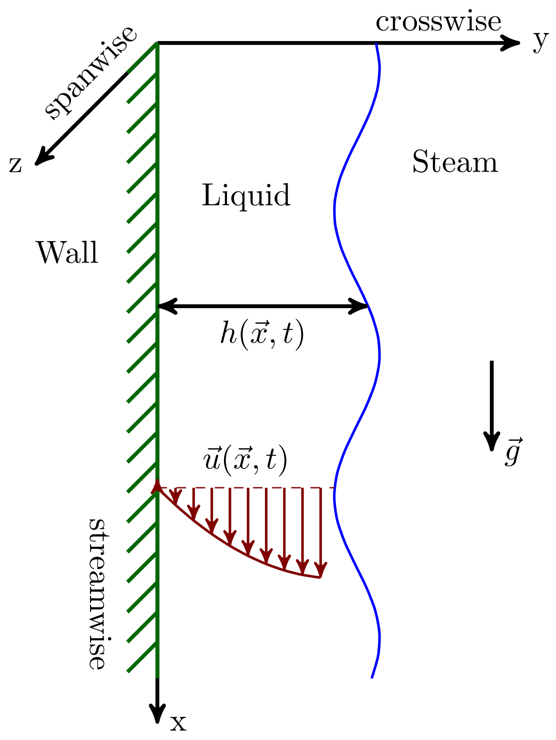

Figure 1.2: Diagram of falling film.

Near the inlet, instabilities cause short periodic waves. Linear stability theory suggest these disturbances should grow exponentially, but as the wave amplitude increases downstream non-linear effects hinder their growth. Instead, the amplitude of these large waves approach a finite value depending on the Reynolds number, and Kapitza number,

$$Ka = \frac{\sigma}{\rho_l \nu_l^{4/3} g^{1/3}} \,. \tag{1.2}$$

The instabilities result in large solitary waves with steep fronts following a series of small capillary waves [14].

Detailed investigations of falling films have focused on laminar flow which allows for a precise analysis of the hydrodynamics. Work by Kungui et al. studied separation vortices in the connecting region between solitary and capillary waves, and showed these separation vortices increase wall shear stress and enhance crosswise film transport [15].

1.3 Liquid Curtain

1.3.1 Hydrodynamics

A liquid curtain is a thin liquid sheet formed by expelling the fluid through a slot and allowing it to fall under the force of gravity. A diagram of a liquid curtain is shown in Figure 1.3. The first studies of liquid curtains were conducted by Brown who was motivated by studying curtain coating industrial processes [16]. Brown produced a relationship for the average film velocity of a liquid curtain based on the velocity of a particle falling freely under the force of gravity. This relationship was later refined by Aidun to increase accuracy near the curtain entrance [17]. Liquid curtains are also used in atomization by bombarding the sheet from both sides with high speed impinging air, so called airblast atomization.

Several methods of forming a liquid sheet have been investigated in the literature. A liquid jet impinging on a plate was the method used by Taylor in his popular study of water bells, which has then been investigate by other authors [1, 18]. Another type of liquid sheet is the radially expanding sheet created by two impinging jets [19, 20, 21]. Researchers also started investigating the characteristics of liquid sheets with different aspect ratios. Sheets with small length-to-thickness aspect ratios are created by driving liquid from a flat-spray nozzle. This type of flow is called a liquid fan and is characterized by thick rims at its edges [22]. Large aspect ratio flows, liquid curtains, are created by extruding liquid through a long, thin slot [5, 23, 24, 25].

1.3.2 Stability

Early linear stability analysis of falling liquid sheets neglected the viscosity of the liquid and the surround gas. These assumptions lead to the conclusion that the liquid sheet is inherently stable if $We < 1$ [5]. However this conclusion is in opposition to early experimental observations by Brown that showed that when $We < 1$ break down of the sheet could occur due to disturbances that propagate upstream. To account for this discrepancy later linear stability analysis took into account the viscosity of the liquid [6] and then the viscosity of the liquid and the gas [8].

Studies of the stability of a liquid curtain have determined that the two principle modes of disturbances are sinuous and varicose waves [5, 6]. Accounting for the viscosity of the liquid, Lin and Roberts found that there was no condition for with the sheet was absolutely unstable. However if $We < 1/2$ and $\rho_g/\rho_l \neq 0$, then the sinuous mode will be convectively unstable. If $\rho_g/\rho_l = 0$ the varicose mode is asymptotically stable, but if $\rho_g/\rho_l \neq 0$ then the varicose mode is unstable. Teng et al. conducted a more sophisticated analysis by accounting for the viscosity of both the liquid and the surrounding gas [8]. This analysis concluded that the sheet is absolutely unstable when $We < We_C$, where We_C, the critical Weber number depends weakly on the Reynolds number, Re, and We_C has a minimum value of one when Re is zero. The Weber number for this flow is defined as

$$We = \frac{\rho_l u_{l,\mathrm{inlet}}^2 h_{l,\mathrm{inlet}}}{\sigma} \tag{1.3}$$

and the Reynolds number is defined as

$$Re = \frac{\rho_l \, u_{l,\mathrm{inlet}} \, h_{l,\mathrm{inlet}}}{\mu_l} \, . \tag{1.4}$$

When $We > We_C$ the amplification of the sinuous mode is greater than the varicose mode, leading the sinuous mode to be convectively unstable.

1.3.3 Breakup

The mechanism by which liquid sheets disintegrate has been studied by Dombrowksi et al., who treated water as a viscous liquid sheet and the air as a stationary inviscid gas [26, 27]. From this work, three modes of sheet disintegration were identified: rim, wave, and perforated-sheet.

Rim disintegration occurs when the liquid has high viscosity and high surface tension. This is usually the method of breakup when the relative velocities are low.

The rim disintegration is caused by surface tension which causes the free edge of the liquid sheet to contract into a thick rim, which then breaks up similar to a free jet. Then newly formed droplets continue to travel in the flow direction and carry with them thin threads that quickly break up into a row of droplets. This creates large droplets surrounded by smaller satellite droplets. Wave disintegration is caused by the interaction between the liquid sheet and the surrounding air. This occurs when spanwise ligaments, that correspond to half or full wavelength segments, are torn away from the liquid sheet.

Perforated-sheet disintegration is caused by holes that are formed in the sheet. The holes have a thick rim at their edge and grow in size until they reach another hole or the sheet edge. Numerous holes in the sheet result in a network of ligaments of varying sizes. These ligaments then breakup into droplets of varying sizes. Perforations are formed by particles from within the fluid that come in contact with the surface, or by droplets from elsewhere that splash onto the sheet [9]. Since black liquor contains suspended solid particles, it is expected that the formation of holes play the primary role in the breakup of black liquor sheets.

1.3.4 Heat Transfer

Heat transfer to a falling liquid curtain has been studied previously by McCarthy and Merson, who investigated heat transfer from steam surrounding a falling liquid curtain of water [11]. They developed an analytical model for the temperature profile and provided experimental results. The calculated average crosswise temperature matched with with mixed cup temperature values measured along the streamwise direction. However, this model was created for an intact liquid sheets and is not valid for liquid curtains past the initial break up. Beyond these authors, there have been no other investigations of heated falling liquid curtains.

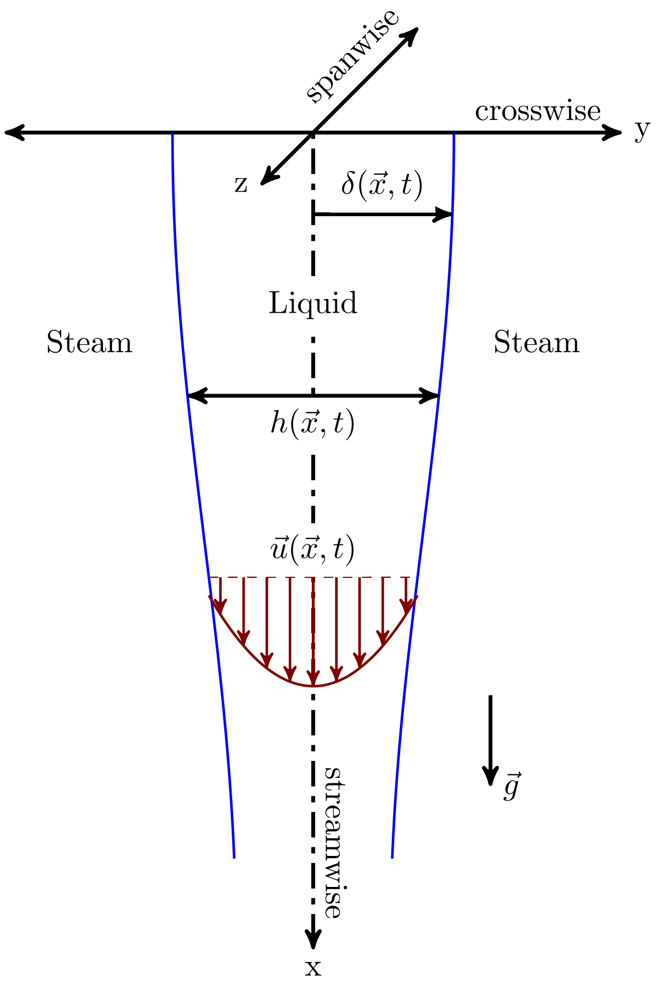

Figure 1.3: Diagram of liquid curtain.

1.4 Outline

The structure of this thesis is as follows:

- Chapter 1 provides an introduction to this research. A review of the current work for falling films and liquid curtains is included.
- Chapter 2 describes the mathematical method of describing thin film flows. Relationships for calculating the fluid properties, specifically the properties of black liquor at high dry solids content, are also presented.
- Chapter 3 describes the implementation of the computational solver. Discretization of the computation domain using the Finite Volume method is presented along with linearization of terms from the generic scalar transport equation. The Pressure Implicit with Splitting of Operators (PISO) algorithm used to solve pressure-velocity coupling of the governing equations is outlined.
- Chapter 4 describes the simulations conducted for falling film flows of water and black liquor and analyzes the results of these simulations.
- Chapter 5 discusses the simulations and results for liquid curtain flows of water and black liquor.
- In Chapter 6, the heat transfer and evaporation from the two fundamentally different flow arrangements falling films and liquid curtains are compared.
- Finally, Chapter 7 concludes with the observations from this work and offers recommendations for future investigators interested in pursuing similar research.

CHAPTER 2

RESEARCH METHODOLOGY

A schematic for a falling film is shown in Figure 1.2. The fluid inlet is at the top of the domain, and it flows down the wall in the streamwise direction. The bottom of the film is in contact with a stationary wall. The film has a thickness in the crosswise direction, h, and velocity field $\vec{v}$ that can vary over time and location. Gravity acts parallel to the stationary wall.

A schematic for a liquid curtain is shown in Figure 1.3. The fluid enters at the top of the domain and falls under the effect of gravity. The thickness of the film in the crosswise direction is denoted as h, and the half film thickness is denoted as δ. The velocity at the inlet is a constant value and as the film moves downstream it transitions to a parabolic-like velocity profile. Gravity acts perpendicular to the fluid inlet.

2.1 Numerical Setup

The focus of this study is to investigate the mechanics and transfer of thin liquid sheets. The concurrent flow of the two incompressible, immiscible fluids is simulated by modeling the domain as a single-fluid and solving the Navier-Stokes equations. To create the single-fluid model, the volume-of-fluid method (VOF) will be employed. The VOF method is in the family of one-fluid approaches to multi-species flow. This approach uses one set of conservation equations for the entire flow domain and a parameter is used to determine whether a cell contains fluid 1, fluid 2, or the interface of the two fluids.

2.1.1 Governing equations

A simple function is created to determine the location of each fluid. This function is defined to have a value of 1 if the liquid fills the cell and a value of 0 if steam fills the cell [28]. At the boundary of the two fluids, the function transitions smoothly from 0 to 1, where a cell containing a mixture of the two fluids is represented as a fractional value.

$$\alpha = \begin{cases} 1 & \text{location in liquid} \\ 0 < \alpha < 1 & \text{location of liquid-gas interface} \\ 0 & \text{location in gas} \end{cases} \tag{2.1}$$

Following the one-fluid approach, the VOF parameter, α, is used to determine the fluid properties throughout the flow domain,

$$\phi = \alpha\phi_1 + (1-\alpha)\phi_2 \,. \tag{2.2}$$

Where ϕ is any scalar property of the fluid such as density ρ, thermal conductivity k, or specific heat c_p. The fluid phase is propagated throughout the flow with the transport equation:

$$\frac{\partial \alpha}{\partial t} + \nabla \cdot (\vec{v}\alpha) + \nabla \cdot (\vec{v}_r \alpha(1-\alpha)) = -\dot{S}_v \,. \tag{2.3}$$

The source term $\dot{S}_v$ accounts for the the change in liquid volume due to the vaporization of the liquid phase [29]. The parameter $\vec{v}_r$ is an artificial velocity applied to this transport equation to keep the interface sharp and is separate from the velocity found by solving the Navier-Stokes equations. The value for is constructed so that it always acts perpendicular to the interface and is slightly larger than the maximum velocity in the transition region [30]. Applying a convective velocity to the interface that is slightly greater than the velocity of the region in front of the interface has the effect of compressing the interface. This additional velocity is rationalized by noting that it only acts over the small area of the interface.

Using the VOF method allows the entire flow domain to be represented as a single fluid. The velocity and pressure for the single-fluid system are solved from the mass and momentum conservation equations, respectively:

$$\frac{\partial \rho}{\partial t} + \nabla \cdot \rho \vec{v} = 0 \tag{2.4}$$

$$\frac{\partial \rho \vec{v}}{\partial t} + \nabla \cdot \rho \vec{v} \vec{v} = -\nabla p + \nabla \cdot \vec{\tau} + \rho \vec{g} + \vec{F} \,. \tag{2.5}$$

Where $\vec{v}$ is the velocity vector, p is the pressure, T is temperature, $\vec{g}$ is the gravity vector, σ is the surface tension coefficient, and $\vec{\tau}$ is the strain rate tensor. The force term at the end of Equation 2.5, $\vec{F}$, is the body force that accounts for the effects of surface tension. Since the VOF method does not track the interface directly, surface forces must be converted to body forces that only act at the interface. The continuum surface force accounts for the normal component of surface tension [31],

$$F_{\text{CSF}} = \int_{\mathcal{S}_I} \sigma \kappa_I \hat{\mathbf{n}}_I \delta(\vec{x} - \vec{x}_I) dS \tag{2.6}$$

$$F_{\text{CSF}} \approx \sigma \kappa \nabla \alpha \,. \tag{2.7}$$

The curvature of the interface is represented by κ, $\hat{\mathbf{n}}$ is the normal vector on the interface, and $\mathcal{S}_I$ is the interfacial area. The subscript I denotes variable values at the interface. This force is limited to the interface between the two fluids due to the gradient of the indicator function, α. The curvature is calculated from the normal of the interface

$$\kappa = \nabla \cdot \hat{\mathbf{n}} \,. \tag{2.8}$$

And the normal is determined from the gradient of the the phase indicator:

$$\hat{\mathbf{n}} = \frac{\nabla \alpha}{|\nabla \alpha|} \,. \tag{2.9}$$

In the one-fluid system, the heat transfer is governed by the following equation:

$$\frac{\partial \rho c_p T}{\partial t} + \nabla \cdot (\rho \vec{v} c_p T) = \nabla \cdot k \nabla T - \dot{S}_q \,. \tag{2.10}$$

Where $\dot{S}_q$ is the source term that accounts for the energy of evaporation. To account for the dry solids mass fraction as the mass of the liquid region changes during evaporation, a transport equation for species is employed:

$$\frac{\partial \chi_S}{\partial t} + \nabla \cdot \rho \vec{v} \chi_S = \nabla \cdot \rho \xi \nabla \chi_S + \dot{S}_m \,, \tag{2.11}$$

where χ_S is the mass fraction of dissolved solids, and ξ is the mass diffusion coefficient for black liquor. The source term $\dot{S}_m$ accounts for the change in liquid mass due to the vaporization of the liquid phase. The species conservation equation is only used for simulations of black liquor which requires the changes in dry solids content to be accounted for, and not for simulations of water.

2.1.2 Surface Evaporation

The numerical simulation employs an evaporation model for front-capturing methods developed by Hardt [29]. If the interfacial temperature differs from the saturation temperature, evaporation heat flux density, j_e^h, is considered to be

$$j_e^h = a_c \left(T_i - T_{\text{sat}} \right) \ , \tag{2.12}$$

where T_i is the interfacial temperature, T_{sat} is the saturation temperature, and a_c is the evaporation heat transfer coefficient determined from kinetic theory [32] to be

$$a_c = \frac{2\phi_e}{2 - \phi_e} \frac{h_e^2}{\sqrt{2\pi R_{\text{gas}}}} \frac{\rho_v}{T_{sat}^{3/2}} \,. \tag{2.13}$$

In Equation 2.13, ϕ_e is the evaporation coefficient, h_e is the enthalpy of vaporization, and R_{gas} is the gas constant of water. The evaporation flux occurs at the interface which, as defined by the parameter α, is located where the gradient of α is non-zero. The evaporative source term is calculated from

$$\dot{S}_q = \frac{j_e^h}{V} \int_V |\nabla \alpha| dV \,. \tag{2.14}$$

Using these relations, the other source terms can be computed as follows:

$$\dot{S}_m = \frac{\dot{S}_q}{\rho_l h_e} \tag{2.15}$$

$$\dot{S}_v = \frac{\dot{S}_q}{\rho_w h_e}\,. \tag{2.16}$$

Where ρ_w is the density of only the water portion of the liquid. For simulations only containing water the distinction between the liquid and water is irrelevant, but for simulations with black liquor the density of water at the local thermodynamic state may differ greatly from the density of the black liquor.

2.1.3 Black Liquor Properties

Black liquor is a complex substance. Fluid properties are calculated from experimental data from a compendium of industry technical papers [33]. For example, the density of black liquor is calculated as

$$\begin{gathered} \frac{\rho_{\mathrm{bl}}}{\rho_{25}} = 1 - 3.69 \times 10^{-4}(T - 298.15) - 1.94 \times 10^{-6}(T - 298.15)^2 \\ \rho_{25} = 997 + 649\chi_S\,. \end{gathered} \tag{2.17}$$

Where ρ_{bl} [kg/m^3] is the black liquor density, T [K] is the temperature, and ρ_{25} [kg/m3] is the black liquor density at 25 °C. The specific heat capacity of black liquor, $C_{p,\mathrm{bl}}$ [J/kg K], is calculated from Equation Set 2.18 by relating the value to the heat capacity of water, $C_{p,\mathrm{w}} = 4216\,\mathrm{J/kg\,K}$.

$$\begin{aligned} C_{p,\mathrm{bl}} &= (1 - \chi_S)\, C_{p,\mathrm{w}} + (\chi_S)\, C_{p,\mathrm{s}} + C_{p,\mathrm{E}} \\ C_{p,\mathrm{s}} &= 1684 + 4.47\,(T - 273.15) \\ C_{p,\mathrm{E}} &= (4930 - 29\,(T - 273.15))\,(1 - \chi_S)\,(\chi_S)^{3/2} \end{aligned} \tag{2.18}$$

The intermittent terms $C_{p,\mathrm{s}}$ [J/kg K] and $C_{p,\mathrm{E}}$ [J/kg K] represent the heat capacity of the black liquor solids and the excess heat capacity respectively. The relationship for thermal conductivity, k [W/m K], is

$$k = 1.44 \times 10^3(T - 273.15) - 0.335\chi_S + 0.58\,. \tag{2.19}$$

The viscosity of black liquor is calculated from a modified version of the Carreau-Yasuda relationship for non-Newtonian viscosity,

$$\frac{\nu}{\nu_0} = \left[1 + (\lambda a_T \dot{\gamma})^a\right]^{\frac{n-1}{a}} . \tag{2.20}$$

Where ν [Pa s] is the shear viscosity, and $\dot{\gamma}$ [1/s] is the shear rate. The other values, λ, n, and a are experimentally determined values for the specific black liquor. And a_T is an adjustment value calculated from the William-Landel-Ferry relation,

$$a_T = \exp\left(\frac{C_1 \left(T - T_0\right)}{C_2 + T - T_0}\right) . \tag{2.21}$$

Where $C_1 = -26.77$ and $C_2 = 104.14\,\mathrm{K}$ were determined as a good fit for all black liquors studied by Zaman and Fricke [34]. These authors noted that the value for T_0 is related to the glass transition temperature, T_g. A numerical fit for T_g from the experimental data is shown in Figure 2.1 and the relationship is found to be:

$$T_g\left(X_s\right) \rightarrow\ T_g = 133.4\chi_S + 124.4 \tag{2.22}$$

$$T_0 = T_g + \delta T\,. \tag{2.23}$$

Where δT is a parameter specific to the black liquor. The last piece of information needed to calculate the viscosity from Equation 2.20 is the zero shear rate viscosity, ν_0. The experimental data is a function of both the dry-solids content and temperature. In order to create a function of a single dependent variable to generate a data fit, the dry-solids content and temperature were combined into one parameter, $(\chi_S/(\chi_S + 1))(1/T)$ [35]. The numerical fit for zero shear rate is shown in Figure 2.2, and the relationship is determined to be:

$$\nu_0\left(X_s, T\right) \rightarrow\ \log\left(\nu_0\right) = 29270\left(\frac{\chi_S}{\chi_S + 1}\right)\left(\frac{1}{T}\right) - 32.79\,. \tag{2.24}$$

The black liquor series used for these calculations is from the work of Zaman and Fricke and is labeled as ABAFX011,12. The parameter values for the black liquor series are shown in Table 2.1.

Table 2.1: Parameter values for black liquor series ABAFX011,12 [34].

Parameter	Value
λ	8.187
n	0.515
a	1.077
δT	74.2

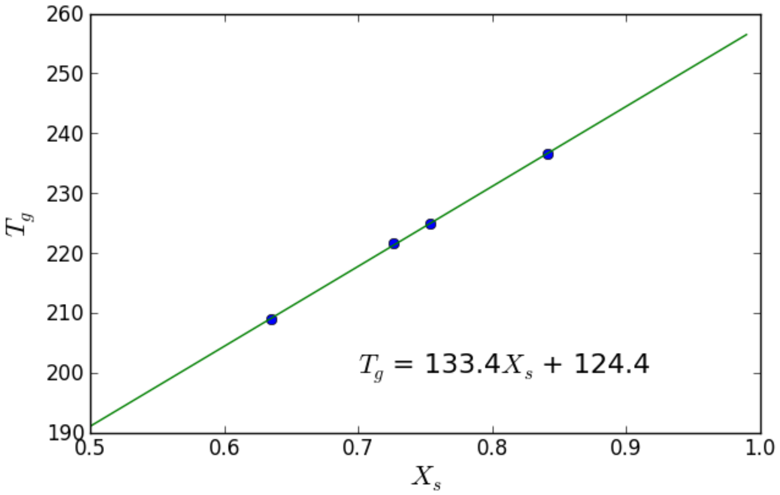

Figure 2.1: Fit to experimental data values for glass transition temperature from black liquor series.

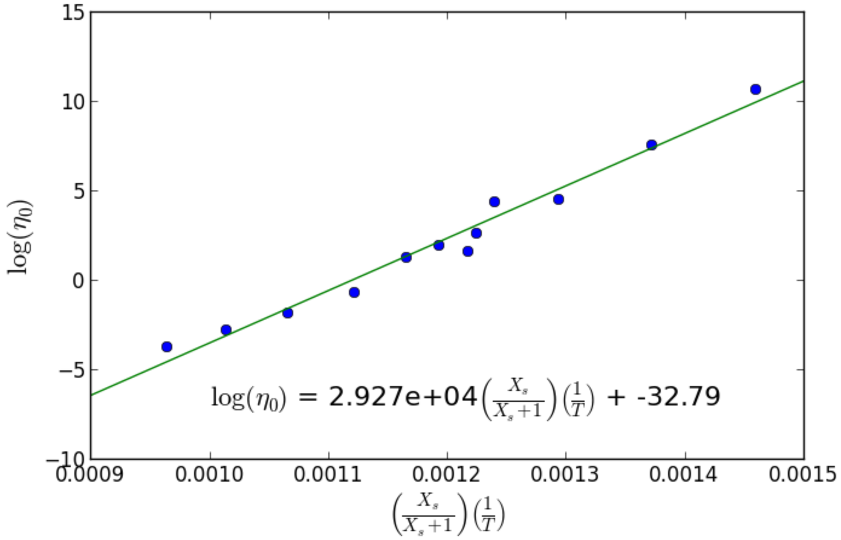

Figure 2.2: Fit to experimental data values for zero shear rate viscosity from black liquor series.

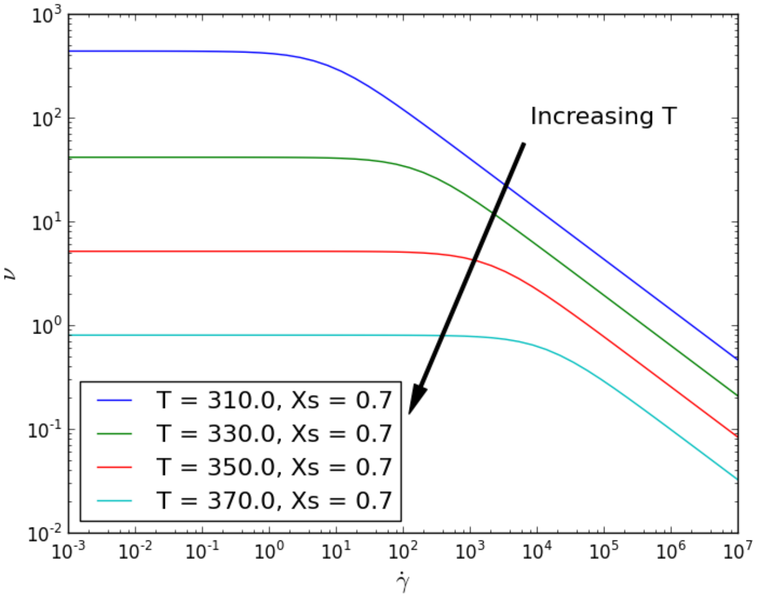

Figure 2.3: Non-Newtonian viscosity of black liquor at high dry solids content for various temperatures.

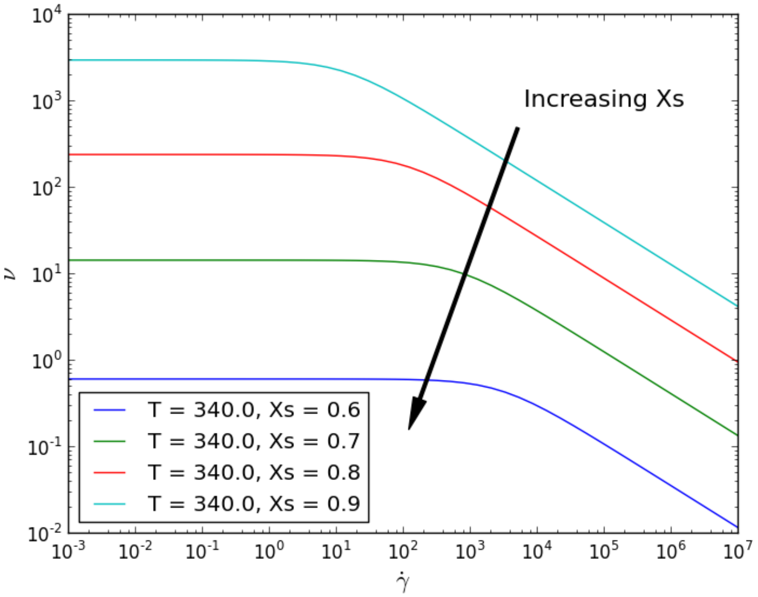

Figure 2.4: Non-Newtonian viscosity of black liquor at high dry solids content for various dry solids content.

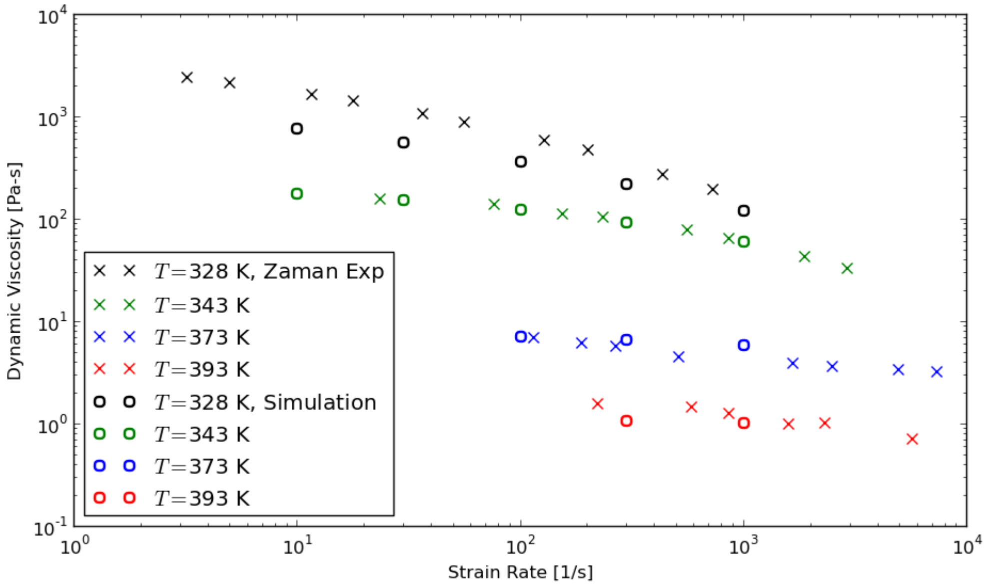

Figure 2.5: Simulation values of black liquor viscosity compared to experimental data.

2.1.4 Boundary Conditions

The inlet condition for the falling film specifies values for the phase indicator, temperature, and dry solids content of the incoming fluid: $\alpha = 1$, $T = T_{\text{inlet}}$, $\chi_S = \chi_{S,\text{inlet}}$. Regarding the velocity, Nusselt theory states that for a laminar falling film the average film x-velocity, called the Nusselt film velocity u_N, and average film height, the Nusselt film thickness h_N, will be

$$u_N = \left(\frac{Re^2 \mu_l g}{3\rho_l} \right)^{1/3} \tag{2.25}$$

$$h_N = \left(\frac{3Re\mu_l^2}{\rho_l^2 g} \right)^{1/3} . \tag{2.26}$$

In Equations 2.25 and 2.26, Re is the film Reynolds number, ρ_l and μ_l are the film density and viscosity respectively. To encourage the development of interfacial waves, the inlet velocity will be disturbed by a small perturbation, ϵ, with a driving frequency, f,

$$u_{\text{inlet}} = u_N \left(1 + \epsilon \sin\left(2\pi f t\right)\right) . \tag{2.27}$$

This disturbance is comparable to the pumping frequency used to drive black liquor through the evaporator. The fluid is in contact with a stationary wall, and at this

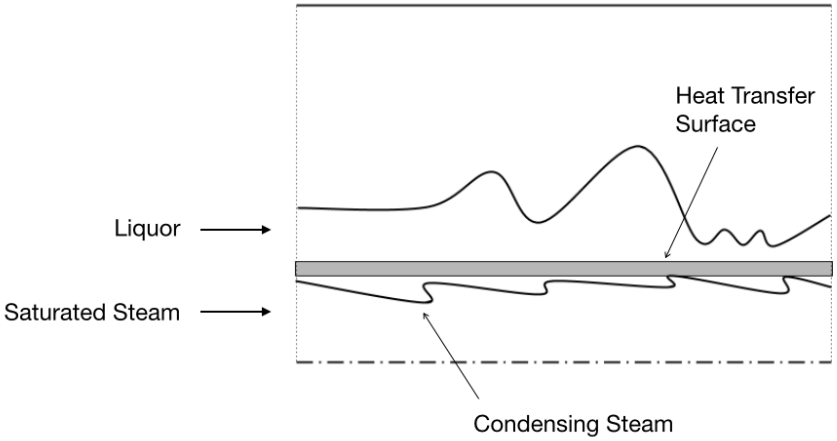

Figure 2.6: Diagram of steam condensing on inner wall of evaporator.

location the fluid velocity is zero, $u = 0$, $v = 0$. To simulate the heat transfer from the evaporator surface a constant wall temperature is specified, $T = T_{\text{wall}}$. The other required parameters are set so that there is no mass flux through the wall: $\partial\alpha/\partial x = 0$, $\partial\chi_S/\partial x = 0$. At the sides and outlet of the domain the fluid is able to freely leave the domain. The phase indicator, velocity, temperature, and species at the sides and out of the domain have a zero gradient; $\partial\alpha/\partial x = 0$, $\partial u/\partial x = 0$, $\partial v/\partial x = 0$, $\partial T/\partial x = 0$, and $\partial\chi_S/\partial x = 0$.

For the liquid curtain, the inlet conditions for the two fluids are specified. The phase indicator, $\alpha = 1$ or 0, temperature, $T = T_{\text{inlet}}$, and dry solids content of the incoming fluids $\chi_S = \chi_{S,\text{inlet}}$. The inlet velocity is set to be a fixed value, $u = u_{\text{inlet}}$. The outlet boundary conditions for the liquid curtain are the same as the outlet boundary conditions of the falling film: $\partial\alpha/\partial x = 0$, $\partial u/\partial x = 0$, $\partial v/\partial x = 0$, $\partial T/\partial x = 0$, and $\partial\chi_S/\partial x = 0$. In place of wall boundary conditions, the crosswise edges of the domain are periodic.

CHAPTER 3

NUMERICAL IMPLEMENTATION

The governing equations are evaluated using a solver constructed from the OpenFOAM CFD library which implements the finite volume method (FVM). The domain is discretized into a series of fully connected and non-overlapping cells. The boundary condition of the domain are applied using the boundary conditions specified in Section 2.1.4. And the fluid properties of the liquid and gas are determined using the methodology from Section 2.1.3.

3.1 Numerical Algorithm

The solution domain is discretized into a mesh of fully connected and non-overlapping cells. The PDE's are then discretized and applied across the computational mesh. Discretization with respect to time is accomplished by using a timestep, Δt, that is allowed to change during the simulation depending on the need to limit the Courant number. Figure 3.1 shows a diagram of a computational cell, P, and a single visible neighbor, N. A flat face, labeled f, separates the cell from its neighbor. The surface normal vector, $\vec{\mathcal{S}}_f$, represents the unit vector orthogonal to the face f, and $\mathbf{d}$ represents the separation between the centroid of cell P and N. Fluid properties and dependent variables are stored at the cell centroid except for flux values which are stored on cell faces.

3.1.1 Discretization of PDEs

After the solution domain has been discretized, the next step is to discretize the PDEs. As an example consider the conservation equation for a generic scalar, ϕ,

$$\frac{\partial \rho\phi}{\partial t} + \nabla \cdot (\rho\vec{v}\phi) = \nabla \cdot (\Gamma\nabla\phi) + S_\phi \,. \tag{3.1}$$

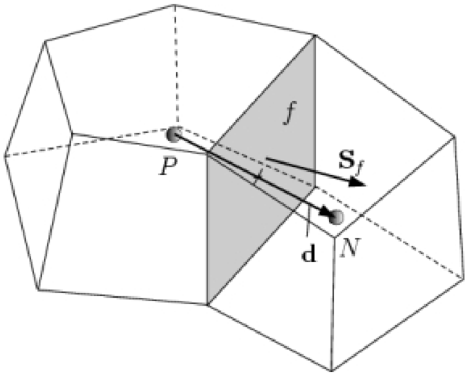

Figure 3.1: Representation of a mesh cell with one neighboring cell visible [36].

Where Γ is the diffusion coefficient and S_ϕ is the source term. In Equation (3.1) the first and second terms on the left side of the equation represent change in the cell with time and convection respectively. The third and four terms on the right side of the equation represent the diffusion of the scalar and a source terms. To condition the conservation equation to be solved by the finite volume method, the equation is first integrating over the control volume,

$$\int_t^{t+\Delta t}\left[\int_{\mathcal{V}_P}\rho\phi d\mathcal{V}+\int_{\mathcal{V}_P}\nabla\cdot(\rho\vec{v}\phi)d\mathcal{V}\right]dt=\int_t^{t+\Delta t}\left[\int_{\mathcal{V}_P}\nabla\cdot(\Gamma\nabla\phi)d\mathcal{V}+\int_{\mathcal{V}_P}S_\phi d\mathcal{V}\right]. \tag{3.2}$$

The terms of the result are then converted from volume integrals to surface integrals using Gauss's Theorem:

$$\int_{\mathcal{V}}\nabla\star\phi d\mathcal{V}=\int_{\mathcal{S}}d\vec{\mathcal{S}}\star\phi\,. \tag{3.3}$$

Where the operator $\star$ represents a general tensor operator.

Time Derivative

In the computational model used in this study the time derivative is discretized using the backward Euler scheme,

$$\frac{\partial}{\partial t}\int_{\mathcal{V}}\rho\phi d\mathcal{V}=\frac{(\rho_P\phi_P)^n-(\rho_P\phi_P)^o}{\Delta t}\mathcal{V}_P\,. \tag{3.4}$$

Where the value of the scalar at the previous timestep, t, is represented by ϕ^o. And the new value at time, $t+\Delta t$, is represented by ϕ^n. This discretization method allows for a stable solution method that is first order accurate in time.

Gradient Term

The discretization of gradient terms is as follows:

$$\int_{\mathcal{V}} \nabla \phi d\mathcal{V} = \int_{\mathcal{S}} d\vec{\mathcal{S}}\phi = \sum_f \vec{\mathcal{S}}_f \phi_f \, . \tag{3.5}$$

Where ϕ_f is evaluated at the face of the control volume. The value for ϕ_f is calculated from cell center of cells P and N using the Central Differencing scheme

$$\phi_f = f_x \phi_P + (1 + f_x)\phi_N \, . \tag{3.6}$$

The weight f_x is a fraction of distance from the cell face, f, to the cell center of N and the distance from cell centers of P and N. This value is calculated as

$$f_x = \frac{|\mathbf{d}_{fN}|}{|\mathbf{d}|} \, . \tag{3.7}$$

Convective Term

The convection term is integrated over the control volume and linearized as follows:

$$\int_{\mathcal{V}} \nabla \cdot (\rho \vec{v} \phi) d\mathcal{V} = \int_{\mathcal{S}} d\vec{\mathcal{S}} \cdot (\phi \vec{v} \phi) = \sum_f \vec{\mathcal{S}}_f \cdot (\rho \vec{v})_f \phi_f = \sum_f F \phi_f \, . \tag{3.8}$$

Divergence Term

The divergence term is also integrated over the control volume and linearized as

$$\int_{\mathcal{V}} \nabla \cdot \phi d\mathcal{V} = \int_{\mathcal{S}} d\vec{\mathcal{S}} \cdot \phi = \sum_f \vec{\mathcal{S}}_f \cdot \phi_f \, . \tag{3.9}$$

Source Term

The source term is expressed explicitly using its known value computed from the previous time step for the location at the center of the control volume:

$$\int_{\mathcal{V}} \phi d\mathcal{V} = \phi^o \mathcal{V}_P \, . \tag{3.10}$$

3.1.2 Boundary Conditions

Cells whose neighbors would be outside the solution domain have boundary conditions applied at the boundary faces of the cell in order to complete the linearization. For Dirichlet boundary conditions with a prescribed value, the fixed boundary value, ϕ_b, is applied at the boundary wall. In terms where the face gradient is needed for discretization, the value is calculated from the the cell center and the fixed boundary value,

$$\vec{\mathcal{S}}_f \cdot (\nabla\phi)_f = |\vec{\mathcal{S}}_f| \frac{\phi_b - \phi_P}{|\mathbf{d}|} \,. \tag{3.11}$$

For Neumann boundary conditions with a prescribed gradient, the gradient is calculated as

$$g_b = \left(\frac{\vec{\mathcal{S}}}{|\vec{\mathcal{S}}|} \cdot \nabla\phi \right)_f \,. \tag{3.12}$$

For terms where the boundary face value is needed for discretization, it is calculated from the gradient $\phi_b = \phi_P + |\mathbf{d}|g_b$ The gradient value can be used directly for terms that require the face gradient value for discretization,

$$\vec{\mathcal{S}}_f \cdot (\nabla\phi)_f = |\vec{\mathcal{S}}_f| g_b \,. \tag{3.13}$$

After the governing PDEs have been fully discretized the relation for a parameter ϕ at cell P can be determined from the neighboring cells as

$$a_P \phi_P^n + \sum_N a_N \phi_N^n = b_P^{n-1} \,. \tag{3.14}$$

Where the a's are interpolation coefficients, ϕ is the scalar variable associated for each cell, n indicates the current timestep, and b_P^{n-1} represents the collection of terms that can be directly calculated from the previous time step. Different interpolation schemes are determined for each flow variable, $\vec{v}$, p, α, or χ_S depending on numerical stability. Performing this summation for all cells in the domain leads to a set of equations which are formed into the matrix equation and solved using iterative methods,

$$[A][\phi] = [b] \,. \tag{3.15}$$

A form of Equation 3.15 is generated for each governing equation. For sets of equations that have coupled variables, the variable of concern for the particular equation is used as the variable to be solved for, ϕ, while the other variables are treated as constants. The secondary variables, acting as constants, use values from the previous time iteration. The iterative solver used for each matrix equation can be changed depending on the numerical stability of the solution.

3.1.3 PISO Algorithm

Collocated grids, where all the variables are stored in the cell center, can suffer from numerical problems such as "checker-boarding". To prevent these issues, the solver determines the flux at the cell wall when solving for pressure-velocity coupled equations. The solver executes the following sequence:

1. Use fluid and flow values from the previous or initial time step.
2. Solve energy equation and compute source terms.
3. Calculate conservation of species equation to determine mass transfer.
4. Determine the phase field by solving the phase indicator equation, and calculate the interface curvature.
5. Construct the momentum equation with the current pressure field to determine an intermediate velocity field.
6. Iterate through PISO Loop:
    (a) Predict flux values using current velocity field.
    (b) Assemble and solve the pressure equation.
    (c) Correct fluxes.
    (d) Recreate velocity field from fluxes.

3.2 Liquid Curtain Mesh

Although a stable implicit time discretization scheme is used, the Courant number still has an important role. For large Courant numbers the PISO algorithm takes a long time to converge, therefore reducing the Courant number is critical to reduce simulation times. In falling film simulations the maximum velocity in the domain tends to stay near to the Nusselt velocity. However the maximum velocity for liquid curtain simulation can become quite large since it is related to the free fall velocity. An expanding mesh is used for these simulations. A diagram of this type of mesh is shown in Figure 3.2.

Special consideration is made towards the mesh, because of the wide variation in velocity, to keep the Courant number small. The expansion ratio, $r = \delta_e/\delta_s$, is used to prescribe the mesh geometry. Before the simulation is conducted the value for the expansion ratio can be determine by minimizing the function for the Courant number along the streamwise direction. Given a starting cell length and a fixed number of cells, N, the length of any cell n in the streamwise direction can be calculated as

$$\delta_n = \delta_s + n\,(r-1)\,\frac{\delta_s}{N}\,. \tag{3.16}$$

The projected streamwise velocity at cell n can then be calculated using the dimensional form of Brown's free fall equation and the cell lengths.

$$u_n^2 = u_0^2 + 2g(\delta_s + n\delta_n) + 4(4g\mu/\rho)^{2/3} \tag{3.17}$$

The Courant number at cells in the streamwise direction is then calculated as

$$Cr_n = u_n \Delta t/\delta_n\,. \tag{3.18}$$

The expansion ratio can now be optimized for each simulation to achieve a minimum value for the projected maximum Courant number in the domain.

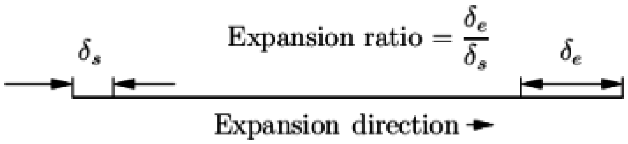

Figure 3.2: Diagram of mesh expansion ratio [37].

3.3 Validation Cases

In a previous work by Doro, the ability of the computational model to capture thin film hydrodynamics was validated and heat transfer [38, 39]. The following subsections discusses validation cases to show that the solver can capture the flow physics of heated thin sheets.

3.3.1 Film Hydrodynamics

To confirm the computational model can capture the hydrodynamics of thin films, simulations were conducted and compared the the experiments and simulations of Dietze et al. [40] The following simulation are for a falling film of DMSO-water solution with a Reynolds number of 15, and a forcing frequency of 16 Hz with measurements taken 0.12 mm downstream from the inlet. In this case the liquid has a density of $1098.3\,\mathrm{kg/m^{-3}}$ and a viscosity of $2.85 \times 10^{-6}\,\mathrm{m^2/s}$. And the surface tension is 0.0484 N/m. Figure 3.3 shows the results of film thickness for simulated and experimental values. As can be seen in the figure, the computational model matched the measured values for the film thickness.

Figure 3.4 shows the results of the near wall velocity of the falling film for simulations and experiments. The computational model matched the measured values for the near wall thickness very well. The simulations from this work seem to match the maximum magnitude of the near wall film better than the previous authors. However both sets of simulation suffer from a dip in velocity immediately after the maximum peak that is not present in the experimental measurements.

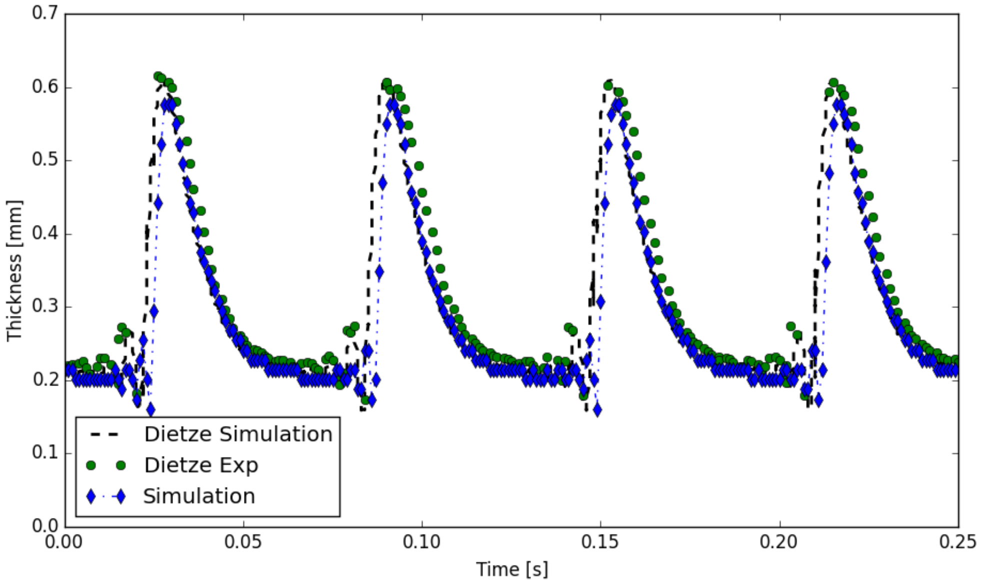

Figure 3.3: Thickness of falling film from simulation compared to experiments.

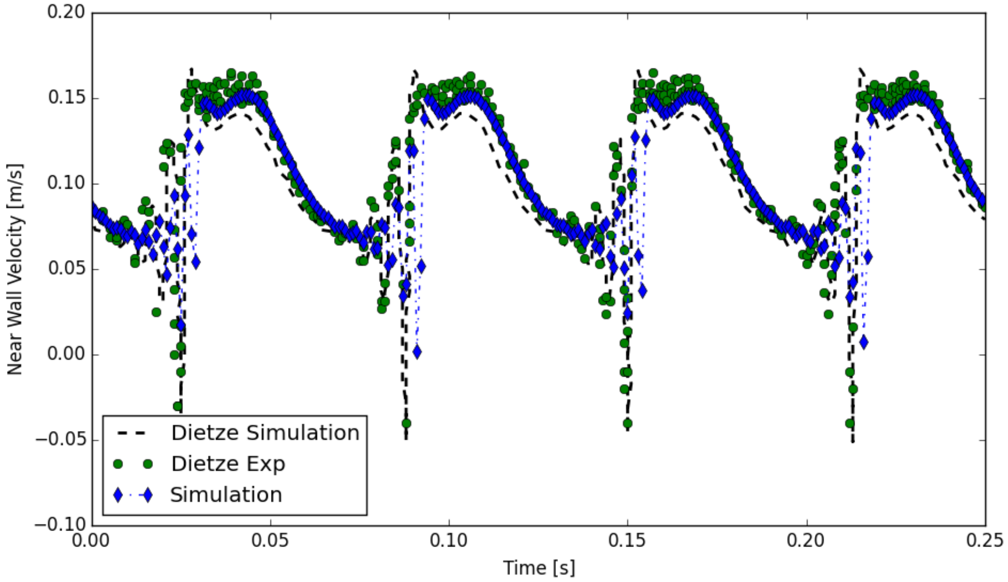

Figure 3.4: Velocity of falling film from simulation compared to experiments.

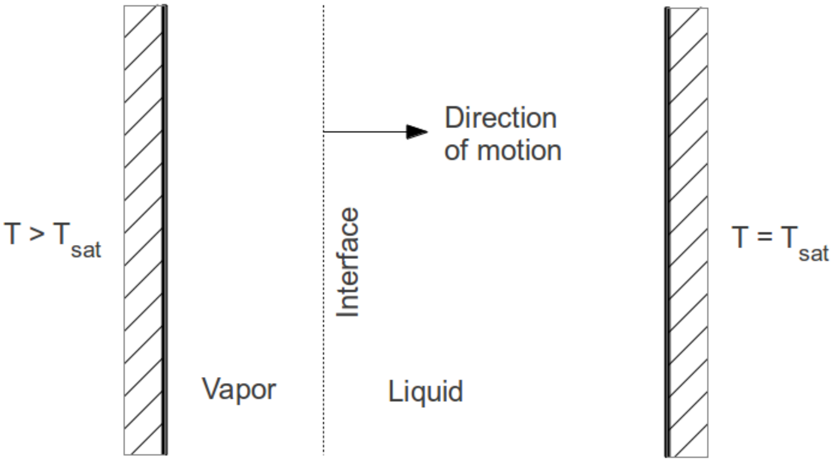

Figure 3.5: Domain for Stefan's first problem.

3.3.2 Surface Evaporation Model

In order to verify the surface evaporation model addressed in Section 2.1.2, the computational model is used to simulate the one dimensional Stefan problem. This was the same validation case use by Hardt, whose surface evaporation model is being used [29]. The aim of the Stefan problem is to track the movement of a liquid-vapor interface, x_{int}, where the movement of the interface is driven by the evaporation.

The boundary conditions for the Stefan problem are

$$T\left(x=0,t\right)=T_0 \tag{3.19}$$

$$T\left(x=x_{\text{int}}(t),t\right)=T_{\text{sat}}\,. \tag{3.20}$$

The temperature of the wall at $x = 0$ is T_0, which is a value greater than the saturation temperature, T_{sat}, of the liquid. The liquid in the domain is at the saturation temperature. The vapor that will form between the hot wall and the liquid interface is found to have a temperature that varies linearly along x between T_0 at the wall and T_{sat} at the interface. Figure 3.5 depicts a diagram of this domain.

The analytical solution for this problem was formulated by Neumann and is well

Table 3.1: Fluid properties used in Stephan problem simulation.

Parameter	Value
ν_l	$1.0 \times 10^{-5}\,\mathrm{m^2/s}$
ν_g	$1.0 \times 10^{-5}\,\mathrm{m^2/s}$
ρ_l	$1\,\mathrm{kg/m^3}$
ρ_g	$1\,\mathrm{kg/m^3}$
$c_{p,l}$	$1000\,\mathrm{J/kg\,K}$
$c_{p,g}$	$1000\,\mathrm{J/kg\,K}$
k_l	$1\,\mathrm{W/m\,K}$
σ	$0.01\,\mathrm{N/m}$
h_e	$1.0 \times 10^{6}\,\mathrm{J/kg}$
ϕ_e	0.5

known. The motion of the interface is governed by the following relation:

$$x_{\text{int}}(t) = 2\beta\sqrt{\lambda_v t}\,. \tag{3.21}$$

Where λ_v is the thermal diffusivity, and β is a scaling value defined as

$$\lambda_v = \frac{k_v}{\rho_v c_{pv}}\,, \tag{3.22}$$

$$\beta \exp\left(\beta^2\right)\operatorname{erf}(\beta) = \frac{c_{pv}\left(T_0 - T_{\text{sat}}\right)}{\sqrt{\pi}h_e}\,. \tag{3.23}$$

In the simulation, the domain is 1 mm long, and the temperature boundary conditions are $T_{\text{sat}} = 373.15\,\mathrm{K}$, and $T_0 = 383.15\,\mathrm{K}$. To initialize the simulation, the interface is offset from the left wall by 0.001 mm. The liquid and vapor properties used are shown in Table 3.1.

The large values for liquid density and thermal conductivity allow for a high heat diffusion into the liquid so that the interface is always near the saturation temperature. Figure 3.6 shows interface locations from the numerical simulation and the analytical solution for varying vapor thermal conductivity. The analytical and numerical results show good agreement.

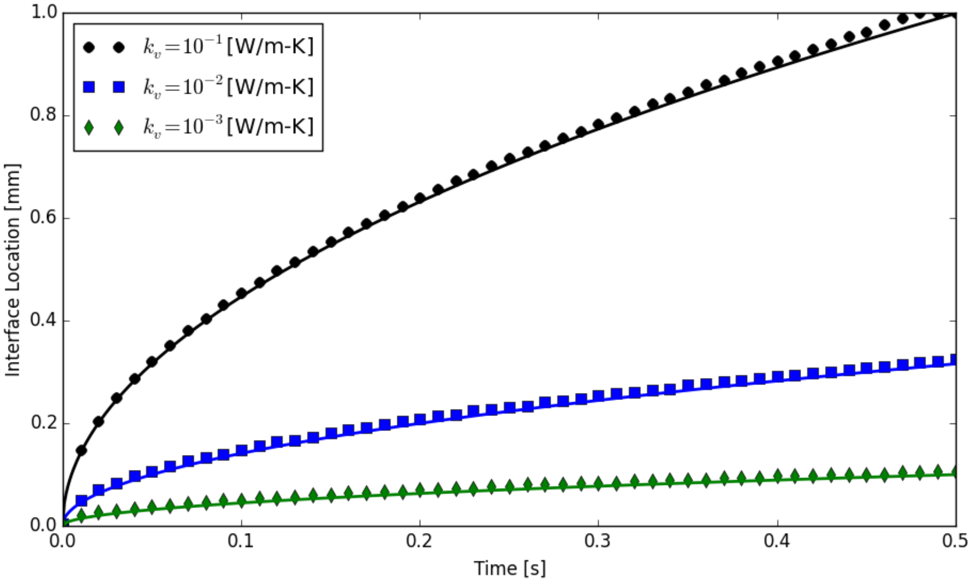

Figure 3.6: Numerical and analytical values of the location of the liquid-vapor interface over time for the Stefan problem.

CHAPTER 4

FALLING FILM EVAPORATION

4.1 Background

The first investigations into the characteristics of a falling liquid film flowing down an inclined plane were conducted by Kapitza. Kapitza identified an important dimensionless group by relating the surface tension with the force of inertia in the fluid which was driven by gravity [41]. This dimensionless group, the Kapitza number, is very useful in the study of wave growth and instability in falling liquid films. If the Reynolds number is below a critical value which is a function of the Kapitza number, the liquid film flow would be uniformly laminar.

Since Kapitza, many other investigators have contributed to our understanding of the flow characteristics of falling liquid films. The work of Alekseenko et al. focused on two-dimensional isothermal films and through experimental measurements characterized the local velocity profile [42]. Work by Kungui et al. studied separation vortices in the connecting region between solitary and capillary waves, and showed these separation vortices increase wall shear stress and enhance crosswise film transport [15].

Long wavelength deformations form on the interface of thin liquid film flowing down an inclined plate. The wavelength of these deformations is much greater than the film thickness. This instability has three different causes: the effect of gravity in the streamwise direction, inertia in the film, and the effect of gravity in the crosswise direction [43].

With regards to black liquor falling films, Johansson et al. experimentally studied the hydrodynamics and heat transfer of black liquor falling film for laminar and turbulent flow conditions during evaporation. [44, 45]. These authors characterized fundamental differences in free surface wave flow structures for evaporating falling films of water and black liquor at similar film Reynolds numbers. In particular, bubble formation was observed only in evaporating black liquor falling films, which was attributed to a combination of surface-active agents and air or vapor entrainment due to free surface wave-breaking. Johansson et al. proposed correlations for predicting black liquor falling film evaporation heat transfer coefficient for laminar, turbulent, and transitional flow regimes. Numerical experiments for evaporating black liquor have be conducted by Chen and Gao [46]. These authors simulated black liquor falling film evaporation based on elliptic incompressible Navier-Stokes equations in 2D. They assumed a flat free surface for the falling film with liquid vaporization taking place within the film rather than limited to only the free surface evaporation.

This chapter focuses on the analysis of wavy-laminar 2-D Newtonian and black liquor falling films based on numerical solution of the transient Navier-Stokes equations on a highly resolved grid. The conservation laws for the transport of heat and species are accomplished with source terms describing interfacial evaporation and species enrichment. This study investigates the fundamental structure of black liquor falling film interfacial waves at high dry solid mass fraction for specified flow inlet perturbation.

4.2 Mathematical Model

A depiction of the falling film domain is shown in Figure 4.1. The thin film enters the top of the with a prescribed half-Poiseuille velocity profile. The film flows along the vertical plate, pulled by gravity to the bottom of the domain. The steam is in contact with the liquid film and it has a density and viscosity much smaller than the liquid.

A detailed description of the governing equations is given in Section 2.1.1, but

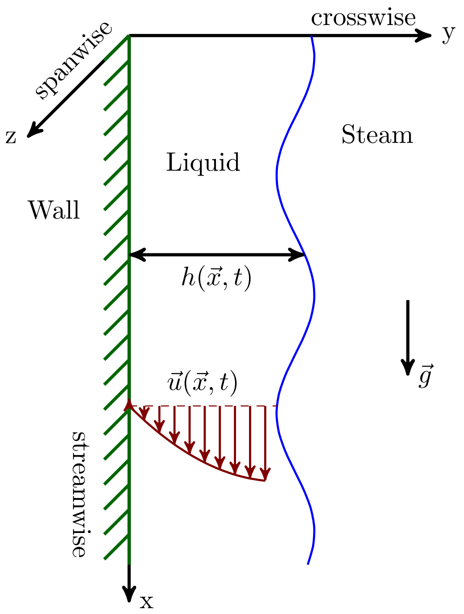

Figure 4.1: Diagram of falling film.

a short description with be given here. The two fluids, liquid film and steam, are simulated as a single-fluid field. The special parameter α is used to indicate the portion cell containing the liquid, and the remaining portion of the contains the steam. The fluid properties of the single-fluid field are calculated from the interpolation of component fluid properties. For example, $\phi = \alpha\phi_l + (1-\alpha)\phi_v$. The conservation equation for the fluid phase is represented as

$$\frac{\partial \alpha}{\partial t} + \nabla \cdot (\vec{v}\alpha) + \nabla \cdot (\vec{v}_r \alpha(1-\alpha)) = -\dot{S}_v \, . \tag{4.1}$$

From the single-field formulation, the respective phase equations, continuity, momentum, and energy for the two-phase flow field are expressed as:

$$\frac{\partial \rho}{\partial t} + \nabla \cdot \rho\vec{v} = 0 \tag{4.2}$$

$$\frac{\partial \rho\vec{v}}{\partial t} + \nabla \cdot \rho\vec{v}\vec{v} = -\nabla p + \nabla \cdot \vec{\tau} + \rho\vec{g} + \vec{F}_{CSF} \tag{4.3}$$

$$\frac{\partial \rho c_p T}{\partial t} + \nabla \cdot (\rho\vec{v}c_p T) = \nabla \cdot k\nabla T - \dot{S}_q \, . \tag{4.4}$$

For simulations in this chapter that use black liquor as the film liquid, the dry-solids content is treated as a scalar that is convected with the flow. The species conservation equation is

$$\frac{\partial \chi_S}{\partial t} + \nabla \cdot \rho \vec{v} \chi_S = \nabla \cdot \rho \xi \nabla \chi_S + \dot{S}_m \,. \tag{4.5}$$

The physical presence of salt crystals that form in the liquid film due to crystallization is not explicitly captured in this formulation.

4.2.1 Important Parameters

Nusselt Film Values

There are several parameters that are important for a discussion of a falling liquid film. The Nusselt film values are vital for describing falling film flows. The average velocity, u_N, and film thickness, h_N, of a fully develop falling film are calculated as:

$$u_N = \left(\frac{Re^2 \mu_l g}{3\rho_l} \right)^{1/3} \tag{4.6}$$

$$h_N = \left(\frac{3 Re \mu_l^2}{\rho_l^2 g} \right)^{1/3} \,. \tag{4.7}$$

Where ρ_l and μ_l represent the density and kinematic viscosity of the liquid film. These terms are derived from the classical Nusselt flat film theory. Nusselt, whose classical analysis focused on the condensation of falling films, made the assumption of a flat free surface.

Reynolds Number

The Reynolds number relates the magnitude of the inertial forces present in the film to the viscous forces. For this flow arrangement it is calculated as

$$Re = \frac{\rho_l u_N h_N}{\mu_l} \,. \tag{4.8}$$

Kapitza Number

The Kapitza number compares the surface tension force, $\sigma(\nu^2/g)^{1/3}$, to the force of inertia, $\rho\nu^2$:

$$Ka = \frac{\sigma}{\rho_l \nu_l^{4/3} g^{1/3}} \,. \tag{4.9}$$

Where σ and ν_l represent the surface tension and the dynamic viscosity of the liquid film. And g is the magnitude of gravity. The flow parameters drop out of the calculation of the force of inertia and the Kapitza number becomes a function of only fluid properties and the angle of the flat surface. Equation 4.9 is the relationship for a vertical falling film, since that is the only arrangement used in the evaporators.

Weber Number

The Weber number is used to assess surface deformability due to the flow. It relates the viscous normal stress at the film surface to the surface tension:

$$We = \frac{\rho_l u_N^2 h_N}{\sigma} \,. \tag{4.10}$$

For small values of the Weber number, the fluid flow is driven by surface tension, while for falling films with large Weber numbers gravity dominates. Small values of Weber number mean that the viscous forces due to the flow are not strong enough to generate pressure that can deform the film surface.

Grashof Number

The Grashof number is defined as:

$$Gr = \frac{g \Delta \rho L^3}{\rho \nu^2} \,. \tag{4.11}$$

And it represents buoyancy forces to viscous forces. For simulation with black liquor, a typical scenario with a dry solids rise of 5 %, change in temperature of 5 K, and film thickness of 2.5 mm leads to a Grashof number on the order of 4.

Richardson Number

The Richardson number represents the ratio of buoyancy forces to inertial forces. And it is defined as:

$$Ri = \frac{g \Delta \rho L}{\rho u_N^2} \,. \tag{4.12}$$

For simulation involving black liquor changes in temperature and dry solids content create changes in the fluid density. A typical scenario with a dry solids rise of 5 %, change in temperature of 5 K, film thickness of 2.5 mm, and velocity of 0.5 m/s leads to a Richardson number of 0.002. It is common to consider flows with a Richardson number smaller 0.1 to have negligible natural convection.

4.2.2 Boundary Conditions

The liquid inlet thickness is calculated from the Nusselt film thickness. The desired film Reynolds number and fluid properties must be selected before hand. At the inlet, the falling film values are specified for the phase indicator, and temperature of the incoming fluid: $\alpha = 1$, $T = T_{l,\text{inlet}}$. If the fluid being modeled is black liquor, the dry solids content is specified as $\chi_S = \chi_{S,\text{inlet}}$. The inlet velocity is specified using as a half-Poiseuille velocity profile using the Nusselt film velocity as the crosswise mean velocity.

$$u_{\text{inlet}} = \frac{3}{2}\left[2\left(\frac{y}{h_N}\right) - \left(\frac{y}{h_N}\right)^2\right]\left[1 + \epsilon \sin\left(2\pi f t\right)\right] u_N \,. \tag{4.13}$$

To encourage the development of interfacial waves, the inlet velocity will be disturbed by a small perturbation, ϵ, with a driving frequency, f. This type of perturbation occurs in practice due to the pumps that carry the black liquor to the top of the falling film.

The gas inlet face is set to all the space above the liquid inlet face. The gas inlet values are set to $\alpha = 0$, $T = T_{g,\text{inlet}}$, $\chi_S = 0$. The gas is allowed to be pulled with the flow, the velocity inlet boundary condition is $\partial u/\partial x = 0$.

For fluid in contact with a stationary wall, the no-slip boundary condition is applied: $u = 0$, $v = 0$. To simulate the heat transfer from the evaporator surface due a condensing steam a constant wall temperature is specified, $T = T_{\text{wall}}$. The other required parameters are set so that there is no mass flux through the wall: $\partial\alpha/\partial x = 0$, $\partial\chi_S/\partial x = 0$.

At the side opposite the stationary wall and bottom outlet of the domain the fluid is able to freely leave the domain. The phase indicator, velocity, temperature, and species at the sides and outlet of the domain have a zero gradient: $\partial \alpha / \partial x = 0$, $\partial u / \partial x = 0$, $\partial v / \partial x = 0$, $\partial T / \partial x = 0$, and $\partial \chi_S / \partial x = 0$.

The domain for these simulations has a very large aspect ratio, typically around 100:1. Cell in the domain reflect this stretched aspect ratio by being slightly stretch in the streamwise direction. An example of the mesh is shown in Figures 4.2 and 4.3. Figure 4.2 shows the inlet of the domain. Figure 4.3 shows the region between two waves captured 0.8 m downstream. The mesh used in the falling film simulation is slightly stretched in the crosswise direction so that cells near the heat transfer surface

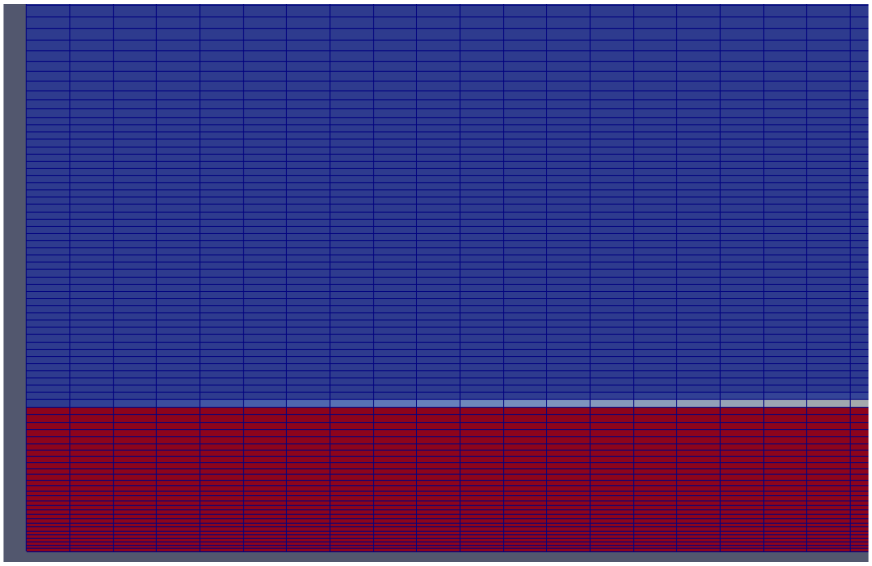

Figure 4.2: Mesh for falling film simulations. Domain inlet is shown. Gravity pulls to the right.

4.3 Numerical Validation

Two sets of simulations are conducted to ensue that results from the numerical model conform to reality. The first validation simulation measures the heat transfer coefficient along the streamwise direction for a heated falling film. And the second simulation verifies the heat transfer can also be matched for black liquor flows.

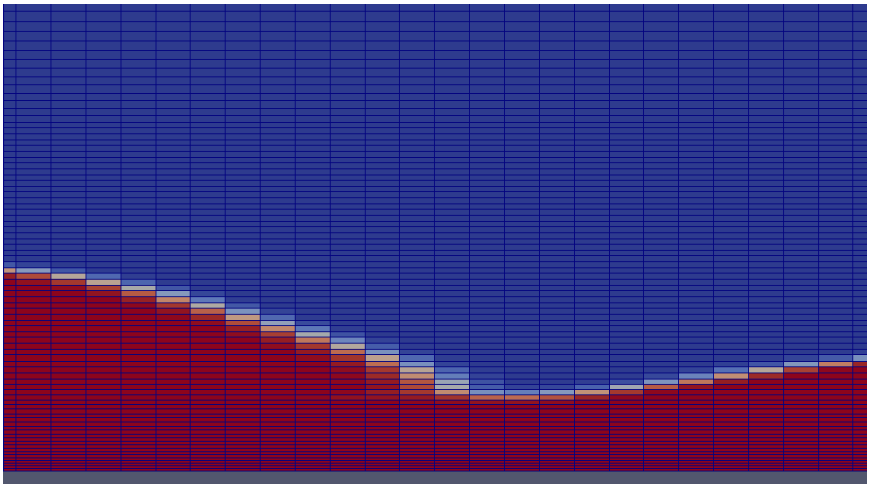

Figure 4.3: Mesh for falling film simulation. Image of shows region 0.8 m downstream. Gravity pulls to the right.

4.3.1 Heat Transfer Coefficient

The following simulations measure the heat transfer coefficient for the heat falling film and compare the results to relations derived from experimental results. The heat transfer coefficient is calculated as

$$h(x,t) = \frac{\dot{q}''(x,t)}{T_{\text{wall}} - T_I(x,t)}\,. \tag{4.14}$$

Where $\dot{q}''$ is the wall heat flux, and T_I is the temperature at the liquid interface. The wall heat flux is calculated as

$$\dot{q}'' = -k\frac{T_{\text{wall}} - T_{\text{near}}}{\Delta y}\,. \tag{4.15}$$

Where T_{near} is the temperature measurement taken a small distance, Δy, in the crosswise direction. Once the curve for the heat transfer coefficient is known it can be averaged over the streamwise distance and time,

$$h_{\text{avg}} = \frac{1}{N_t}\sum_{1}^{N_j}\frac{1}{L}\int\limits_{0}^{L} h(x,t)dx\,. \tag{4.16}$$

the value N_j is the number of time steps. The Nusselt number is then calculated as

$$Nu_{\text{avg}} = \frac{h_{\text{avg}} l_v}{k_l}\,. \tag{4.17}$$

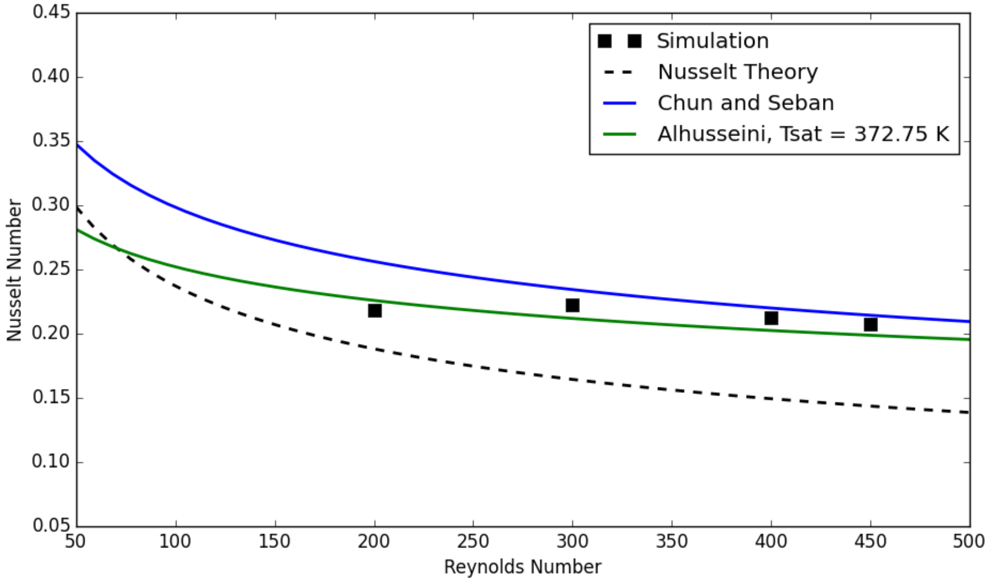

Figure 4.4: Heat transfer coefficient to falling liquid film.

In this equation, the parameter l_v represents the viscous length scale.

Figure 4.4 shows Nusselt number values for various Reynolds number as compared to experimental results. The Nusselt number from Nusselt's flat film theory is

$$Nu_{\text{avg}} = \left(\frac{4}{3}\right)^{1/3} Re^{-1/3}\,. \tag{4.18}$$

A relationship for average Nusselt number determined Chun and Seban [47]:

$$Nu_{\text{avg}} = 0.822 Re^{-0.22}\,. \tag{4.19}$$

Alhusseini [48] produced a relationship for the average Nusselt number as well. For a liquid with a Kapitza number of 2.92×10^{-13} the relationship at a temperature of 372.15 K is

$$Nu_{\text{avg}} = 2.65 Ka^{0.0563} Re^{-0.158}\,. \tag{4.20}$$

Results for the Nusselt number show good correspondence with the analytical and experimental relationships.

Comparisons to experimental results of the heat transfer coefficient for black liquor simulations using this computational model was conducted by Doro [39].

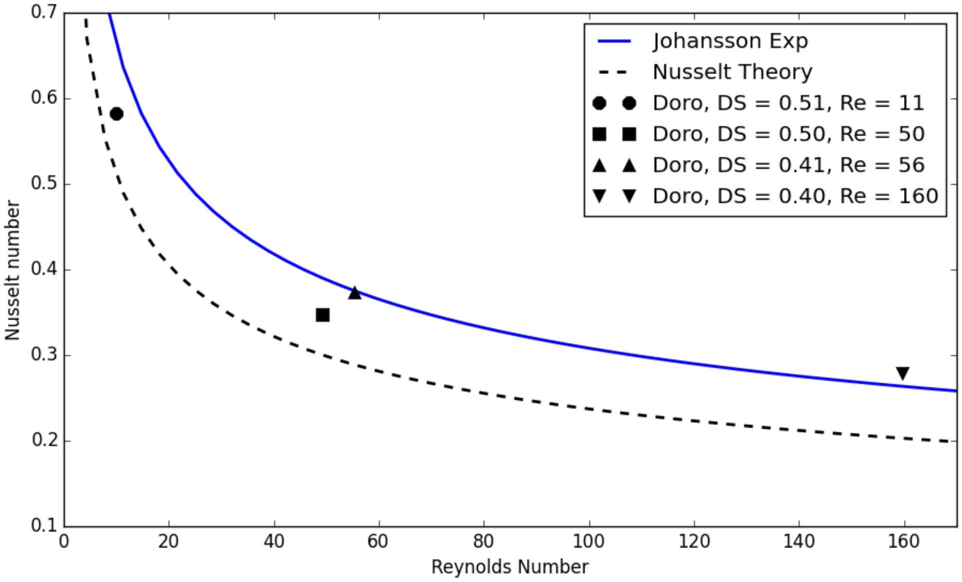

Figure 4.5: Comparison of average Nusselt number for black liquor flow to physical experiment correlations and Nusselt flat film theory [39].

Figure 4.5 shows a comparison of the Nusselt number for black liquor through a range of dry solids values and Reynolds numbers. The simulated results show good agreement with the experimentally determined relationship for Johansson [44]

$$Nu_{\text{avg}} = 1.43 Re^{-1/3} \,. \tag{4.21}$$

4.4 Analysis of Simulation Results

4.4.1 Streamwise Film Temperatures

In this simulation series, a Newtonian falling film flowing down a vertical heated surface will be modeled on a highly resolved grid. This case utilizes the model developed to study the flow structure of the falling film. The range of Reynolds numbers and forcing frequencies are shown in Table 4.1. The goal of this simulation series is to study the effect of forcing frequency on the hydrodynamics and temperature of the film.

Figure 4.6 shows a comparison snapshots of the falling film interface under various flow conditions. From this chart the effect of the Reynolds number and forcing

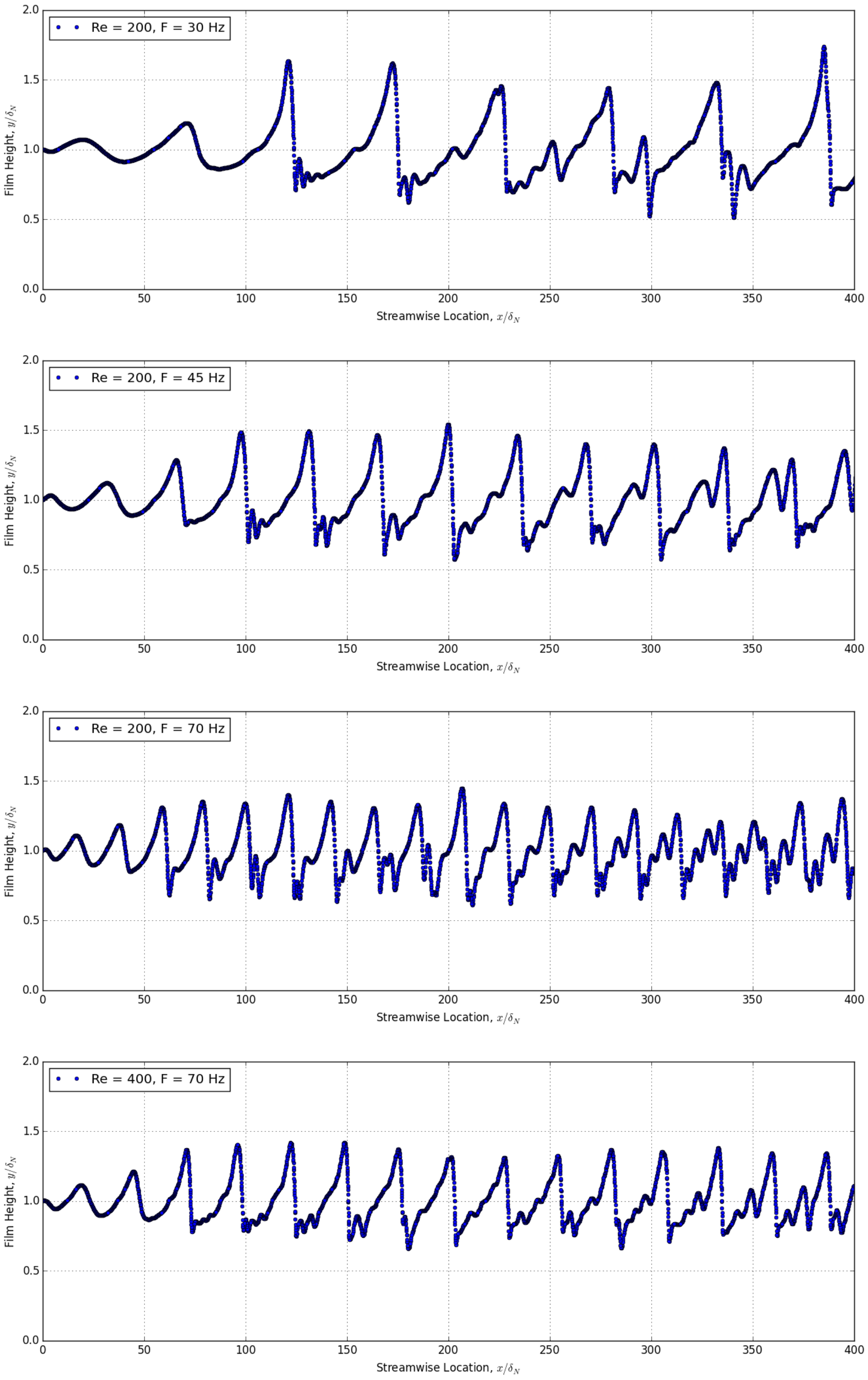

Figure 4.6: The effect of Reynolds number and forcing frequency on the interface of heated falling liquid film.

Table 4.1: Simulations to study the effect of forcing frequency on the hydrodynamics and temperature of a falling film.

Case	T_{sat} [K]	T_{wall} [K]	Re	f [Hz]
1	373.0	383.0	200	30
2	373.0	383.0	200	45
3	373.0	383.0	200	70
4	373.0	383.0	400	30
5	373.0	383.0	400	45
6	373.0	383.0	400	70

frequency on the the interface of the film can be seen. As the forcing frequency increases the magnitude of large waves in the film decreases. The distance between the large humps also contracts increasing the number of large humps that are inside the computational domain. It can also be seen that the small waves that precede the large hump, are also affected by the forcing frequency. In the 30 Hz simulation these waves only exist in the small region directly in front of the large wave. But as the forcing frequency increases, these waves grow in thickness and spread out in front of the large wave, eventually they completely span the space between the large humps.

The third and fourth plots in Figure 4.6 show the effect of Reynolds number on the film with a forcing frequency of 70 Hz. The increase in Reynolds number from 200 to 400 has little affect on the magnitude of the large waves, however the separation distance between these waves increases. The magnitude of the intermediate waves are reduced significantly by this increase in the Reynolds number.

Figure 4.7 shows the crosswise-average liquid temperature as it changes along the streamwise direction. This curve is calculated by numerically creating stations located along the streamwise direction, and then calculating the mass average of temperature along this station. Measurements are taken at N stations along the streamwise direction, and the crosswise direction contains M computational cells.

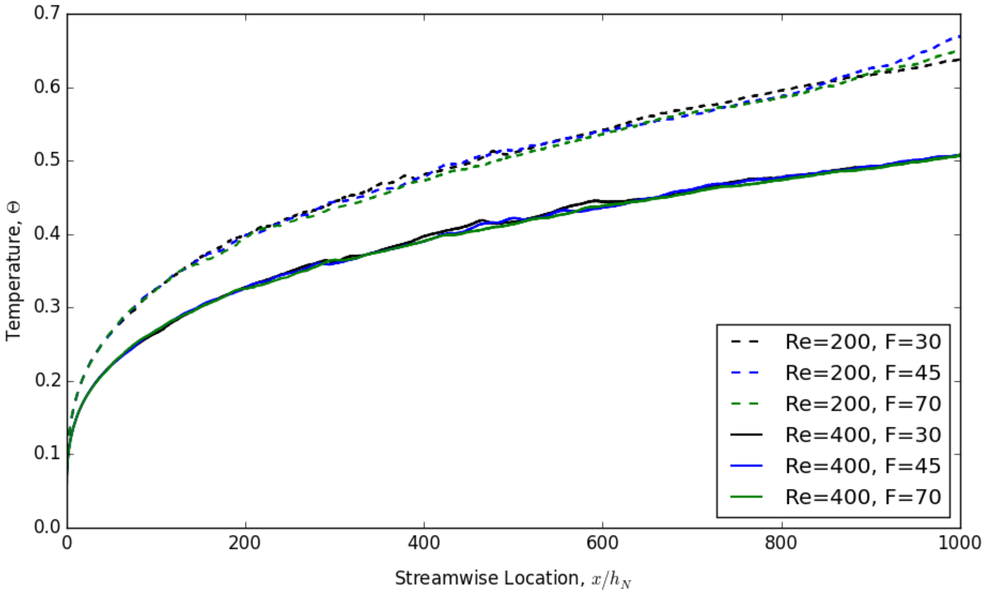

Figure 4.7: Average liquid temperature along the streamwise location of the falling film for Reynolds numbers and forcing frequencies.

The location of a station can be calculated as:

$$x_{\text{st}} = \sum_{i=1}^{N_{\text{st}}} \Delta x_i \, . \tag{4.22}$$

Where Δx_i is spacing between stations in the streamwise direction between the i and $i-1$ station. The crosswise mass average of the temperature is calculated from the following equation,

$$T_{\text{avg}}(x_{\text{st}}) = \frac{\left[\sum\limits_{j=1}^{M} \alpha_j \rho_{l,j} \mathcal{V}_j T_j\right]_{\text{st}}}{\left[\sum\limits_{j=1}^{M} \alpha_j \rho_{l,j} \mathcal{V}_j\right]_{\text{st}}} \, . \tag{4.23}$$

It is shown in Figure 4.7 that as the Reynolds number decreases the average liquid temperature increases. Here the Reynolds number is related to mass flow rate. As the amount and rate of liquid flowing over the heat transfer surface decreases, the heated surface is able to have a greater influence on the film and raise the average temperature of the liquid. The forcing frequency in this simulation has little effect on the average liquid temperature. In this range of frequencies, an increase in the

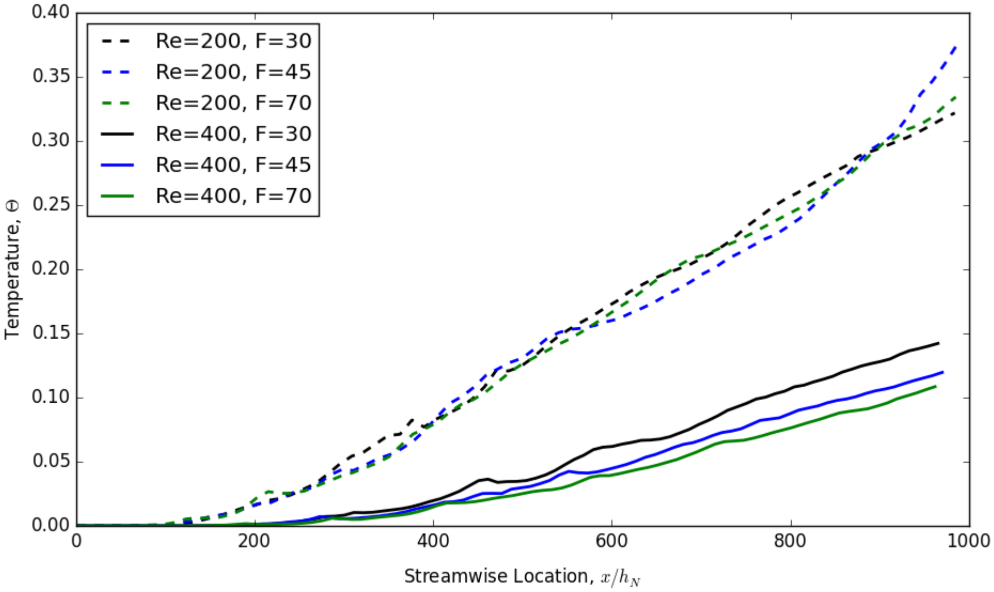

Figure 4.8: Average surface temperature along the streamwise location of the falling film for Reynolds numbers and forcing frequencies.

frequency increases the prominence of the humps in the flow. But the bulk of the fluid near the wall dominates the film temperature averaging, and this fluid is relatively unaffected by the forcing frequency.

Figure 4.8 shows the liquid surface temperature as it changes along the streamwise direction. This curve is calculated by numerically creating stations located along the streamwise direction, isolating cells that only contain the interface, and then calculating the mass average of temperature along this station. The surface temperature is calculated the same way as the average liquid temperature in Equation 4.23, but first filtering for cells that meet the criteria, $0.1 < \alpha < 0.9$. It is shown in Figure 4.8 that the surface temperature profiles group by the Reynolds number. Like with the average liquid temperature, the Reynolds number, and thereby the mass flow rate, has a larger influence on the flow than the forcing frequency. A lower Reynolds number leads to a higher liquid surface temperature. The effect of the forcing frequency is reduced to noise in the case of higher Reynolds number, with no apparent pattern

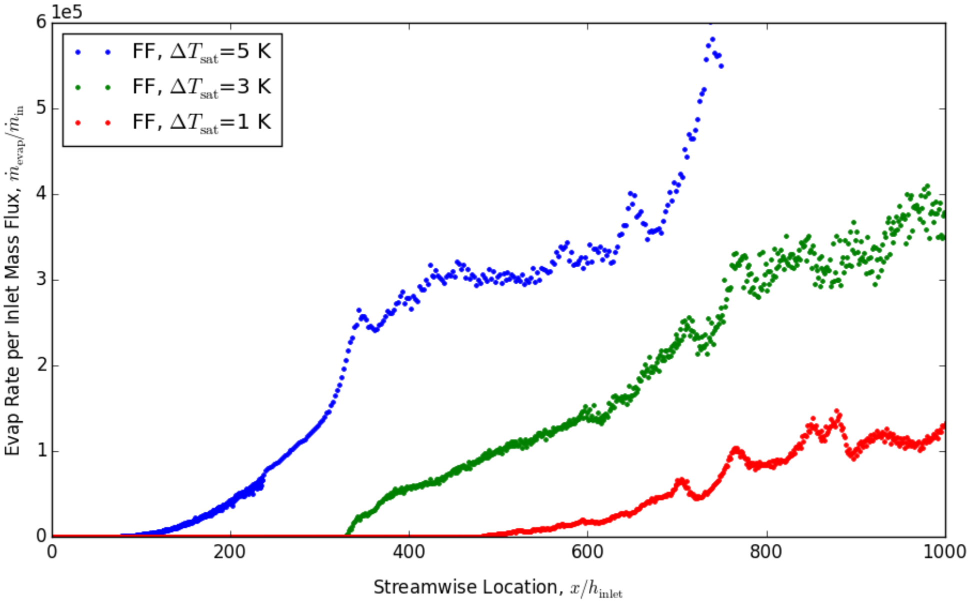

Figure 4.9: Evaporation rates at streamwise locations for excess wall temperature values.

resulting. However for a lower Reynolds number the liquid surface temperature decreases with increasing forcing frequency. In this range of frequencies, an increase in the frequency increases the prominence of the humps in the flow. A study of the temperature profile in these large humps is shown in a later section.

4.4.2 Film Evaporation

The previous section focused on the heat transfer to a falling film. The ultimate aim of this project is to study the concentration of black liquor, so now we include the results of the surface evaporation model.

Figure 4.9 shows the rate of evaporation at various excess wall temperatures above the liquid saturation temperature, ΔT_{sat}. Because of the assumption of constant wall temperature due to the expected phase change of steam on the unmodeled side of the evaporator surface, there is no restriction on the amount of heat that the liquid can receive from the wall. As expected, the higher the excess wall temperature above the saturation temperature, the higher the rate of evaporation that can be achieved in the

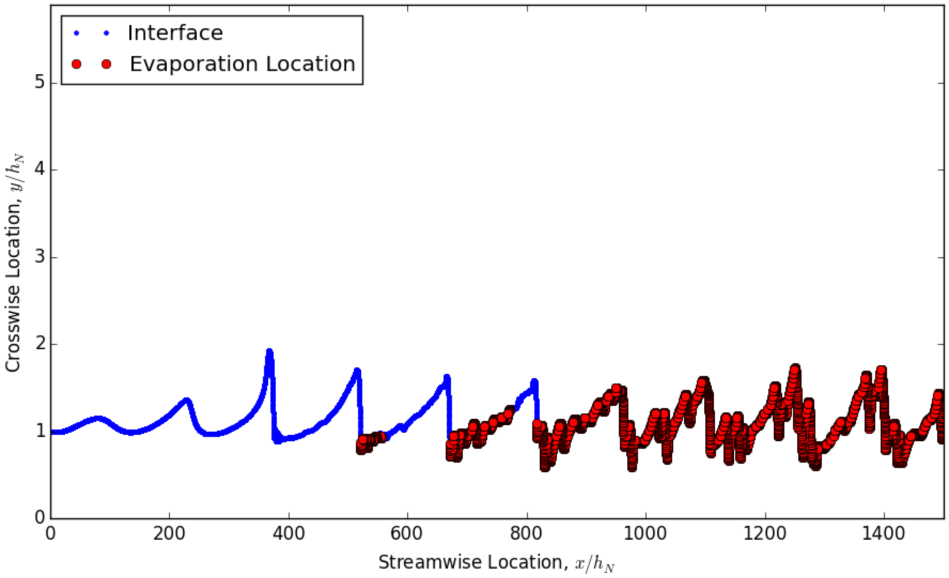

Figure 4.10: Snapshot of simulation that shows the interface and the location on the interface where evaporation occurs.

domain. All three of the simulations have some entrance region where evaporation does not occur. The length of this entrance region is affected by the magnitude of the excess wall temperature. A higher wall temperature shortens this entrance length, because it can raise the film surface temperature to the saturation temperature in a shorter streamwise distance.

Figure 4.10 shows a snapshot of the falling film interface. On this plot, the blue dots show the form of the interface, $\alpha \approx 0.5$. And the red dots indicate location where evaporation is occurring at this timestep regardless of magnitude. From this figure, it can be seen that there are three regions in the flow. There is an entrance length where the film is heating up, and no evaporation is occurring. Then there is an intermediate region where the temperature profile is still developing so evaporation only occurs in thin regions of the film, as described in Section 4.4.4. Finally there is a fully developed region of the flow, where evaporation is occurring along all points of the film.

The wall heat flux along the streamwise direction is shown in Figure 4.11. The

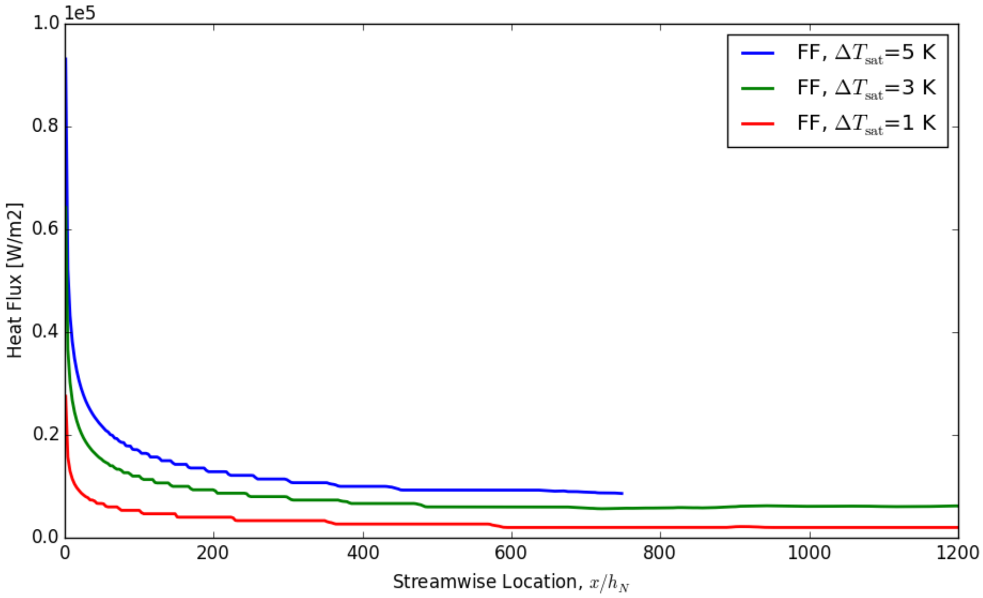

Figure 4.11: Wall heat flux along the streamwise direction.

effect of the constant wall temperature boundary condition is tested here, as at the inlet the heat flux extremely large with no limit on the amount of heat that can be transported through the evaporator surface.

The steam side of the evaporator, where steam is condensing into a liquid is not directly modeled in the simulations. An estimate for the steam consumption, the amount of steam converted to liquid, in the evaporator can be calculated by assuming that all the heat passing through the evaporator wall is from the latent heat of evaporation on the source steam side. This simple relationship is $\dot{m}_{\mathrm{stm,cons}} = \dot{q}''/h_e$. This is an ideal form of the evaporator, and is expected to under predict the amount of steam converted into liquid.

Using the wall heat flux from Figure 4.11, the steam consumption for this simulation is calculated and shown in Figure 4.12 The large temperature difference at the inlet between the liquid film and the fixed wall temperature boundary conditions means that a large amount of heat is allowed to move through the heat transfer surface. Moving downstream, the near wall temperature rises due to this heat flux and

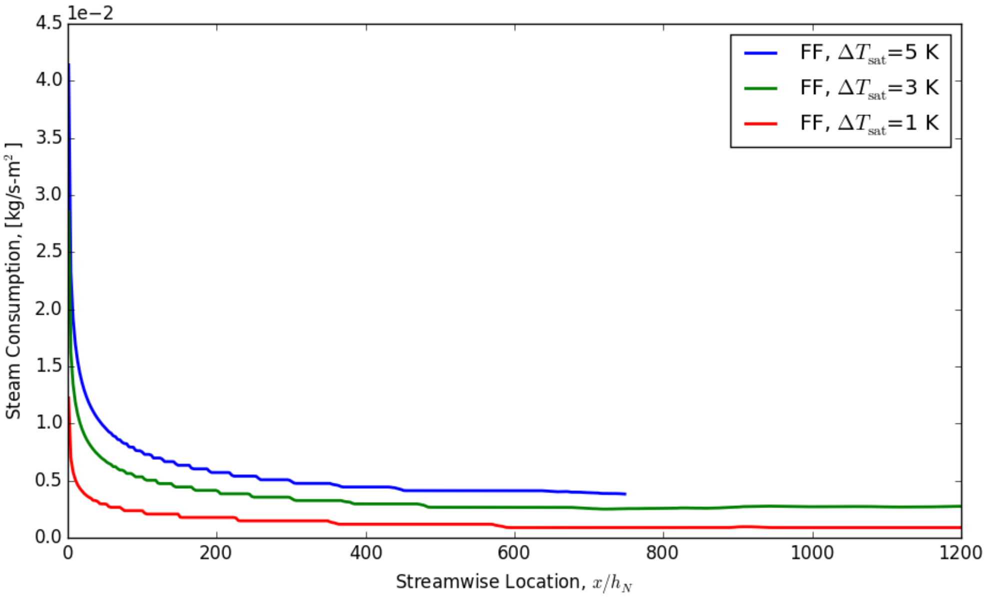

Figure 4.12: Calculated steam consumption in the streamwise direction.

the rate of heat entering the liquid drops off accordingly. The relationship used to determine the steam consumption rate is proportional to the wall heat flux. The global steam consumption rate is calculated by averaging the wall heat transfer over time and the integrating over the domain,

$$\dot{q}''_{\text{avg}}(x) = \frac{1}{N_t} \sum_{1}^{N_t} \dot{q}''(x,t) \tag{4.24}$$

$$\dot{m}_{\text{stm,cons}} = \frac{1}{L} \int_{0}^{L} \frac{\dot{q}''_{\text{avg}}(x)}{h_e} dx\,. \tag{4.25}$$

Where L is the length of the domain, and N_t is the number of time steps used in the averaging process.

Figures 4.13, 4.14, and 4.15 show the global mass evaporation rates, steam consumption rates, and steam efficiency for evaporator lengths. These are not values measured at a specific streamwise location, but global values that are calculated cumulatively along the streamwise distance of the simulation domain.

Figure 4.13 shows calculated steam consumption rates as a function of evaporator length for the various wall temperatures. As expected, the higher the wall excess

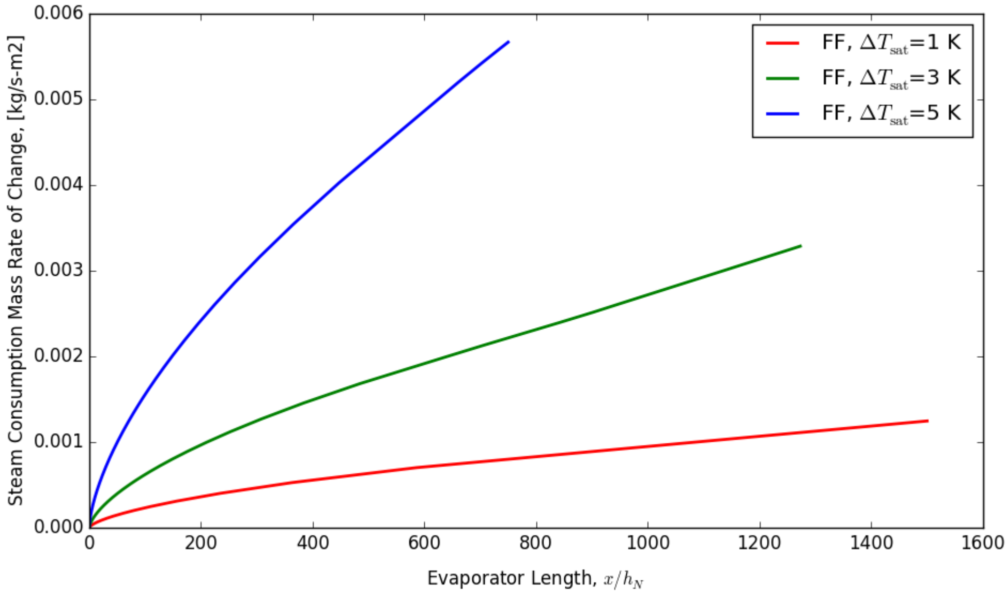

Figure 4.13: Global steam consumption rates for evaporator lengths of increasing size for a Newtonian falling film.

temperature the greater the rate of steam consumption by the evaporator.

And Figure 4.14 shows how liquid mass evaporation rates vary with evaporator length. Close to the inlet no evaporator is occurring, because the wall temperature has not yet had an effect on the liquid interface. At the location where evaporation does begin to occur, the rate increases very slowly with evaporator length. However the rate does continue to grow with evaporator length. For long evaporator, increasing the domain length has a strong effect on increasing the global evaporator rate of the liquid.

The global steam efficiency for these cases of a Newtonian falling film is shown in Figure 4.15. The analysis of the evaporation data suggests that increasing the evaporator length will increase the steam efficiency. Interestingly, the rate of increasing efficiency per evaporator length for all the simulations have tended to settle in a similar slope.

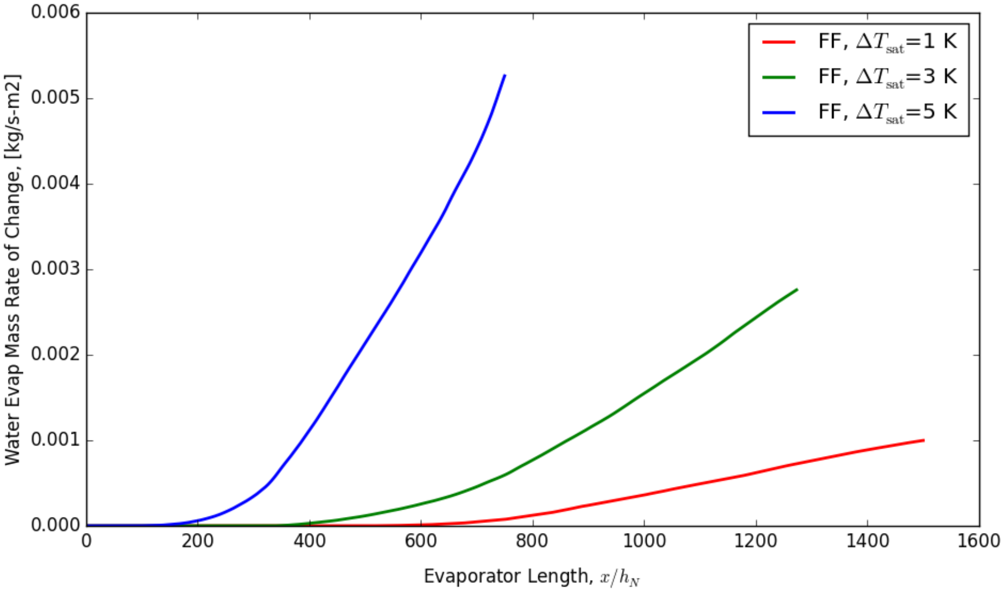

Figure 4.14: Global liquid mass evaporation rates for evaporator lengths of increasing size for a Newtonian falling film.

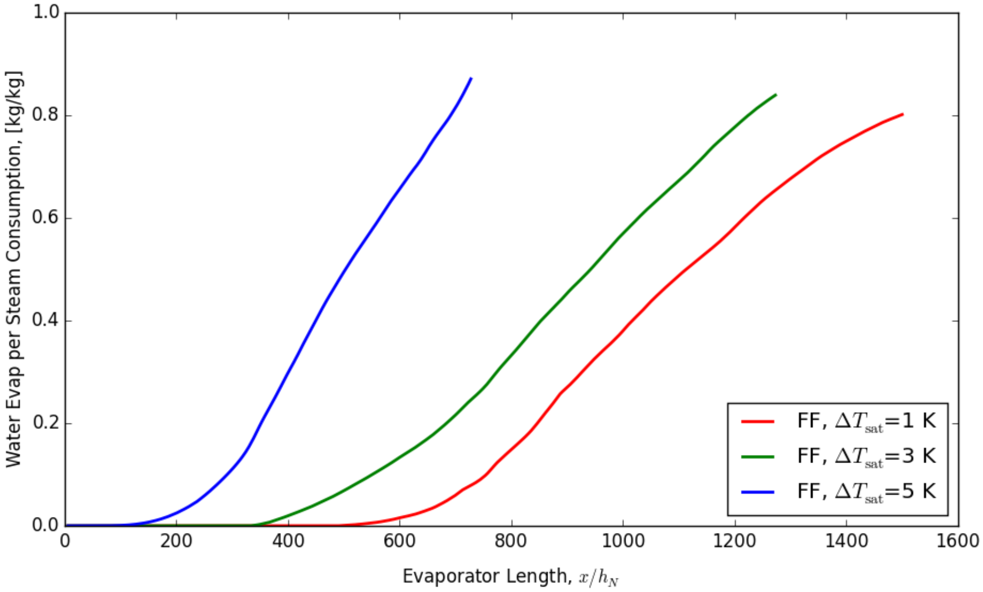

Figure 4.15: Steam efficiency for evaporator lengths of increasing size for a Newtonian falling film.

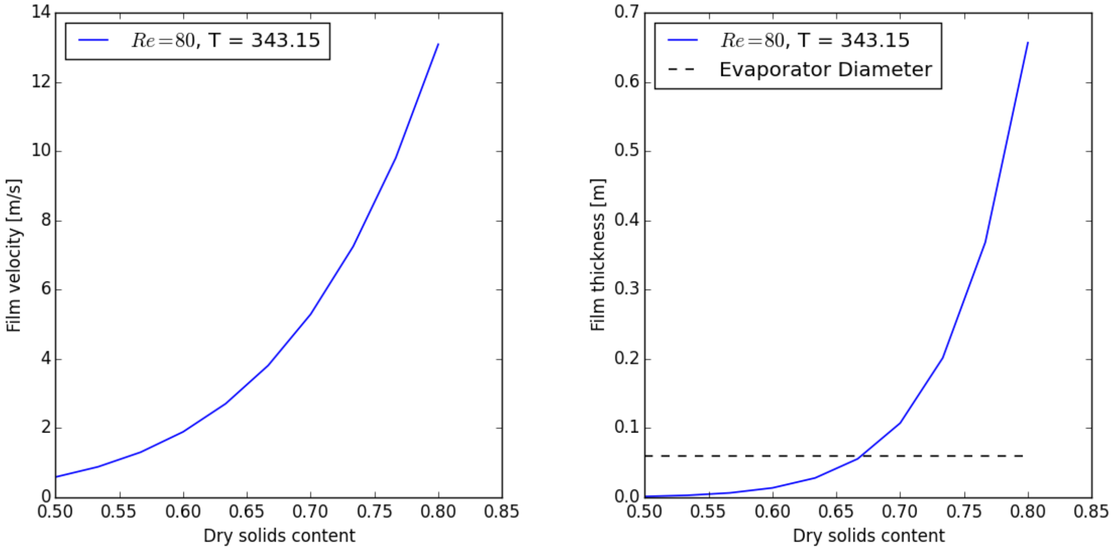

Figure 4.16: Challenges with simulating black liquor flows while with fixed Reynolds number. Increasing Nusselt film values with dry solids content. Dashed line shows tube diameter for a typical falling film evaporator.

4.4.3 Black Liquor Falling Film

The computational model has been used to investigate the nature of the transport mechanics for a heated falling film. Now the model will be utilized to study the effects of non-Newtonian properties of black liquor.

Ideally, the simulation series would use a constant Reynolds number as a control, but the extreme range of black liquor fluid properties over a range of dry solids content makes fixing the Reynolds number very challenging. Using the Nusselt film values as an inlet condition for the simulations, means that as dry solids content grows large, the required inlet film thickness and inlet velocities become unreasonable. Figure 4.16 shows the Nusselt film thickness and Nusselt film velocity or a range of dry solids content for a small Reynolds number of 8. To illustrate the problem, the dashed line in this figure shows the diameter of a typically falling film evaporator that might be used by a paper mill, 60 mm.

To account for these problems, simulations using a black liquor falling film do not use a fixed Reynolds number but a fixed mass flow rate instead.

4.4.3.1 Effect of Dry Solids

As water is evaporated out of the black liquor, the dry solids content will increase. The percentage of dry solids is an important property affecting the thermodynamic and rheological properties of black liquor. The following sets of simulations described in Table 4.2, are conducted to investigate the effect of increasing dry solids on the film hydrodynamics.

Table 4.2: Simulations series to study the effect of dry solids content on black liquor hydrodynamics.

Case	$\dot{m}_{2\mathrm{D}}$ [kg/s m]	χ_S	$T_{\mathrm{liq,in}}$ [K]	f [Hz]	h_N [m]
1	1.0	0.5	343.0	30	0.0013
2	1.0	0.55	343.0	30	0.0024
3	1.0	0.6	343.0	30	0.0042

The numerical model allows for a view into the hydrodynamics. Figures 4.17 and 4.18 show a snapshot for interface profile and interfacial temperature for three simulations of Table 4.2. These black liquor simulations use an inlet mass flow rate of 1 kg/m s and a dry solids content of 50 %, 55 %, and 60 %. The inlet temperature is 343.0 K and the uniform wall temperature is 353.0 K. The forcing frequency is 30 Hz for all flows. For the 50 % dry solids, after the initial entrance region, the solitary wave heights remain very consistent. The spacing of the solitary waves remains very regular as well, until the last fifth of the domain. Very little fluid detaches from the bulk flow in this simulation.

The 55 % dry solids black liquor has a very different interface profile. For the first fifth of the domain, the waves are very regularly spaced and have a similar non-dimensional height to the solitary waves of the 50 % dry solids flow. Further down stream the waves start to coalesce. As these waves start to collide, a large wave

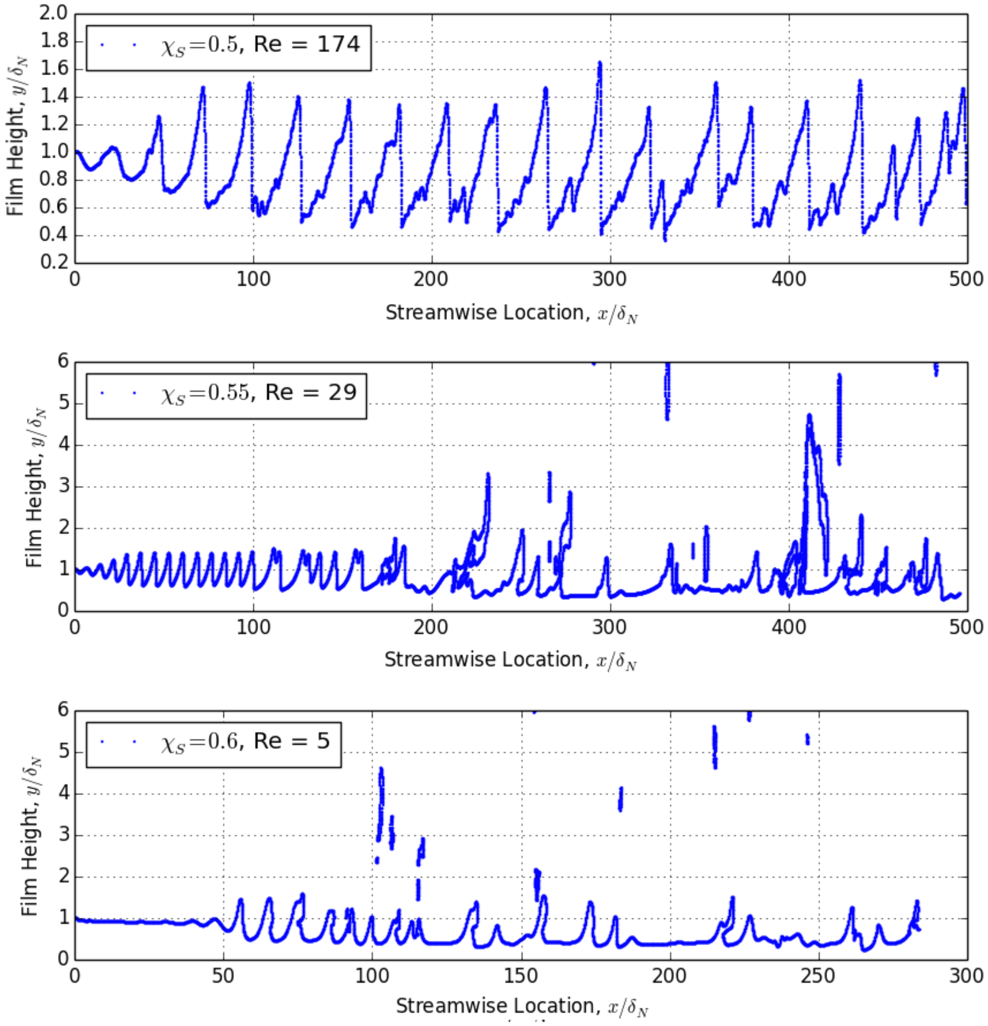

Figure 4.17: Snapshots of interface profiles for black liquor falling films with dry solids content: 50 %, 55 %, 60 %. For all flows the mass flow rate is 1 kg/s m. Lines detached from the interface are segments of fluid that have become detached from the bulk film.

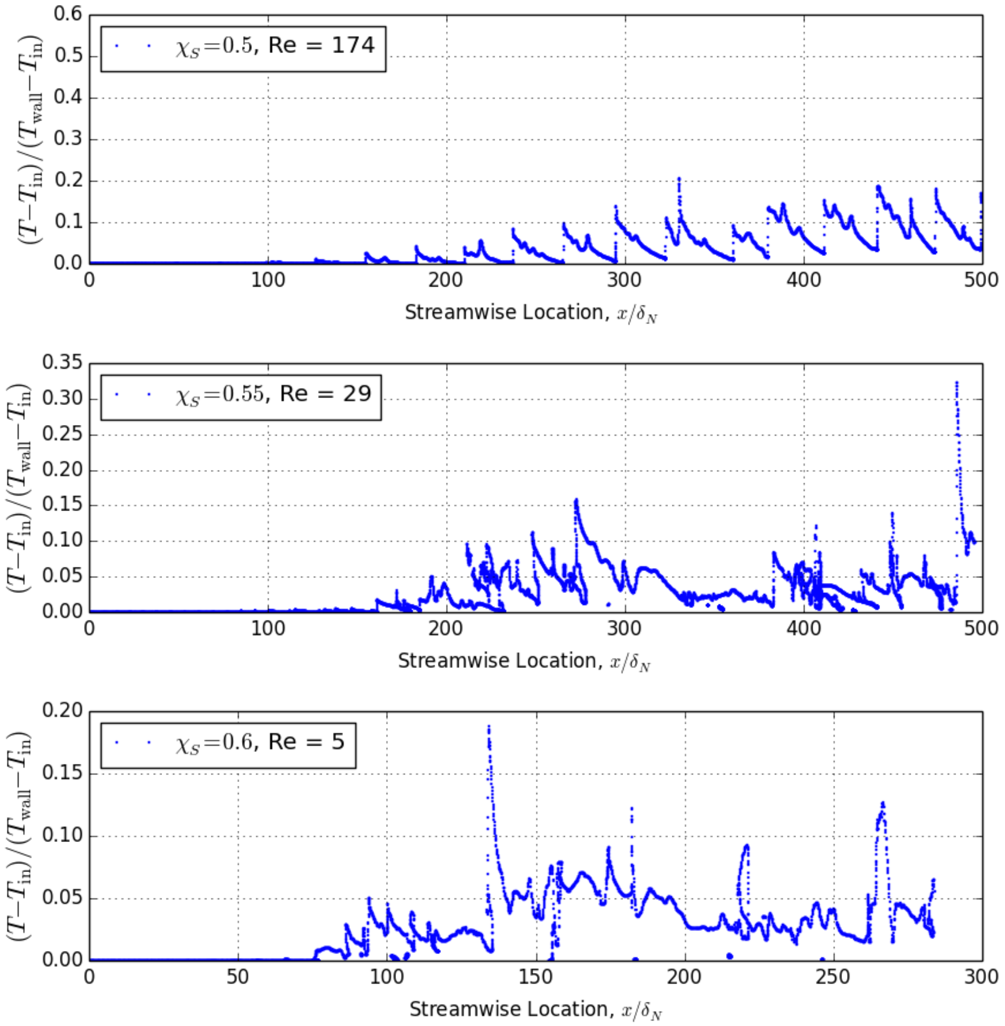

Figure 4.18: Snapshots of interfacial temperature profiles for black liquor flow.

upstream will ramp off of a large wave down stream as it overtakes it. This can cause air entrainment, if the overtaking wave reconnects with the film, or the overtaking wave can disconnect from the bulk flow and free fall separately. Near the location a very large hook-shaped strand can be seen.

Black liquor at 60 % dry solids has a near uniform interface for the first fifth of the domain. At this point, perturbations create rapid growth in the interface height. A large number of strands break off from the flow and free fall through the rest of the domain.

The interfacial temperature for these simulations is shown in Figure 4.18. Overall, simulations with lower dry solids content have a higher interface temperature. For the 50 % dry solids flow, after the entrance region, the temperature profile is very regular and seems to resemble the inverse of the interface profile. This is because the tall solitary wave humps are colder since they require a long time for the temperature to diffuse. The wave-ramping mechanic discussed above can aid in diffusing heat into a solitary wave hump.

4.4.4 Solitary Wave Temperature Profile

It is known that, in the range of frequency studied in the previous section, increasing the forcing frequency increases the size of large solitary waves, or humps, in the film. This section investigates the effect that these humps have on the temperature profile in the film.

In Figure 4.19, the temperature profile at four stations around a solitary wave are shown. The dashed lines indicate the location of the station, and the solid line is a measure of the normalized temperature,

$$\Theta = \frac{T - T_{l,\text{inlet}}}{T_{\text{wall}} - T_{l,\text{inlet}}} \,. \tag{4.26}$$

On the flat plate, the temperature is specified as a boundary condition, expressed as $\Theta = 1$ In the thin region in front of the large hump heat very thorough into the

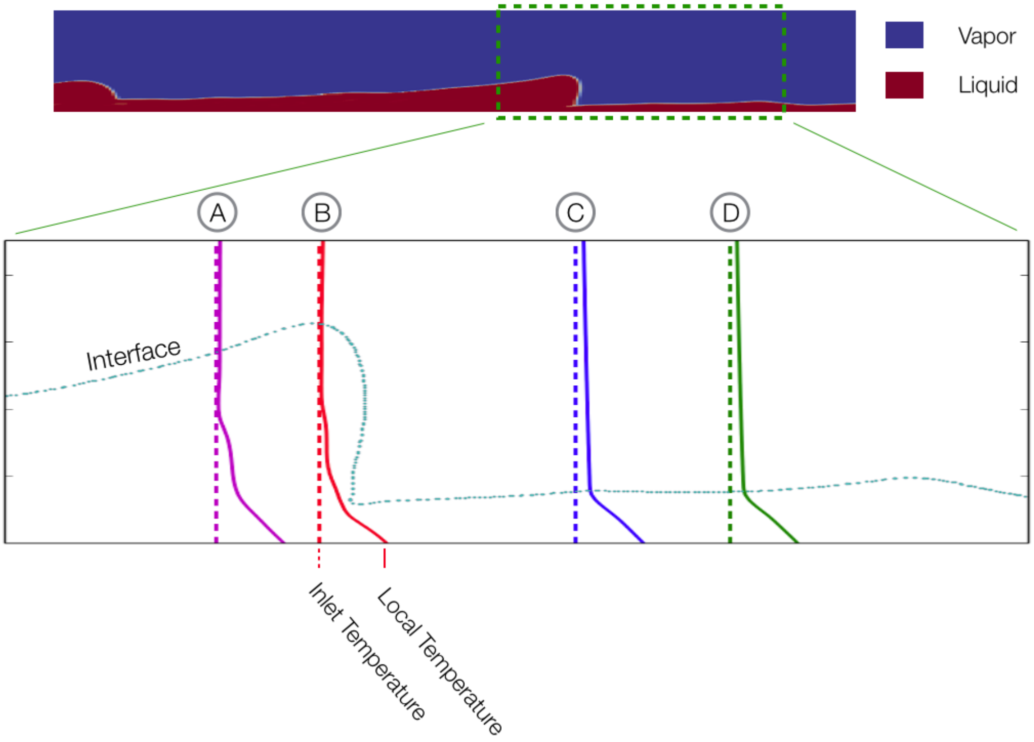

Figure 4.19: Crosswise temperature profile at various stations around a solitary wave far down the simulation domain.

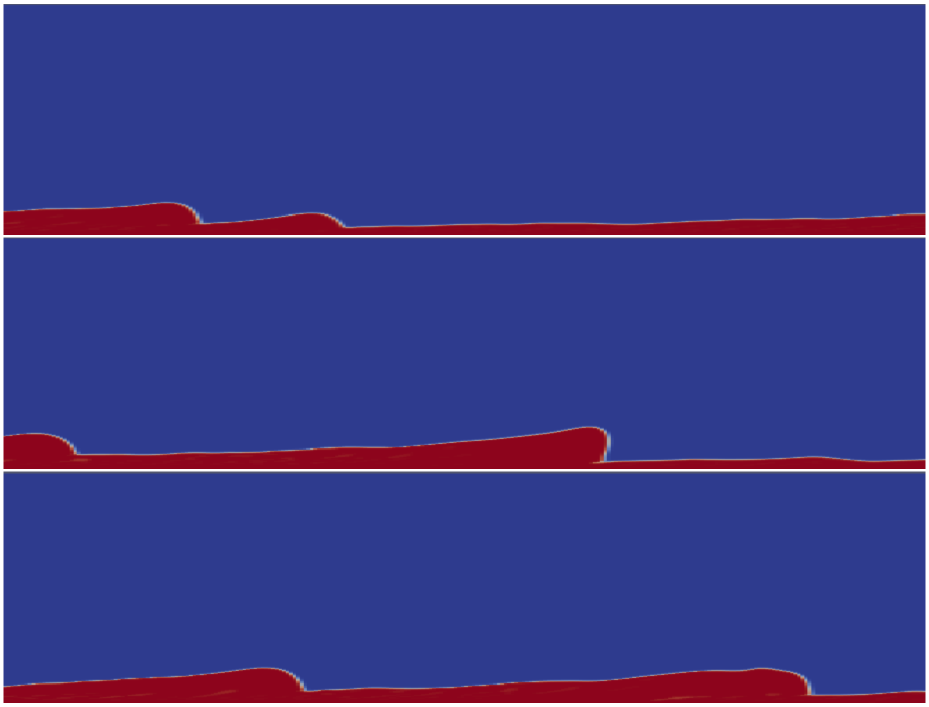

Figure 4.20: Fast moving wave overtaking a slower moving wave.

thin film and the temperature profile is nearly even in these regions. However in the large hump, the temperature profile drops off very quickly as a proportion of the film thickness. The surface temperature in this region has not risen above the liquid inlet temperature, and there is a very unfavorable temperature gradient that limits heat from moving up into the large hump.

Figures 4.21 and 4.22 show the streamwise velocity and temperature profile at various locations before and after two coalescing waves crest and over take the region in front of them. The top of Figure 4.22 shows the nondimensionalized temperature profile approaches zero about halfway up the hump, while the interface of the thin region in front is relatively hot. The bottom of Figure 4.22 shows the temperature profiles after the wave has landed on the front region. A dashed line has been drawn to show the previous interface of the thin film. The cold hump of the wave is now sitting on top of the hot film, and there is a more favorable temperature gradient causing heat to diffuse into the hump.

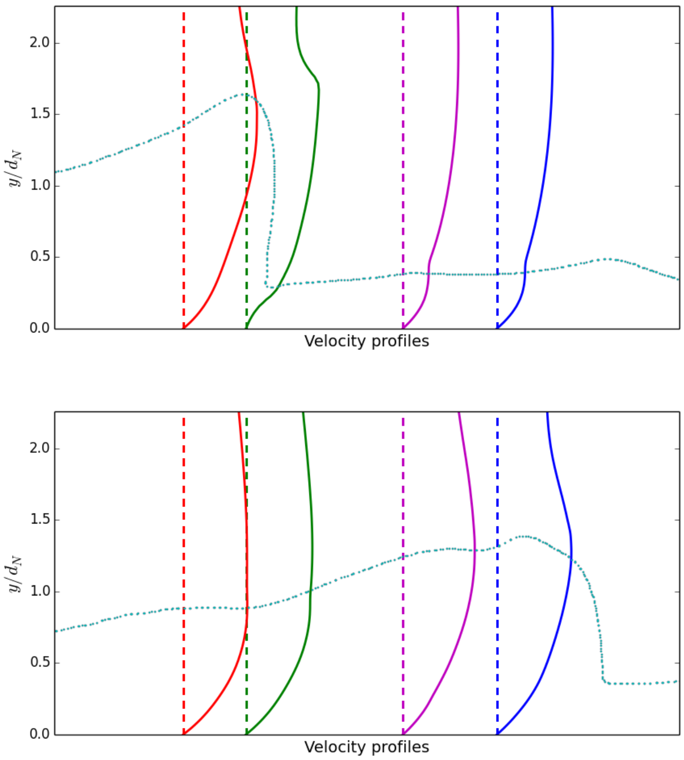

Figure 4.21: Streamwise velocity profiles at various locations around a large solitary wave before and it crests and over takes the region in front. Film is moving the right. Gravity vector points to the right. Dotted teal line indicates location of the interface. Image on top occurs 0.01 seconds before image on bottom. 50 % dry solids content.

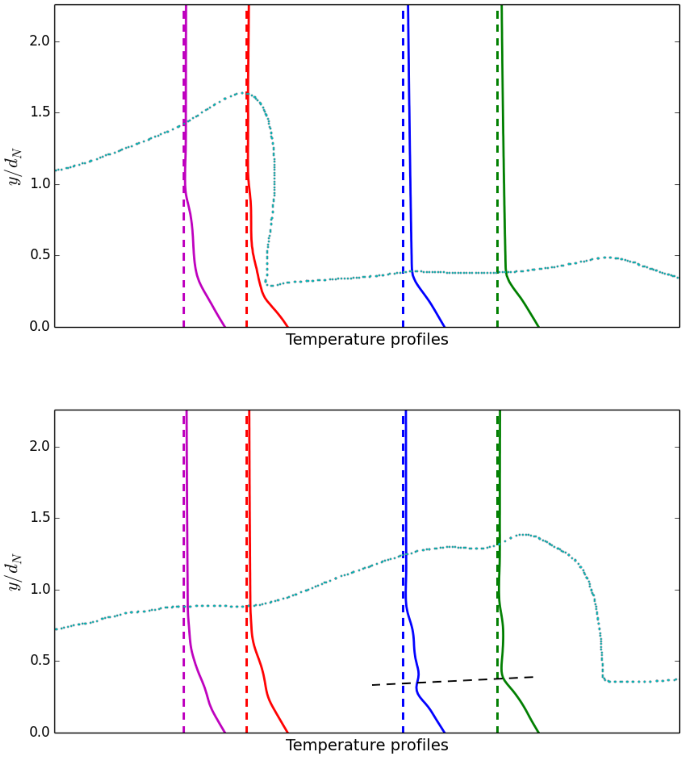

Figure 4.22: Temperature profiles around a large solitary wave before and after it crests and over takes the region in front. Dotted teal line indicates the film interface. The film is moving to the right and the gravity vector points to the right. 50 % dry solids content. See Figure 4.21 for velocity profiles at same locations. The black dashed line represents the division between fluid that was in the capillary wave and fluid that was in the front region.

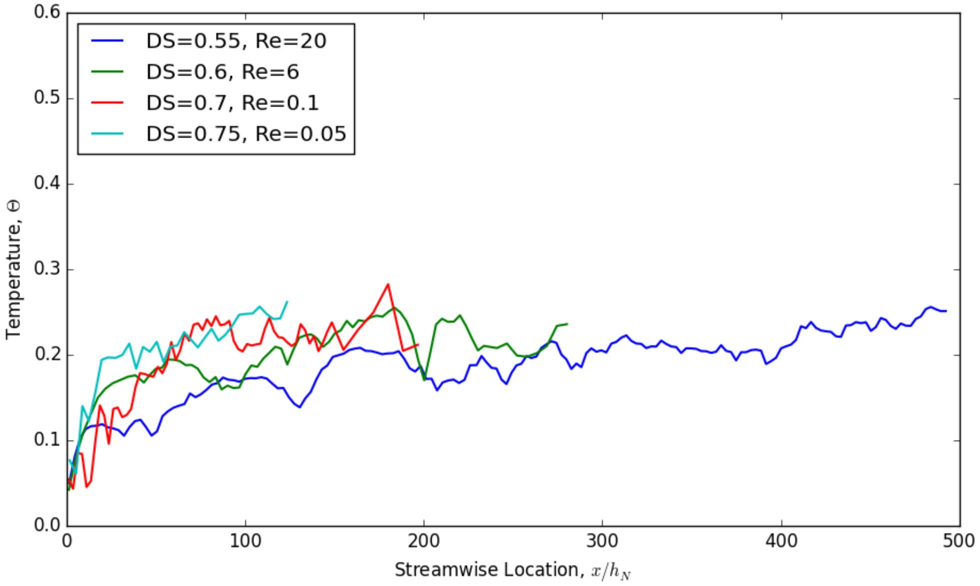

Figure 4.23: Average temperature profile for black liquor falling film with varying dry solids content.

4.4.4.1 Temperature Profile

The previous section investigated the effects of dry solids content on the hydrodynamics of black liquor films. This simulation series includes heat transfer into the simulation to look at how this effects the temperature rise in the film. Details of the simulation parameters are given in Table 4.3.

Table 4.3: Simulation series to study the effect of dry solids content on black liquor film surface evaporation.

Case	T_{in} [K]	T_{wall} [K]	$\dot{m}_{2\text{D}}$ [kg/s m]	χ_S	Re	f [Hz]	h_N [m]
1	343.0	353.0	1.0	0.55	20	30	0.0024
2	343.0	353.0	1.0	0.6	6	30	0.0042
3	343.0	353.0	1.0	0.7	0.1	30	0.0116
4	343.0	353.0	1.0	0.75	0.05	30	0.0185

Figure 4.23 shows the crosswise average temperature in the film. This value is calculated the same way as in Section 4.4.1. As can be seen in the figure, the dry solids

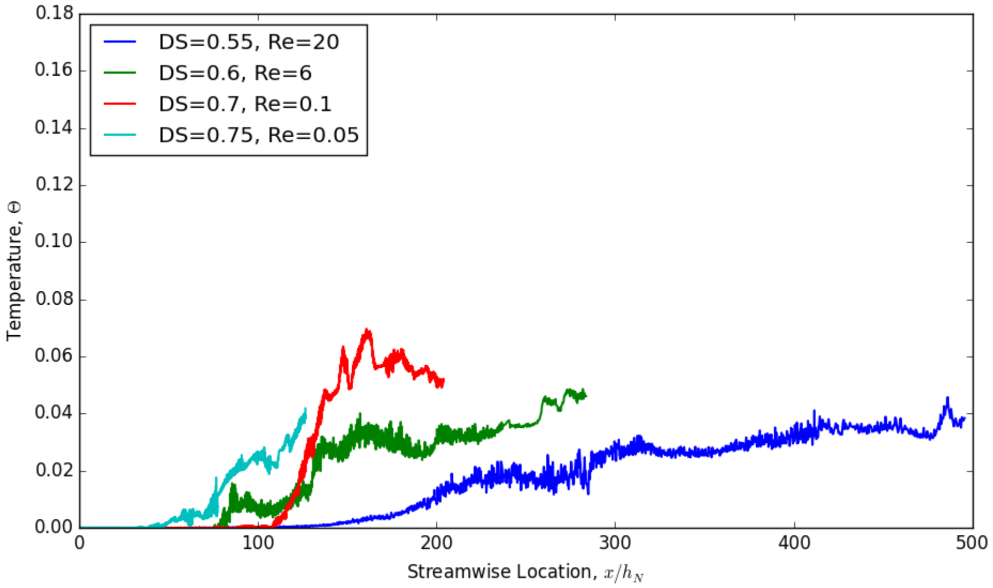

Figure 4.24: Surface temperature along the streamwise location for black liquor falling film with varying dry solids content.

have a slight affect on the average temperature. Roughly, as the dry solids content increases, the average temperature in the domain has a faster rate of increase. Because the inlet mass flux remains constant in the these simulations, as the Reynolds number increases inversely with the dry solids content. This relationship of increasing in the average liquid temperature with a decreasing Reynolds number fits what was shown in Section 4.4.1. The dry solids content will have an effect on the hydrodynamics of the flow, but the average film temperature is dominated by the hot region of liquid near the wall.

Figure 4.24 shows the surface temperature of the black liquor film for increasing dry solids content. From the results there seems to be a slight relationship showing that the higher the dry solids the earlier the in domain the surface temperature begins to increase appreciably. The surface temperature growth rate also seems to be higher with higher dry solids content.

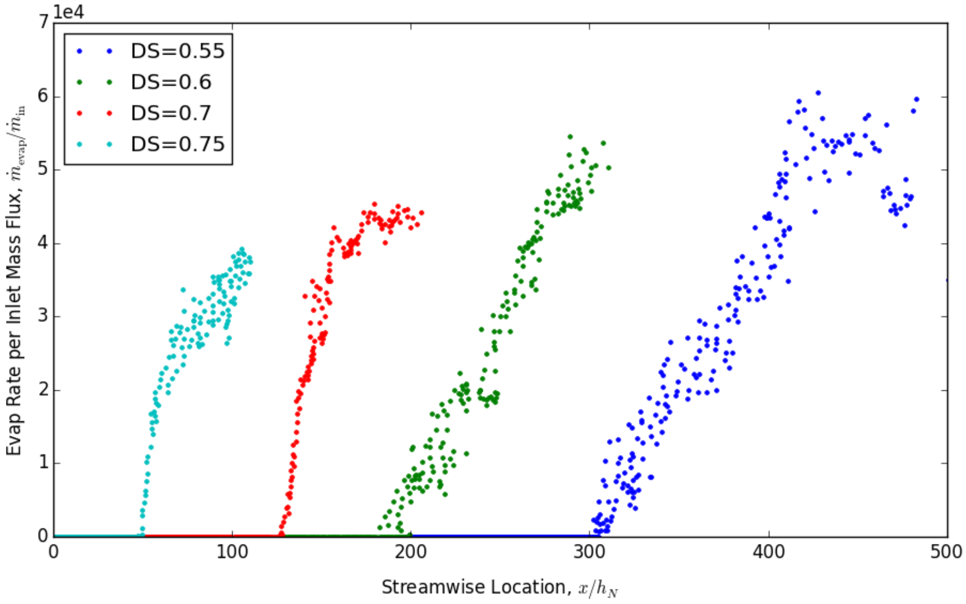

Figure 4.25: Average evaporation rate for black liquor falling film for varying dry solids content.

4.4.4.2 Evaporation Rate

This series of simulations will model a falling film of black liquor flowing down a vertical heated surface. The flow is modeled on a highly resolved grid using the non-Newtonian viscosity model for high dry solids content. It is known that the flow characteristics play an important role in facilitating heat transfer, so this simulation case will be run over a range of dry solids content to measure the effect non-Newtonian rheology. Details of the simulation parameters are given in Table 4.4.

Table 4.4: Parameters for cases investigating the effect of non-Newtonian viscosity on heat transfer to a falling film.

Case	T_{sat} [K]	T_{wall} [K]	$\dot{m}_{2\mathrm{D}}$ [kg/s m]	χ_S	f [Hz]	h_N [m]
1	373.0	376.0	1.0	0.55	30	0.0024
2	373.0	376.0	1.0	0.6	30	0.0042
3	373.0	376.0	1.0	0.7	30	0.0116
4	373.0	376.0	1.0	0.75	30	0.0185

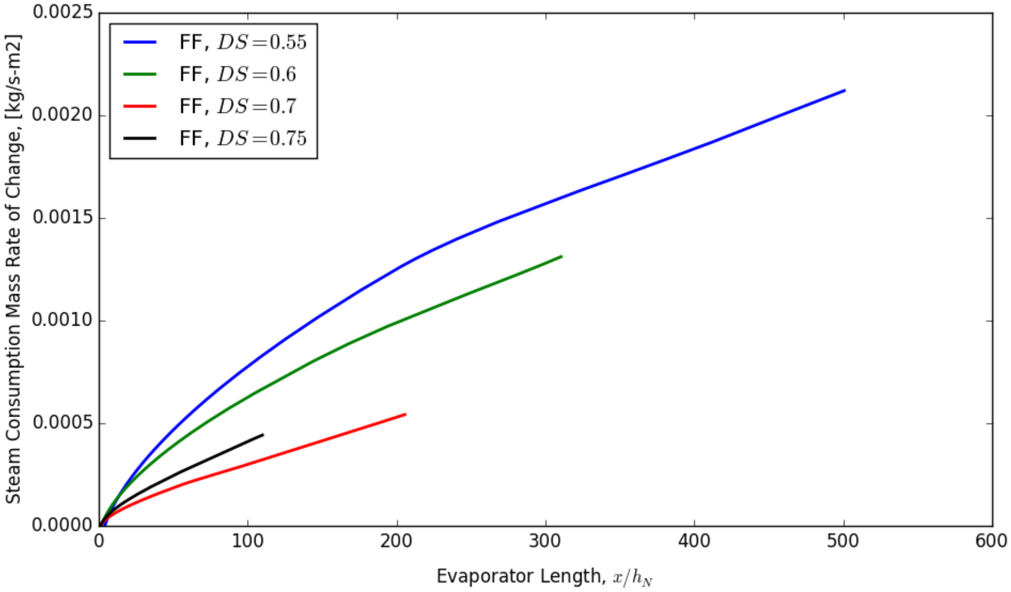

Figure 4.26: Global steam consumption rates for evaporator lengths of increasing size for a black liquor falling film.

Figure 4.25 shows the rate of evaporation from the black liquor film along the streamwise direction. There is a similar relationship here as with Figure 4.9. There is an inlet region with no evaporation while the heat is propagating through thickness of the film, followed by a region of increasing evaporation rate. Films with a lower dry solids content have a higher evaporation rate. These simulations use a fixed mass flow rate, as a result the density increases with the dry solids content the Reynolds number decreases. Because of this relation, the lower dry solids content flows will have better convective heat transfer from wall. Also, the Nusselt film thickness is greater for the higher dry solids flows, this means that the heat has to pass through a larger distance before it can raise the surface temperature.

Figures 4.26, 4.27, and 4.28 show the steam consumption rates, global mass evaporation rates, and steam efficiency for evaporator lengths. From Figure 4.26 is can be seen that using the normalized evaporator length, the curves for the steam consumption rates have a similar shape to those for the Newtonian falling film. From the curves it appear the general trend is from increasing dry solids content to lead to an

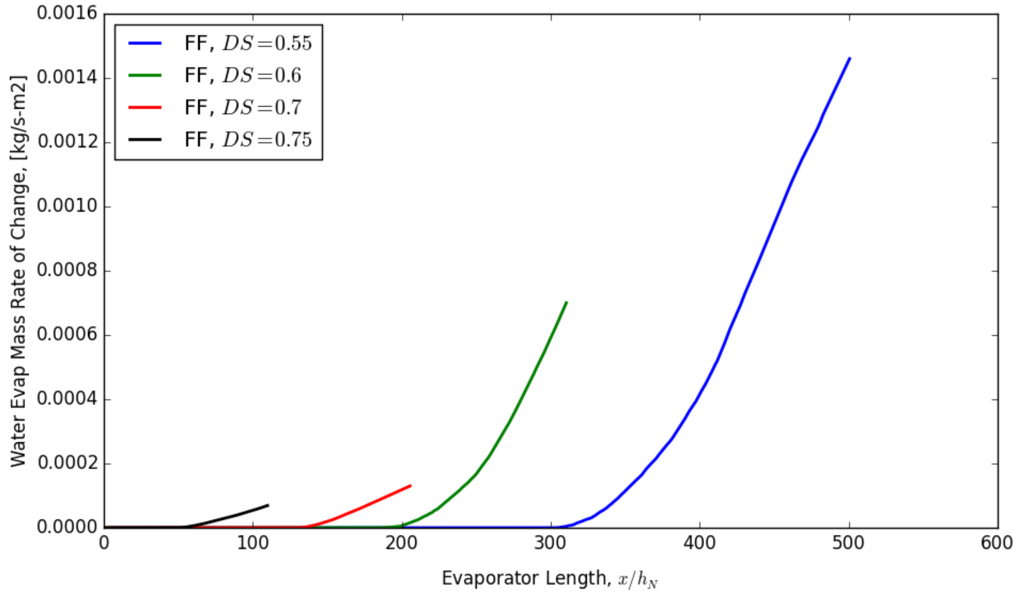

Figure 4.27: Global liquid mass evaporation rates for evaporator lengths of increasing size for a black liquor falling film.

overall decrease in the steam consumption rate. This pattern is reversed for the the simulations 70 % and 75 % dry solids, however their values are close. The decrease in the domain lengths for higher dry solids content is due to the Nusselt film thickness being higher for higher dry solids simulations, and the Nusselt film thickness is used to scale the domain.

Figure 4.27 shows the relationships for global mass evaporation with the evaporator lengths. Clearly increasing the evaporator length leads to a higher global evaporation rate because the effect of the entrance length, where little or no evaporation is occurring, is reduced. For high dry solids simulations, the initial evaporation location is moved closer to the inlet.

Figure 4.28 shows the steam efficiency for these black liquor falling film simulations. The results suggest that, for a given normalized domain length, a higher steam efficiency is found is evaporators with a higher dry solids content.

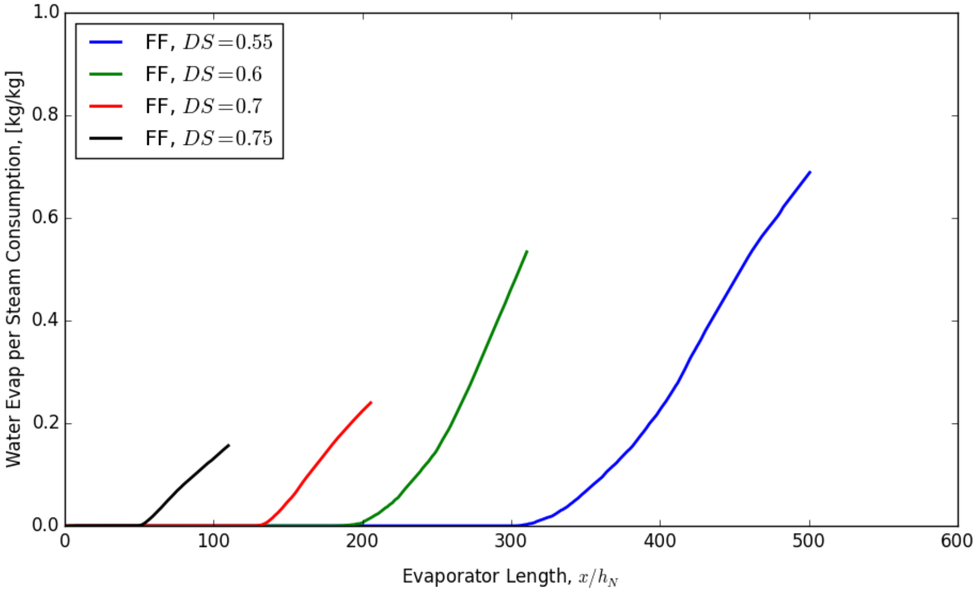

Figure 4.28: Steam efficiency for evaporator lengths of increasing size for a black liquor falling film.

CHAPTER 5

LIQUID CURTAIN EVAPORATION

5.1 Background

A liquid curtain is a thin liquid sheet formed by expelling the fluid through a slot and allowing it to fall under the force of gravity. A diagram of a liquid curtain is shown in Figure 1.3. The first studies of liquid curtains were conducted by Brown who was motivated by studying curtain coating industrial processes [16]. Brown produced a relationship for the average film velocity of a liquid curtain based on the velocity of a particle falling freely under the force of gravity. This relationship was later refined by Aidun to increase accuracy near the curtain entrance [17]. Taylor developed a non-linear differential equation describing the streamwise velocity of the film,

$$\frac{d}{dx}\left(\frac{1}{U}\frac{dU}{dX}\right)+\frac{1}{U}-\frac{dU}{dX}=0\,. \tag{5.1}$$

The normalized values for velocity and distance are $U=(\frac{\rho}{4\eta g})^{1/3}u$, and $X=(\frac{\rho}{4\eta})^{2/3}g^{1/3}x$, respectively [16]. This equation is used in conjunction with the assumption of a constant stress in the crosswise component and the surface tension effects are negligible. Liquid curtains are also used in atomization by bombarding the sheet from both sides with high speed impinging air, so called airblast atomization.

A liquid curtain is not the only form of a liquid sheet. Several methods of creating a liquid sheet have been investigated in the literature. Researchers have investigated the characteristics of liquid sheets with different aspect ratios. A liquid curtain is at one extreme, a large aspect ratio flow, created by extruding liquid through a long, thin slot [24]. Sheets with small length-to-thickness aspect ratios are created by driving liquid from a flat-spray nozzle. This type of flow is called a liquid fan and is characterized by thick rims at the edges [22]. A liquid jet impinging on a plate was the method used by Taylor in his popular study of water bells [1]. And another type of liquid sheet is the radially expanding sheet created by two impinging jets [19, 21].

Early linear stability analysis of falling liquid sheets neglected the viscosity of the liquid and the surrounding gas. These assumptions lead to the conclusion that the liquid sheet is inherently stable if $We < 1$ [5]. However this conclusion is in opposition to early experimental observations by Brown that showed that when $We < 1$ break down of the sheet could occur due to disturbances that propagate upstream. To account for this discrepancy, later linear stability analysis took into account the viscosity of the liquid and then the viscosity of the liquid and the gas [6, 8].

Heat transfer to a falling liquid curtain has been studied previously by McCarthy and Merson, who investigated heat transfer from steam surrounding a falling liquid curtain of water [11]. They developed an analytical model for the temperature profile and provided experimental results. The calculated average crosswise temperature matched with mixed cup temperature values measured along the streamwise direction. However, this model was created for an intact liquid sheets and is not valid for liquid curtains past the initial breakup. Beyond these authors, there have been no other investigations of heated falling liquid curtains.

This chapter focuses on the analysis of 2D liquid curtain flows of Newtonian and black liquor based on the numerical solution of the transient Navier-Stokes equations. The conservation laws for the transport of heat and species are accomplished with source terms describing interfacial evaporation and species enrichment. This study investigates the fundamental structure of black liquor liquid curtain at high dry solid mass fraction and its affect on the evaporation.

5.2 Mathematical Model

A depiction of the falling liquid curtain domain is shown in Figure 4.1. The thin film enters the top of the with a domain with a prescribed uniform velocity profile.

The film is pulled by gravity down to the bottom of the domain. The steam that surrounds the liquid curtain on both sides also enters the domain with a uniform velocity profile. The steam has a density and viscosity much smaller than the liquid.

The two fluids, the liquid film and steam, are simulated as a single-fluid field. The special parameter α is used to indicate the portion of the cell containing the liquid, and the remaining volume of the cell contains the steam. The fluid properties of the single-fluid field are calculated from the interpolation of component fluid properties. For example, $\phi = \alpha\phi_l + (1-\alpha)\phi_v$. From the single-field formulation, the respective equations for fluid phase, continuity, momentum, and energy of the two-phase flow fields are expressed as:

$$\frac{\partial \alpha}{\partial t} + \nabla \cdot (\vec{v}\alpha) + \nabla \cdot (\vec{v}_r \alpha(1-\alpha)) = -\dot{S}_v \tag{5.2}$$

$$\frac{\partial \rho}{\partial t} + \nabla \cdot \rho\vec{v} = 0 \tag{5.3}$$

$$\frac{\partial \rho\vec{v}}{\partial t} + \nabla \cdot \rho\vec{v}\vec{v} = -\nabla p + \nabla \cdot \vec{\tau} + \rho\vec{g} + \vec{F}_{CSF} \tag{5.4}$$

$$\frac{\partial \rho c_p T}{\partial t} + \nabla \cdot (\rho\vec{v}c_p T) = \nabla \cdot k\nabla T - \dot{S}_q\,. \tag{5.5}$$

For simulations in this chapter that use black liquor as the film liquid, the dry-solids content is treated as a scalar that is convected with the flow. The species conservation equation is

$$\frac{\partial \chi_S}{\partial t} + \nabla \cdot \rho\vec{v}\chi_S = \nabla \cdot \rho\xi\nabla\chi_S + \dot{S}_m\,. \tag{5.6}$$

The physical presence of salt crystals that form in the liquid film due to crystallization is not explicitly captured in this formulation.

5.2.1 Important Parameters

Reynolds Number

There are several parameters that are important for a discussion of a falling liquid curtain. The Reynolds number compares the magnitude of the inertial forces present

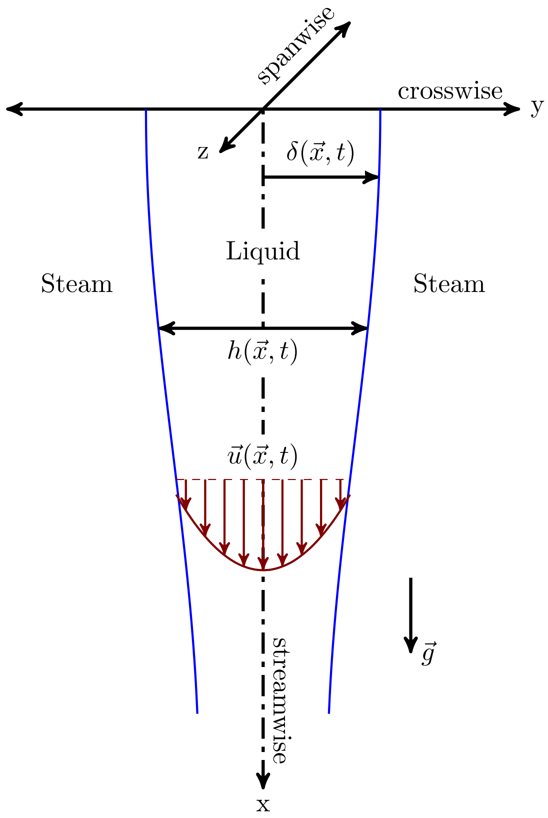

Figure 5.1: Diagram of liquid curtain.

in the film to the viscous forces. For this flow arrangement it is calculated as

$$Re = \frac{\rho_l u_{l,\text{inlet}} h_{l,\text{inlet}}}{\mu_l}\,. \tag{5.7}$$

Where $u_{l,\text{inlet}}$ and $h_{l,\text{inlet}}$ are the domain inlet velocity and thickness of the liquid curtain respectively. And ρ_l and μ_l represent the density and kinematic viscosity of the liquid curtain.

Weber Number

The Weber number is used to assess surface deformability due to the flow. It relates the viscous normal stress at the film surface to the surface tension:

$$We = \frac{\rho_l u_{l,\text{inlet}}^2 h_{l,\text{inlet}}}{\sigma}\,. \tag{5.8}$$

In this equation, σ represents the surface tension. For small values of the Weber number, the fluid flow is driven by surface tension, while for falling films with large Weber numbers gravity dominates. Small values of Weber number mean that the viscous forces due to the flow are not strong enough to generate pressure that can deform the film surface.

Velocity Ratio

The velocity ratio is a measure of the relative inlet velocity of the vapor compared to the liquid curtain:

$$V_r = \frac{u_{v,\text{inlet}}}{u_{l,\text{inlet}}}\,. \tag{5.9}$$

Froude Number

The Froude number compares the inertial forces of the film to the force of gravity. The parameter is calculated as

$$Fr = \frac{u_{l,\text{inlet}}^2}{gL}\,. \tag{5.10}$$

Where g is the magnitude of gravity and L represent the characteristic length of the film.

Peclet Number

The Peclet number expresses the relative power of convection and heat conduction

$$Pe = \frac{\rho_l c_{p,l} u_{l,\text{inlet}} h_{l,\text{inlet}}}{k_l} . \tag{5.11}$$

Where $c_{p,l}$ and k_l are the specific heat and thermal conductivity of the liquid curtain.

5.2.2 Boundary Conditions

The inlet thickness for the falling liquid curtain is chosen in correspondence with the inlet liquid velocity to generate a desired mass flow rate. At the inlet, the liquid curtain values are specified for the phase indicator, and temperature of the incoming fluid: $\alpha = 1$, $T = T_{l,\text{inlet}}$. If the fluid being modeled is black liquor, the dry solids content is specified as $\chi_S = \chi_{S,\text{inlet}}$. The inlet velocity is specified as a uniform value across the liquid inlet, $u = u_{l,\text{inlet}}$, $v = 0$.

To prevent numerical issues at the inlet of the domain a small gap separates the liquid inlet face from the stream inlet face. No mass transfer is permitted through the gap face on the inlet wall, it acts as a spacer. The steam inlet face is set to all the space above and below the liquid inlet face and two gap faces. The steam inlet values are set to $\alpha = 0$, $T = T_{g,\text{inlet}}$, $\chi_S = 0$, $u = u_{g,\text{inlet}}$, $v = 0$.

The outlet boundary conditions for the liquid curtain are the same as the outlet boundary conditions of the falling film. A zero gradient boundary is applied to all values: $\partial\alpha/\partial x = 0$, $\partial u/\partial x = 0$, $\partial v/\partial x = 0$, $\partial T/\partial x = 0$, and $\partial\chi_S/\partial x = 0$. In place of wall boundary conditions, the crosswise edges of the domain are periodic.

5.3 Numerical Validation

A series of simulations have been run in order to determine that the resolution of the mesh is not affecting the flow of the liquid curtain. The results of the simulations are shown in Figure 5.2. The breakup location is used as the key metric used to determine the effect of mesh resolution on the liquid curtain. With a fine enough resolution, the breakup location is no longer affected by the mesh. The resolution used here is $\Delta x = 0.03h_{\text{inlet}}$, $\Delta y = 0.03h_{\text{inlet}}$.

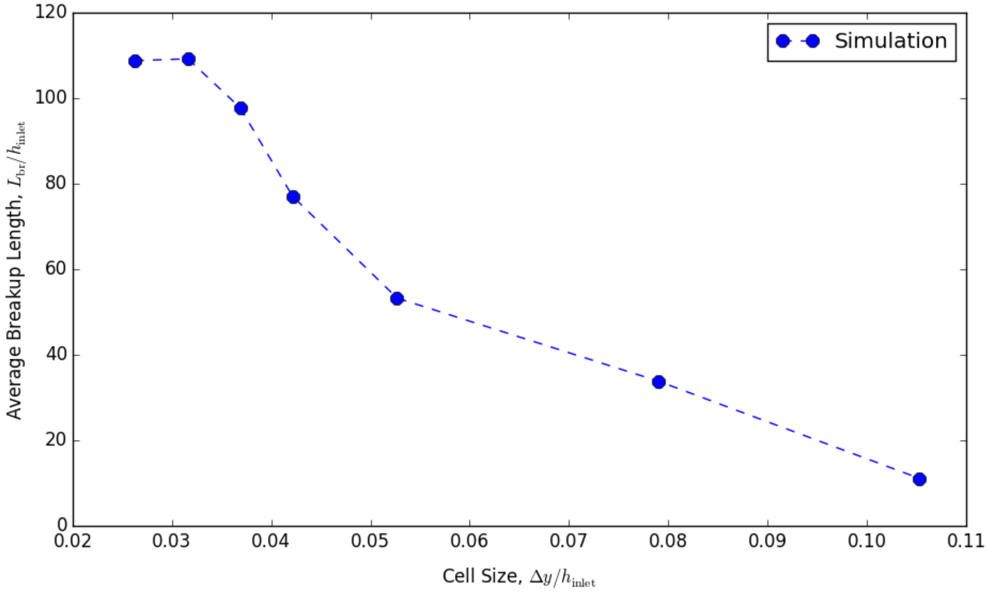

Figure 5.2: Liquid curtain breakup length as a function of the mesh cells crosswise length.

Images of the mesh for near the liquid curtain inlet and the breakup location are shown in Figures 5.3 and 5.4 respectively. In Figure 5.3 although only a small distance is shown, the narrowing of the liquid curtain can already be seen. Figure 5.4 shows the droplet that is forming at the end of the liquid curtain. An expanded view is shown in Figure 5.5, here it can be seen that a two segments of liquid have broken away from the bulk curtain. And these segments have thick regions of liquid that have formed on the tips.

5.3.1 Velocity Profile of Liquid Curtain

Early work with liquid curtains was done by Brown, who determined a relationship for the average velocity of a liquid curtain emanating from a slot [16]. The velocity and location are normalized by $U = (\frac{\rho}{4\eta g})^{1/3}u$, and $X = (\frac{\rho}{4\eta})^{2/3}g^{1/3}x$. The relationship

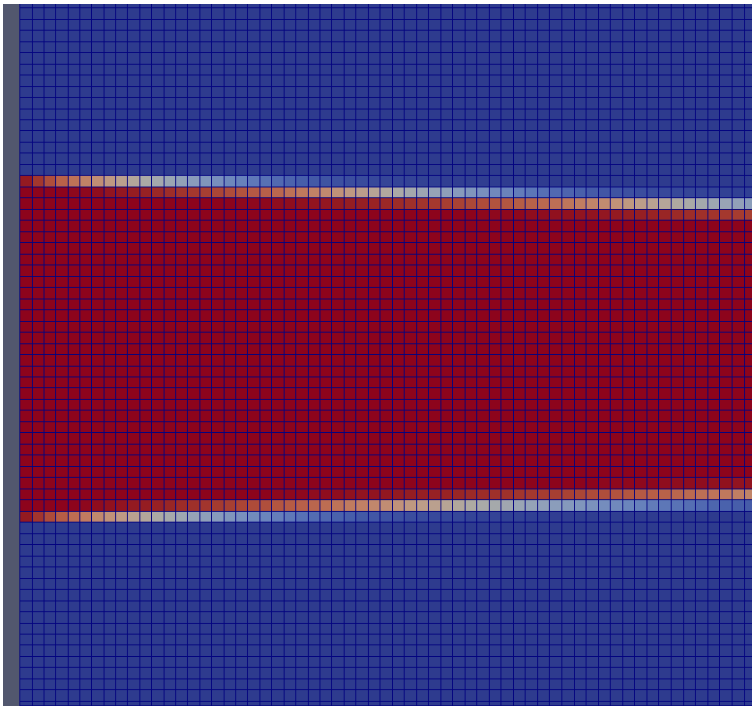

Figure 5.3: Mesh for liquid curtain simulation. Domain entrance shown. Gravity acts to the right.

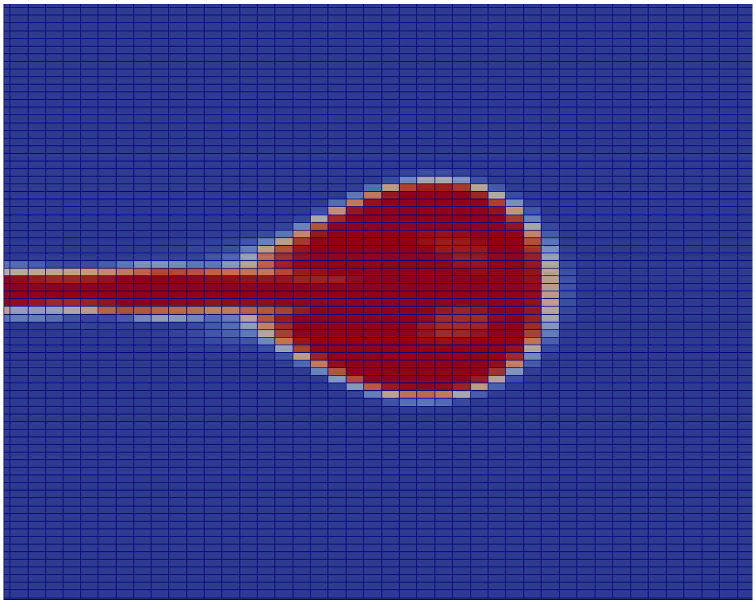

Figure 5.4: Mesh for liquid curtain simulation. Area shown is the breakup location of the curtain. Droplet is forming at the tip of the film and it will break away sometime later.

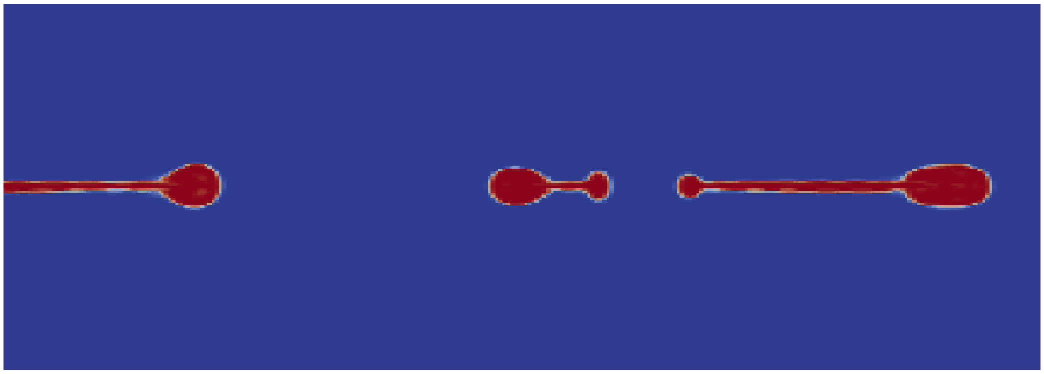

Figure 5.5: Liquid curtain with droplet forming at tip. Strand of liquid separated from curtain is capped on end with thick liquid regions.

that Brown found for the streamwise liquid velocity was

$$U^2 = U_0^2 + 2(X - 2)\,. \tag{5.12}$$

This free fall relationship is valid for $X > 7$. Before this location the model cannot account for the effect of surface curvature of the film. Aidun provided a model that is accurate up to $X = 3$ by using the equation of Taylor, Equation 5.1, neglecting surface tension and normalizing the pressure [17]. The equation reduces to

$$U'' = UU' - 1\,. \tag{5.13}$$

With boundary conditions extracted from the experimental results of Brown,

$$U(X = 12) = 4.6 \tag{5.14}$$

$$U' = 1/U \quad \text{at} \quad X = 12\,. \tag{5.15}$$

The solution is simplified by using the substitution $U^\star = 2^{-2/3}U$ and $X^\star = 2^{-1/3}(X + C)$. The solution to Equation 5.13 is

$$U^\star(X^\star) = -\frac{a_r A_i' + B_i'}{a_r A_i + B_i}\,. \tag{5.16}$$

The symbols A_i and B_i represent the Airy functions that are functions of $X^\star$. And the symbols A_i' and B_i' represent the first derivatives. The value a_r can is calculated from

$$a_r = -\frac{B_i' + U_b^\star B_i}{A_i' + U_b^\star A_i} \quad \text{at} \quad X = 12\,. \tag{5.17}$$

Where $U_b^\star = 2^{-2/3}U(X = 12)$. The relationship in Equation 5.16 provides a more accurate solution for the free fall velocity profile. Agreement with the experimental values occurs down to $X > 3$. Before this location the effect of the surface curvature is too great to be accounted for in the relationship.

Figure 5.6 shows a snapshot during a simulation of a falling film and a plot for the average velocity profile. The simulation matches the parameters used in Brown's experiment. No inlet velocity was given, and was instead described simply as "negligible", thus an inlet velocity was chosen that allowed the velocity profile to match the data. The velocity profile matches the experimental and analytical data until breakup occurs. After breakup, the velocity profile drops below the expected value.

The crosswise-average velocity in the streamwise direction is evaluated by considering the phase indictor, α, and streamwise velocity, v, at every x-location. Measurements are taken at N stations along the streamwise direction, and the crosswise direction contains M computational cells. The location of a station can be calculated as:

$$x_{\text{st}} = \sum_{i=1}^{N_{\text{st}}} \Delta x_i\,. \tag{5.18}$$

Where Δx_i is spacing between stations in the streamwise direction between the i and $i-1$ station. The crosswise mass average of the streamwise velocity is calculated from the following equation,

$$u_{\text{avg}}(x_{\text{st}}) = \frac{\left[\sum_{j=1}^{M} \alpha_j \rho_{l,j} \mathcal{V}_j u_j\right]_{\text{st}}}{\left[\sum_{j=1}^{M} \alpha_j \rho_{l,j} \mathcal{V}_j\right]_{\text{st}}}\,. \tag{5.19}$$

If the maximum value of all α along the crosswise direction is less than 0.01, the film is considered broken at that x-location. Finding the minimum streamwise location

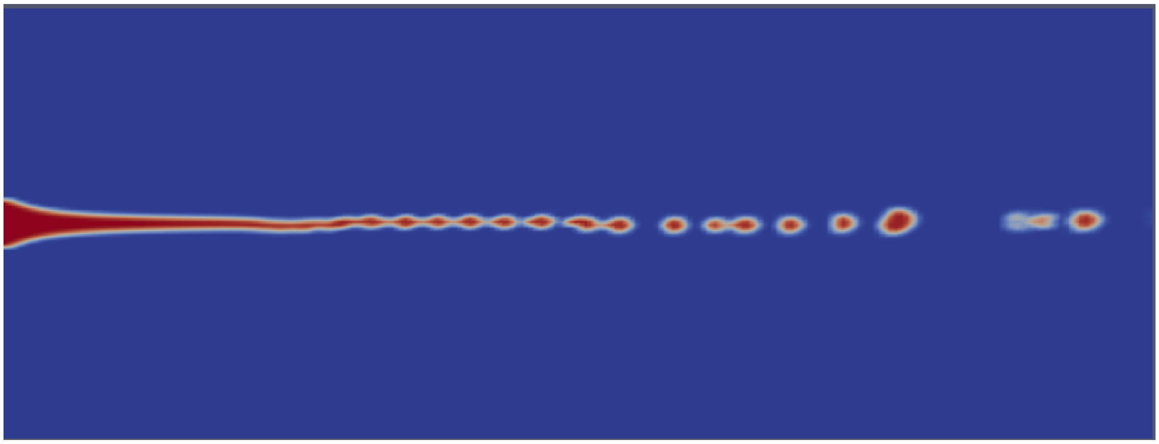

(a) VOF indicator field.

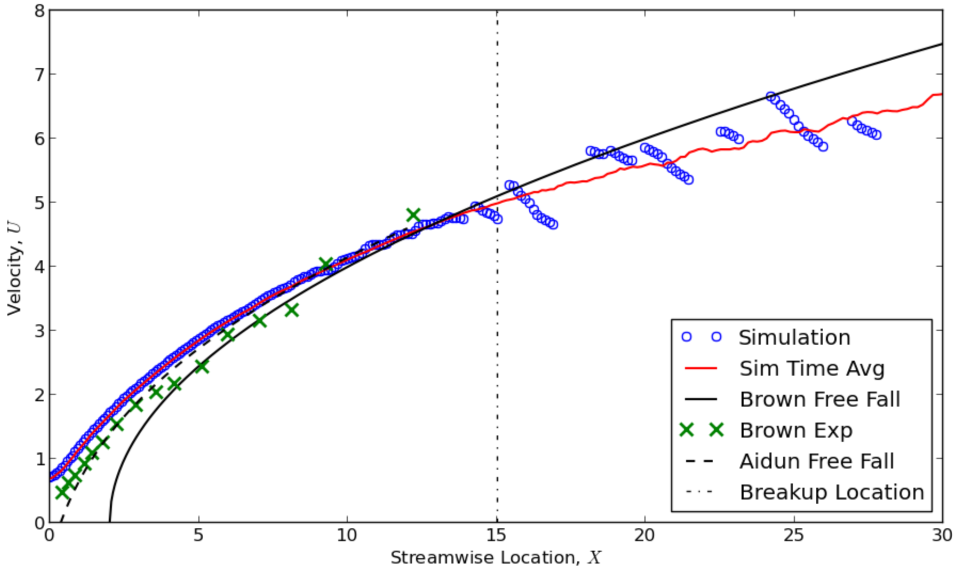

(b) Plot of crosswise average velocity compared to experimental from and analytical velocity profiles.

Figure 5.6: Two-dimensional simulation of Newtonian fluid falling from a slot with negligible inlet velocity. Dashed line indicates time-average breakup location.

the meets this criteria is considered to be the breakup location.

$$x_{br} = \{x_{st} \mid max\,(\alpha(x = x_{st}, y)) < 0.01\} \tag{5.20}$$

$$L_{br} = min(x_{br}) \tag{5.21}$$

This breakup location at a single time step is then average with the breakup location at all other time steps.

5.3.2 Heated Liquid Curtain Thermal Profile

An analytical solution for the temperature profile in a heated liquid curtain is given by McCarthy and Merson [11]. This analysis assumes that the liquid is a Newtonian fluid with constant physical properties, the flow is laminar and has reached steady state, and the heat transfer from steam encounters negligible resistance.

$$\rho c_p u(x) \frac{\partial T}{\partial x} = k \frac{\partial^2 T}{\partial y^2} \tag{5.22}$$

$$T = T_{\text{inlet}} \quad \text{at } x = 0 \tag{5.23}$$

$$\partial T/\partial y = 0 \qquad \text{at } y = 0 \tag{5.24}$$

$$T = T_{\text{steam}} \text{ at } y = \delta(x) \tag{5.25}$$

The relevant parameters for the heated liquid curtain are normalized as the following:

$$\Theta = (T - T_{\text{inlet}})/(T_{\text{steam}} - T_{\text{inlet}}) \tag{5.26}$$

$$\hat{X} = x/L \tag{5.27}$$

$$\hat{Y} = y/\delta(x)\,. \tag{5.28}$$

The value L is chosen as a location far enough downstream that the liquid temperature is 99 % of the steam temperature. Using the velocity profile of the liquid curtain and including the dimensionless variable $\Psi = 1 + 2\hat{X}/Fr$, the film half thickness can be described as,

$$\delta(x) = h_0 \Psi^{-1/2}\,. \tag{5.29}$$

The 2D energy equation solved to model the liquid curtain temperature is

$$\frac{Pe}{Fr}\frac{h_0}{L}\hat{Y}\Psi^{-3/2}\frac{\partial\Theta}{\partial\hat{Y}} + Pe\frac{h_0}{L}\Psi^{-1/2}\frac{\partial\Theta}{\partial\hat{X}} = \frac{\partial^2\Theta}{\partial\hat{Y}^2}\ . \tag{5.30}$$

The curtain enters the domain with an inlet temperature of $\Theta = 0$, and at some distance far enough downstream it will reach the stream temperature and will stop increasing. At the center line, $\hat{Y} = 0$ the temperature profile is symmetric. And at the interface between the liquid and steam, $\hat{Y} = 1$, the temperature equal to the steam temperature $\Theta = 1$. The conditions are represented by the following boundary conditions which are solved in conjunction with Equation 5.30:

$$\Theta = 0 \text{ at } \hat{X} = 0 \tag{5.31}$$

$$\partial\Theta/\partial\hat{X} = 0 \text{ at } \hat{X} = 1 \tag{5.32}$$

$$\partial\Theta/\partial\hat{Y} = 0 \text{ at } \hat{Y} = 0 \tag{5.33}$$

$$\Theta = 1 \text{ at } \hat{Y} = 1\ . \tag{5.34}$$

Figure 5.7 shows a colormap solution to Equations 5.30, and 5.34. This example is solved for the following parameters: $Pe = 1170$, $Fr = 0.052$, $h_0/L = 0.001667$.

Image snapshots from the simulation of the phase indicator and temperature profile are shown in Figure 5.8. This simulation uses the same fluid properties and boundary conditions as the analytical solution of Figure 5.7.

Figure 5.9 shows the results from a simulation conducted using the same flow parameters as Figure 5.7. Here, the black line indicates the analytical solution. This is value calculated by taking the crosswise averages of the temperature of the solution in Figure 5.7. The green crosses represent experimental values from work of McCarthy and Merson [11]. The red line represents the time-averaged crosswise temperature from the numerical simulation, with the blue circles being a snapshot. The liquid curtain breaks up around $x/L = 0.28$. It is shown that the crosswise average temperature along the streamwise direction has good agreement to the experimental results.

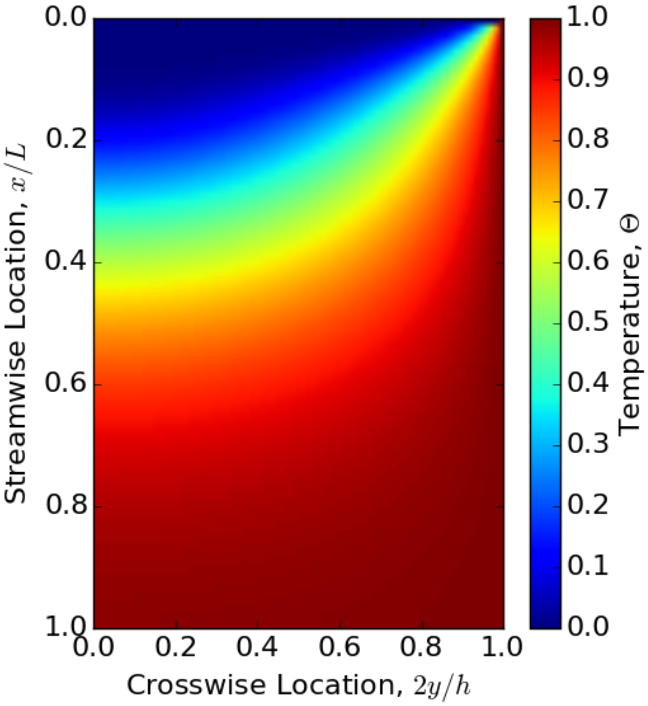

Figure 5.7: Analytical temperature model from Equations 5.30–5.34.

5.4 Analysis of Simulation Results

5.4.1 Curtain Breakup

The breakup location of a liquid curtain is an important transition. The hydrodynamics and transport mechanics of the flow will greatly change after the film disperses into droplets. A simulation series is conducted in order to investigate the effect of the Weber number and the velocity of the surrounding gas on the breakup process. This simulation series studies the case of Newtonian fluid falling under the effect of gravity while surrounded by an envelope of steam at the same temperature. No heat transfer is occurring. The aim of this scenario is to study the breakup mechanics and surface waves that form on the liquid sheet. Cases cover a range of liquid-gas velocity ratios, V_r, relating the liquid inlet velocity to the steam inlet velocity, and a range of inlet Weber numbers. The specifics of this simulation series are outlined in Table 5.1.

The breakup location at a particular instance is determined by considering the

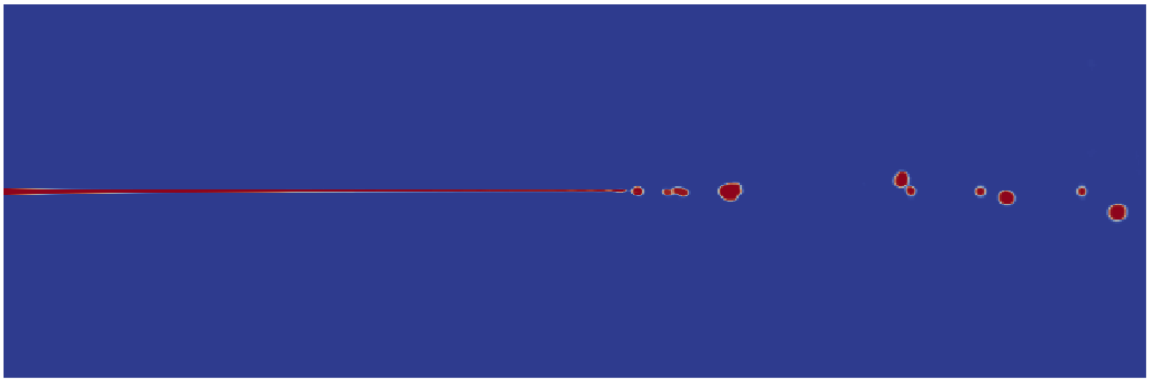

(a) VOF indicator field

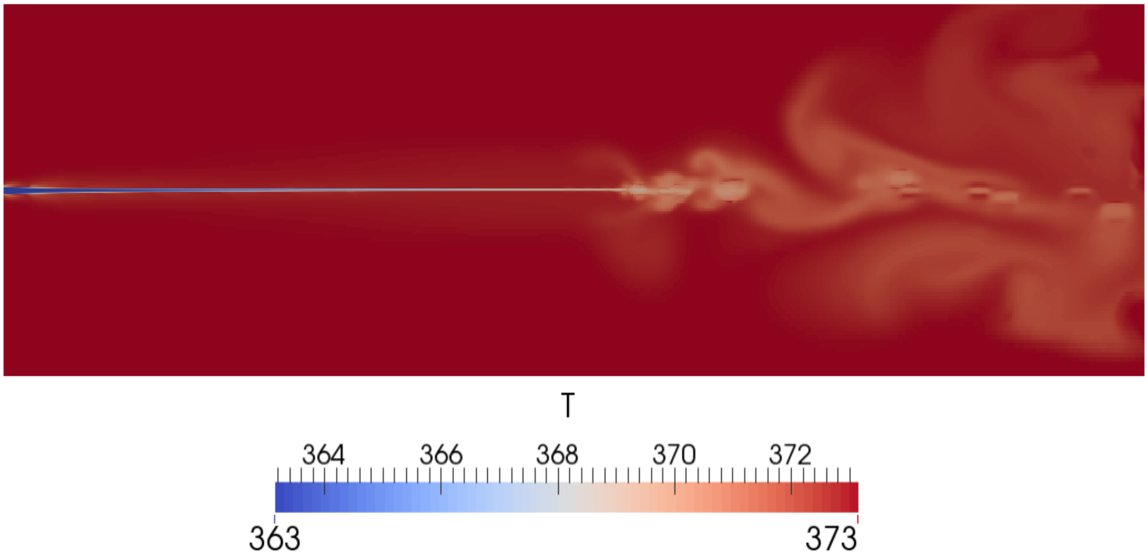

(b) Temperature field, K

Figure 5.8: Images of simulated heated liquid curtain. Dashed line indicates time-average breakup location.

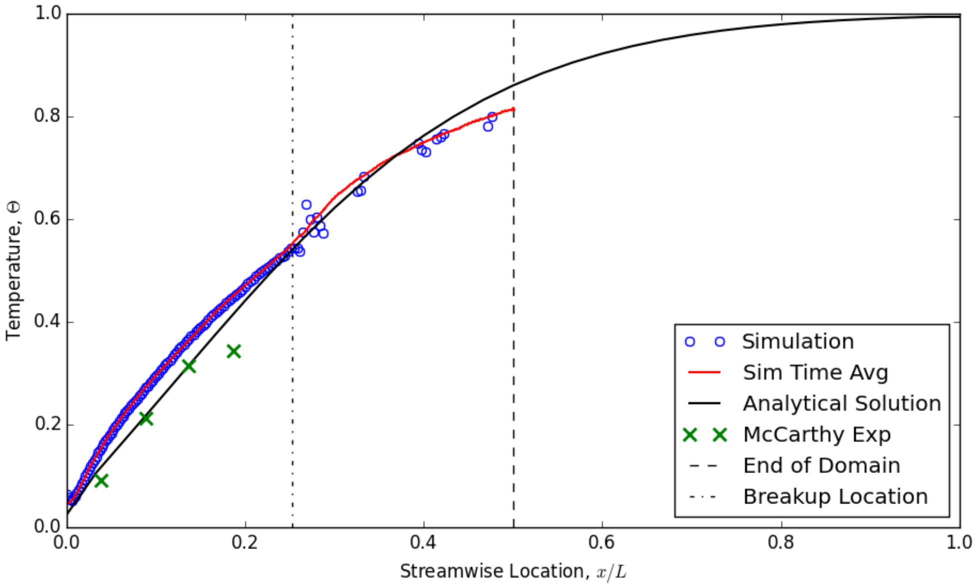

Figure 5.9: Simulation of heated liquid curtain. Dashed line indicates time-average breakup location.

phase indictor α at every x-location. If the maximum value of all α along the crosswise direction is less than 0.01 , the film is broken at that x-location. Finding the minimum streamwise location the meets this criteria is considered to be the breakup location,

$$x_{br} = \{x_{st} \mid max\,(\,\alpha(x = x_{st}, y)\,) < 0.01\} \tag{5.35}$$

$$L_{br} = min(x_{br})\,. \tag{5.36}$$

This breakup location at a single time step is then averaged with the breakup location at all other time steps. It is this time-averaged value for the breakup location that is recorded in Figure 5.10.

Results of the simulations of Table 5.1 can be seen in Figure 5.10. As shown in the figure, as the Weber number decreases the breakup length also decreases. The Weber number, as defined in Equation 5.8, can be related to the stability of the liquid curtain, so a decrease in the breakup length with a decrease in Weber number is expected. This conforms to expectations because the Weber number in these flows acts a measure of stability. Also, at high Weber number, as the velocity ratio increases

Table 5.1: Simulations designed to study effect of inlet velocity and gas/liquid velocity ratio on liquid curtain hydrodynamics.

Case	We	V_r	Fr	Re	$V_{\text{liq,inlet}}$ [m/s]	h_{inlet} [m]
1	5.0	0.5	20	709.8	0.425	0.000924
2	5.0	1.0	20	709.8	0.425	0.000924
3	5.0	1.5	20	709.8	0.425	0.000924
4	1.5	0.5	20	287.7	0.315	0.000560
5	1.5	1.0	20	287.7	0.315	0.000560
6	1.5	1.5	20	287.7	0.315	0.000560
7	1.0	0.5	20	212.3	0.284	0.000413
8	1.0	1.0	20	212.3	0.284	0.000413
9	1.0	1.5	20	212.3	0.284	0.000413

the stability of the liquid curtain decreases.

Figure 5.11 shows the crosswise-average velocity along the streamwise direction. The red line indicates the time average of the velocity, and the blue circles show a snapshot of the flow. From this figure it can be seen that the breakup process has the effect of delaying the free fall velocity. Breakup of the liquid curtain occurs around $X = 78\,000$ At this location there a region where the velocity slows due to energy lost during the breakup process. After this breakup region, the velocity begins to increase and by the end of the domain the shape of the velocity profiles matches the projected shape had breakup not occurred. In this simulation, the breakup process had the effect of delaying the free velocity by, $60\,000$ length units, X.

5.4.2 Heat Transfer from Surrounding Gas

The previous section looked at the general hydrodynamics of a liquid curtain. This section will investigate the heat transfer from the steam to the liquid curtain. This simulation series studies Newtonian falling liquid curtain surrounded by an envelope of steam at an elevated temperature. The goal of this simulation is to see the affect

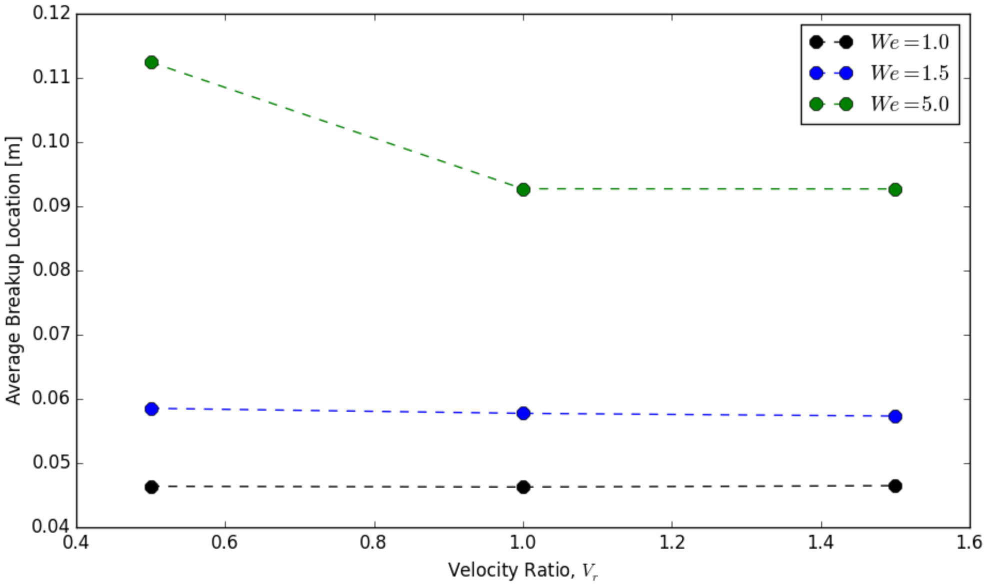

Figure 5.10: Average breakup location of isothermal liquid curtain with respect to velocity ratio for various Weber numbers.

heat transfer has on the breakup mechanism of the liquid curtain. A range of liquid-gas relative velocities is used, as shown in Table 5.2.

Table 5.2: Cases intended to study heat transfer from steam to falling liquid curtain. Liquid inlet temperature: 372.5 K, density: $994.0\,\mathrm{kg/m^3}$, dynamic viscosity: 0.000 719 kg/m s, surf tension: 0.0589 N/s. The inlet thickness is 0.000 89 m.

Case	We	V_r	T_{sat} [K]	$T_{\mathrm{stm,inlet}}$ [K]	$V_{\mathrm{liq,inlet}}$ [m/s]	$\dot{m}_{\mathrm{2D}}$ [kg/s m]	Re
1	1.5	0.5	373.0	383.0	0.390	0.34	479
2	1.5	1.0	373.0	383.0	0.390	0.34	479
3	1.5	1.5	373.0	383.0	0.390	0.34	479

Evaporation rates along the streamwise direction from the simulations are shown in Figure 5.12. For the liquid curtain there is an inlet region where little or no evaporation occurs. The dotted lines in the figure represent the breakup location of the curtain. Peak evaporation rate occurs in the region just after the breakup location. Moving downstream, the evaporation rate slowly increases as the droplets formed after breakup move downstream.

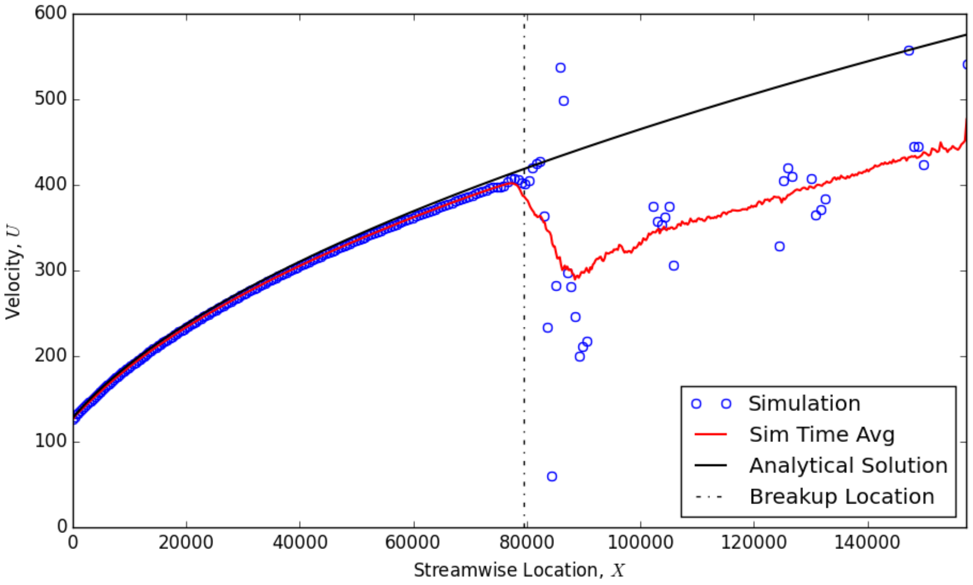

Figure 5.11: Mean streamwise velocity of liquid curtain. Simulation compared to free fall analytical solution of Brown.

Figure 5.13 shows a snapshot of the interface. Solid red dots on the image show locations where evaporation is occurring. It can be seen from the image that evaporation occurs sporadically in the liquid curtain before breakup. After the breakup, the droplets that form have a higher percentage of their interface undergoing evaporation. Near the exit of the domain, evaporation is occurring around the entire surface of the droplet.

Figures 5.14, 5.15, and 5.16 show the global mass evaporation rates, steam consumption rates, and steam efficiency for evaporator lengths. These are not values measured at a specific streamwise location, but global values that are calculated cumulatively along the streamwise distance of the simulation domain.

The measured global steam consumption rates as a function of evaporator length for the various liquid-gas relative velocities is shown in Figure 5.14. The plot shows that increasing the relative velocity of gas to liquid decrease the rate of steam consumed in the liquid curtain evaporator.

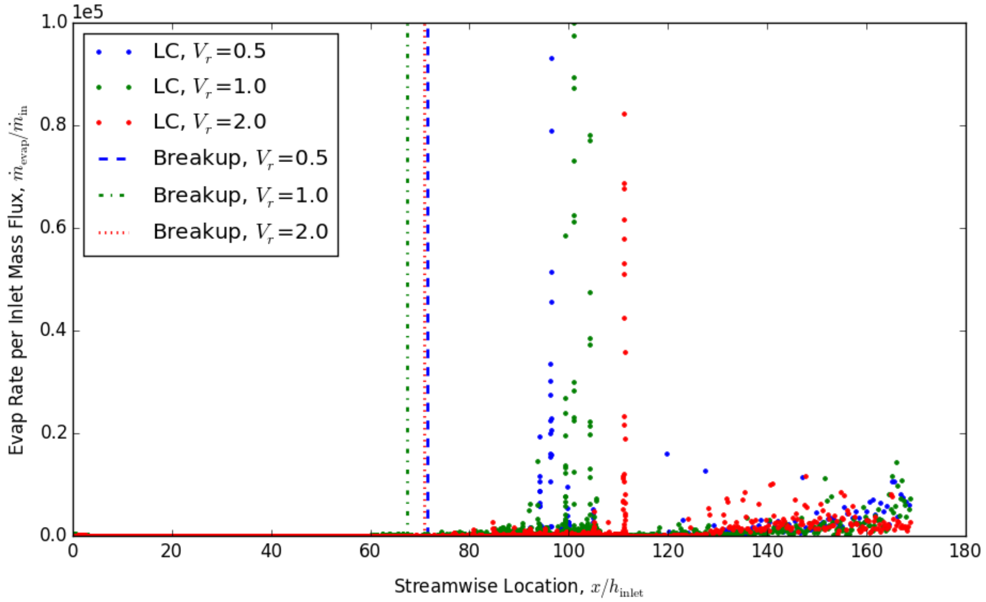

Figure 5.12: Evaporation rates at streamwise locations for various velocity ratios. Dotted lines indicate the average breakup location.

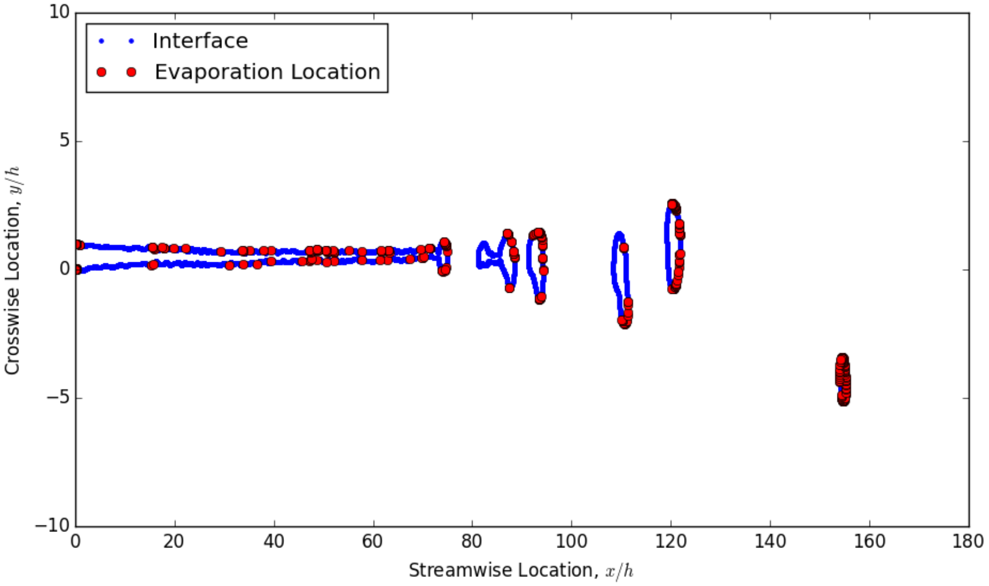

Figure 5.13: Snapshot of simulation that shows the interface and the location on the interface where evaporation occurs.

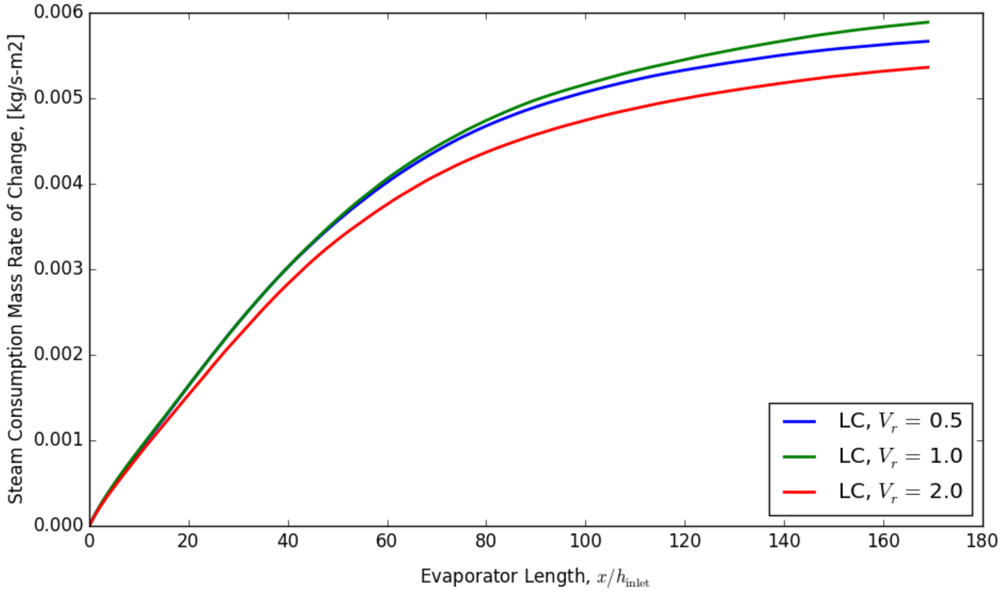

Figure 5.14: Global steam consumption rates for evaporator lengths of increasing size for a Newtonian liquid curtain.

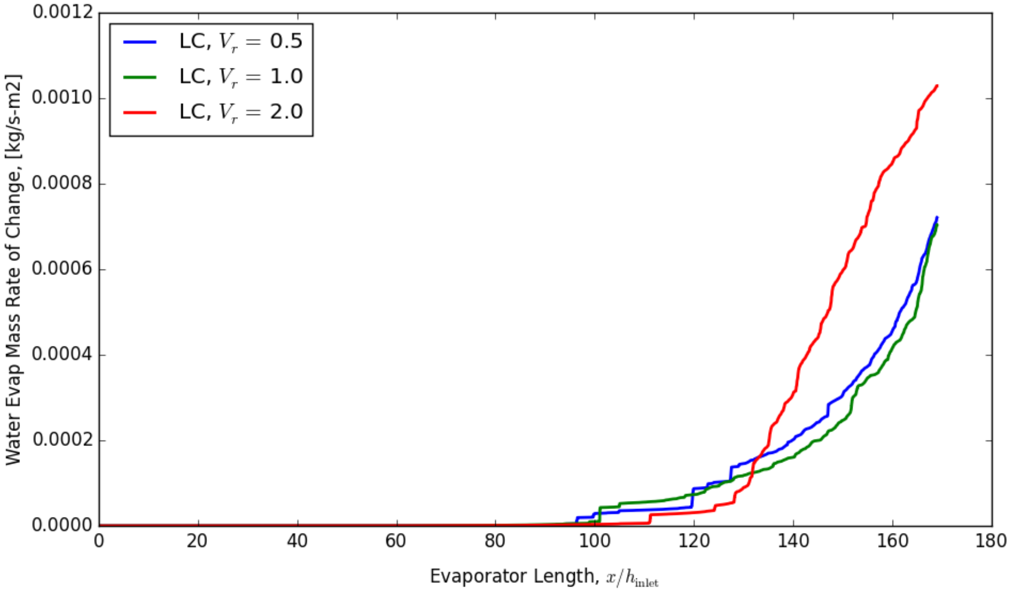

Figure 5.15: Global liquid mass evaporation rates for evaporator lengths of increasing size for a Newtonian liquid curtain.

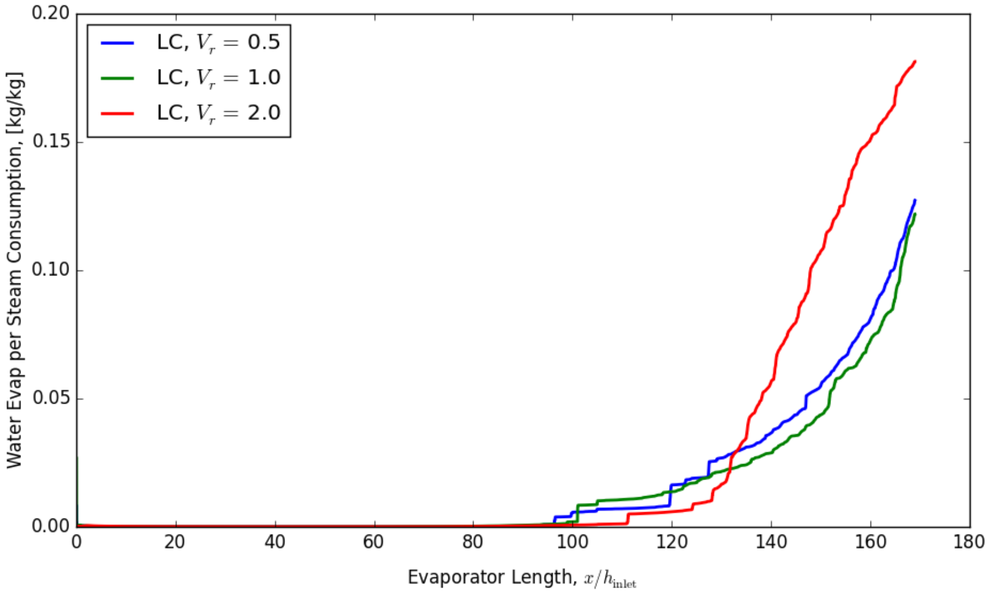

Figure 5.16: Steam efficiency for evaporator lengths of increasing size for a Newtonian liquid curtain.

Figure 5.15 shows the relationship for global liquid evaporation rates with evaporator length for varying velocity ratios. The shape of these curves are similar to the global liquid evaporation rates for a Newtonian falling film, Figure 4.14. The velocity ratio only has a small effect on the evaporation rate, with a high gas velocity leading to high evaporation rate at long evaporator lengths. The velocity ratio had a small effect on moving the start of evaporation location. Although the start of evaporation is pushed further down the domain for the simulation of $V_r = 2.0$, as the domain length increases the global evaporator overtakes for this overtakes the values for simulations with a lower velocity ratio.

Figure 5.16 shows global steam efficiency for these cases of a Newtonian liquid curtain. Because the steam consumption rate grows rapidly early in the domain and then begins to levels off, the mass evaporation rate curve has the dominate affect of on shaping the curve for the evaporator steam efficiency. From this plot, it can be seen that increasing the velocity ratio increases the steam efficiency for long evaporator domains.

5.4.3 Black Liquor Liquid Curtain

The computational model has been used to investigating the nature of the transport mechanics for a heated liquid curtain. The following sections will utilize the model to study the effects of non-Newtonian properties of black liquor.

5.4.3.1 Effect of Dry Solids

In this simulation series a thin sheet of black liquor falling under the effect of gravity is modeled on a highly resolved grid using the non-Newtonian viscosity model for high dry solids content defined in Section 2.1.3. The simulation cases are run over a range of dry solids content to see the affect of non-Newtonian viscosity on the flow hydrodynamics, as shown in Table 5.3.

Table 5.3: Simulations to be run to investigate heat transfer into black liquor.

Case	χ_S	We	V_r	T_{sat} [K]	$T_{\text{liq,in}}$ [K]	$T_{\text{stm,in}}$ [K]	$\dot{m}_{\text{2D}}$ [kg/s m]	Re	h_{inlet} [m]
1	0.5	1.0	1.0	373.0	372.5	376.0	0.34	265	0.0019
2	0.6	1.0	1.0	373.0	372.5	376.0	0.34	10	0.0016
3	0.7	1.0	1.0	373.0	372.5	376.0	0.34	0.6	0.0013

Results for the average breakup location of these simulations is shown in Figure 5.17. As the dry solids content increases, the fluid becomes much more solid-like and the breakup location moves downstream. For the cases of high solids, this has a very pronounced effect.

5.4.3.2 Evaporation Rate

This simulation series uses the previous cases as a baseline and incorporates heat steam to allow for the study of the transport mechanics. The black liquor liquid curtain is modeled with the viscosity determined using the non-Newtonian model for high dry solids content. The thin liquid sheet is surrounded by a confluent envelope of hot steam. This setup is intended to approximate how black liquor could be condensed

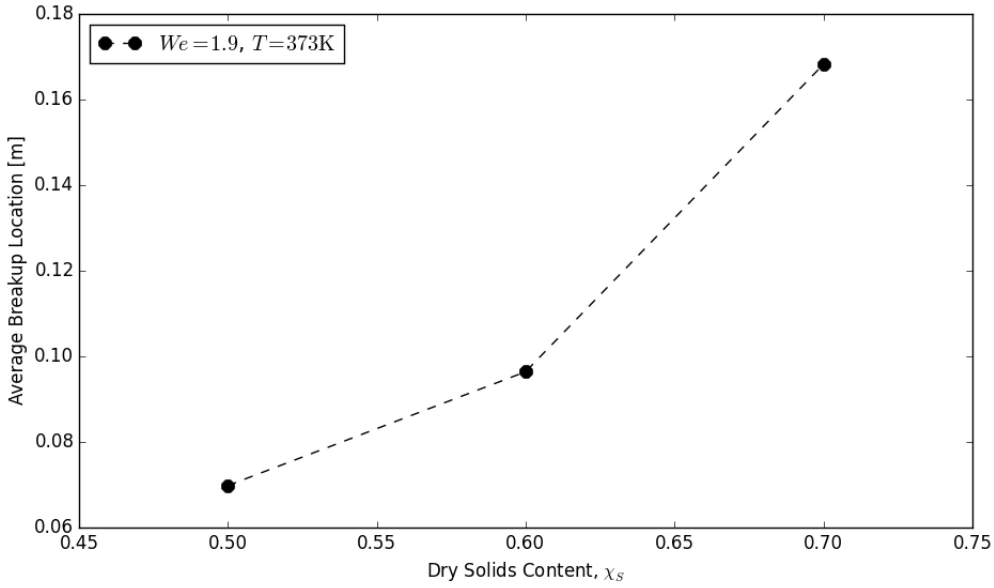

Figure 5.17: Variation of breakup location of black liquor liquid curtain with dry solids content.

in the paper mill. These cases are run over a range of dry solids content to examine the affects of non-Newtonian viscosity on the flow hydrodynamics and the transport mechanics. Details of the simulation parameters are given in Table 5.3.

Results for the averaged evaporation rate of these simulations is shown in Figure 5.18. As the dry solids content increases, the overall level of the evaporation rate decreases. Furthermore, we have seen that as the dry solids content increases, the breakup location increases to a greater extent. With regards to evaporation, this extends the low evaporation region of the domain and delays the location of peak evaporation further downstream.

Figures 5.19, 5.20, and 5.21 show the global mass evaporation rates, steam consumption rates, and steam efficiency for evaporator lengths. Figure 5.19 shows curves for the measured global steam consumption rates as a function of evaporator length for increasing dry solids content. These curves have a very similar shape to the Newtonian liquid curtain simulations, Figure 5.14. For these simulations, increasing the dry solids content has the effect of lowering the global steam consumption rate.

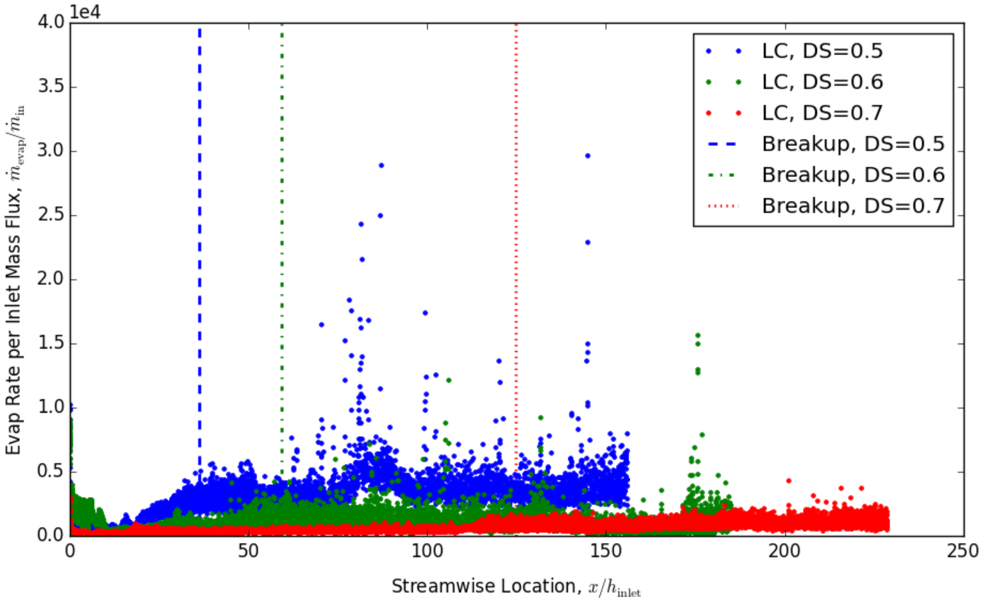

Figure 5.18: Average evaporation rate of black liquor liquid curtain as it varies in the streamwise direction.

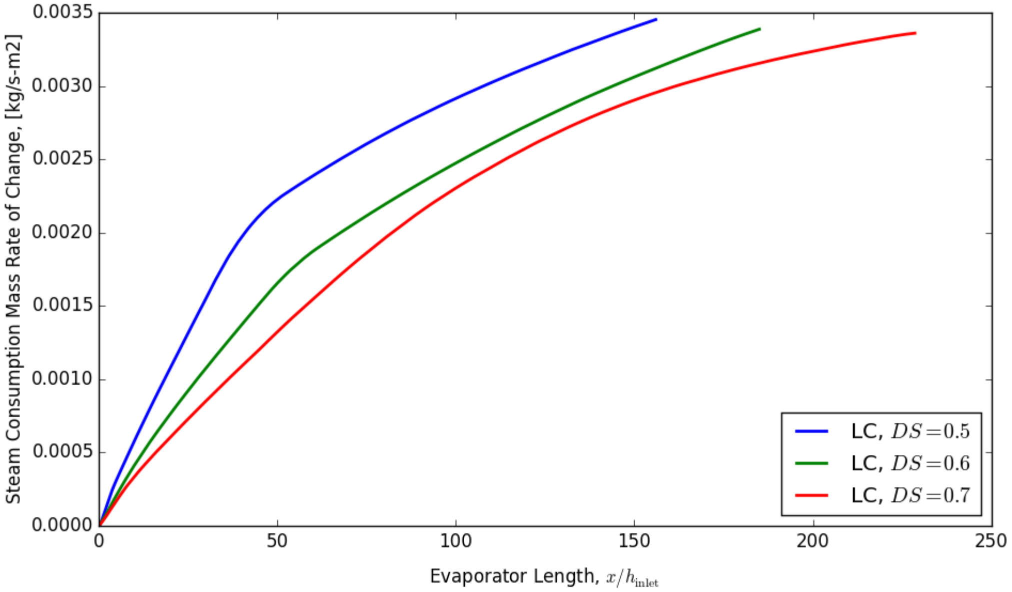

Figure 5.19: Global steam consumption rates for evaporator lengths of increasing size for a black liquor liquid curtain.

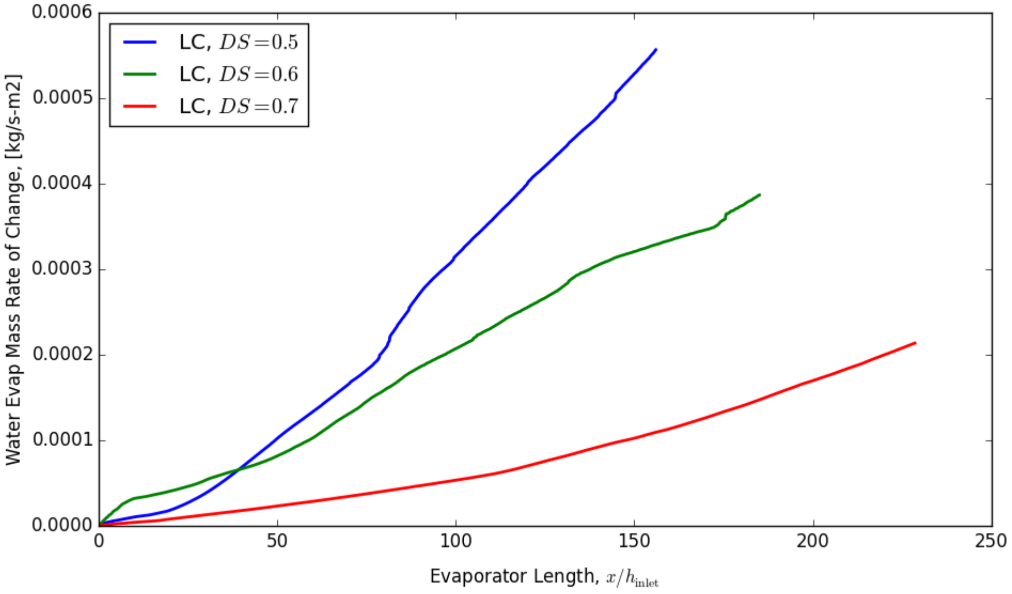

Figure 5.20: Global liquid mass evaporation rates for evaporator lengths of increasing size for a black liquor liquid curtain.

The global liquid evaporation rates with evaporator length for varying dry solids content are shown in Figure 5.20. These curves differ from the Newtonian simulations because there is no entrance length. Instead evaporation is able to occur at the inlet of the domain, although is starts small. As the evaporator length increases, the global liquid evaporator rate is able to increase as well. This effect is strongest for low dry solids content. For high dry solids curtains, increasing the domain length does increase the global mass evaporation rate, but at a much lesser rate. For the Newtonian fluid, it was noticed that the evaporation grew slowly in the liquid curtain, peaked in the region just downstream of the breakup location, and then continued to grow at a slightly faster rate than in the intact liquid curtain. For the black liquor liquid film, as the dry solids content increases, the breakup location is pushed further downstream. The extension of the intact liquid film lessens the benefit the curtain receives from the post breakup evaporation rate increase.

Figure 5.21 shows the steam efficiency as a function of evaporator domain length. Because evaporation is present very near the inlet of the simulations, these curves

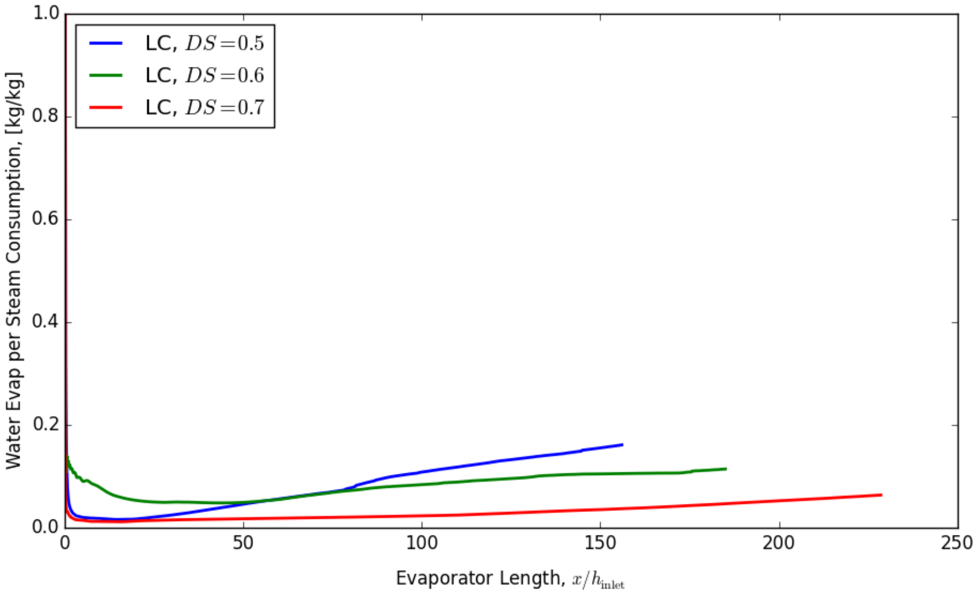

Figure 5.21: Steam efficiency for evaporator lengths of increasing size for a black liquor liquid curtain.

show the steam efficiency decreasing near the inlet an then increasing once the liquid mass evaporator rate increases along the domain length. For high dry solids content, the evaporator length has little effect steam efficiency. The steam efficiency of the evaporator is dominated by the dry solids content. Even at twice the evaporator length, the simulation of 70 % dry solids does not increase its efficiency to the level of the 60 % dry solids simulation.

CHAPTER 6

COMPARISON OF EVAPORATION METHODS

6.1 Background

The basics of the kraft recovery process have remained unchanged since it was introduced in 1884. However, steps in the operation have been refined as the industry has had a need to improve the operation. The current state of the industry has led paper mills to concentrate black liquor in a series of effects. The advantage of multiple effects is steam economy since the steam produced during concentration in one effect can be used at the heat source in the preceding effect. For the purpose of comparison, in this chapter, only one effect is examined. No complicated multiple effects arrangements are considered.

6.2 Evaporator Comparison

The previous two chapters looks at the results for the falling film and curtain separately. In this chapter the results are brought together to determine where the trade-offs are for each evaporation process.

Figure 6.1 shows the evaporation rates along the streamwise direction for Newtonian falling films and a liquid curtain. This is the same data from Sections 4.4.2 and 5.4.2 combined into a single plot for convenience. The evaporation rates for the liquid curtain with varying velocity ratios is similar enough that only one data set is presented here, the case where the velocity ratio $V_r = 1.0$.

The evaporation rates for the falling film clearly exceed the values for the liquid curtain near the end of the domain. However, early in the domain, the liquid curtain is able to achieve evaporation rates that exceed the falling film, because the falling

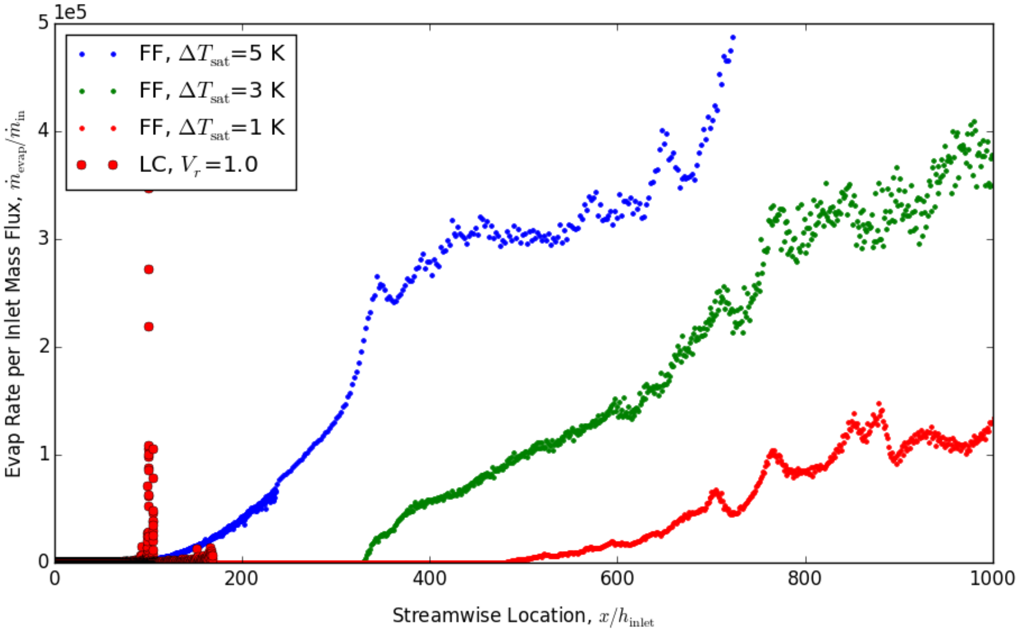

Figure 6.1: Evaporation rate along streamwise direction for falling film and liquid curtain simulations.

film is still in its entrance region where no evaporation is occurring. The liquid curtain is able to have non-zero evaporation rates very near the inlet because heat transfer is occurring at the interface of the liquid curtain.

Comparing the liquid curtain evaporation rate to the cases with wall excess temperature below 3 K, it can be seen that all the evaporation of the liquid curtain occurs before the falling film evaporation rates rise above zero. The evaporation rate entrance region for the falling film could be reduced by driving the wall excess temperature higher, but in practice there is an incentive to keep value low because of the use of multiple effects. The data for Figure 6.1 suggest that evaporation of a Newtonian fluid using a liquid curtain would be advantageous if the there is a need to keep the length small, or if the wall excess temperature for the falling film must be small.

Figures 6.2 to 6.7 show the global steam consumption rate, global mass evaporator rate, or steam efficiency compared to the evaporator length. These are global values

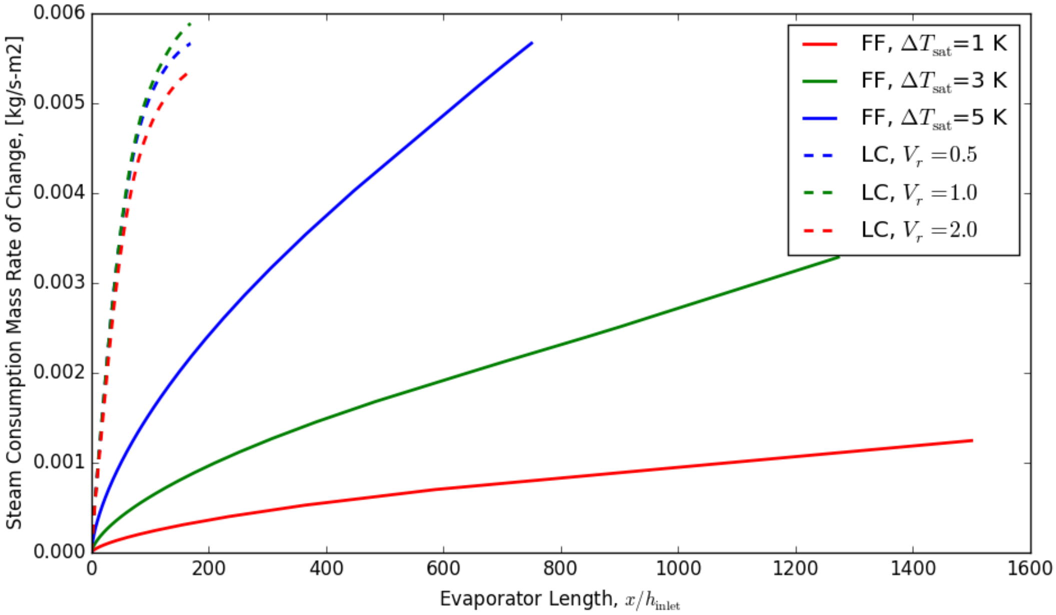

Figure 6.2: Comparison of Newtonian falling film and liquid curtain global steam consumption rates for evaporator lengths of increasing size.

that are calculated cumulatively along the streamwise distance of the simulation domain. The calculated value at each streamwise location is the global value that would be measured in an evaporator of that particular length.

Figure 6.2 shows global steam consumption rate along the normalized evaporator length for Newtonian fluid. The normalized domain for a the liquid curtain is much shorter than for the falling film. Relative to the falling film, the liquid curtains steam consumption rate raises very quickly early in the domain before leveling off.

The global liquid evaporation rate along the normalized evaporator length for Newtonian simulations is shown in Figure 6.3. In terms of magnitude, the global evaporation of the falling film dominates the liquid curtain. However the liquid curtain evaporation rate rises a much shorter distance downstream from the inlet.

Figure 6.4 shows the global evaporation rates for the Newtonian falling films and liquid curtains. From the comparison, the falling film evaporator systems are able to achieve a much higher overall efficiency. With the highest steam efficiency occurring

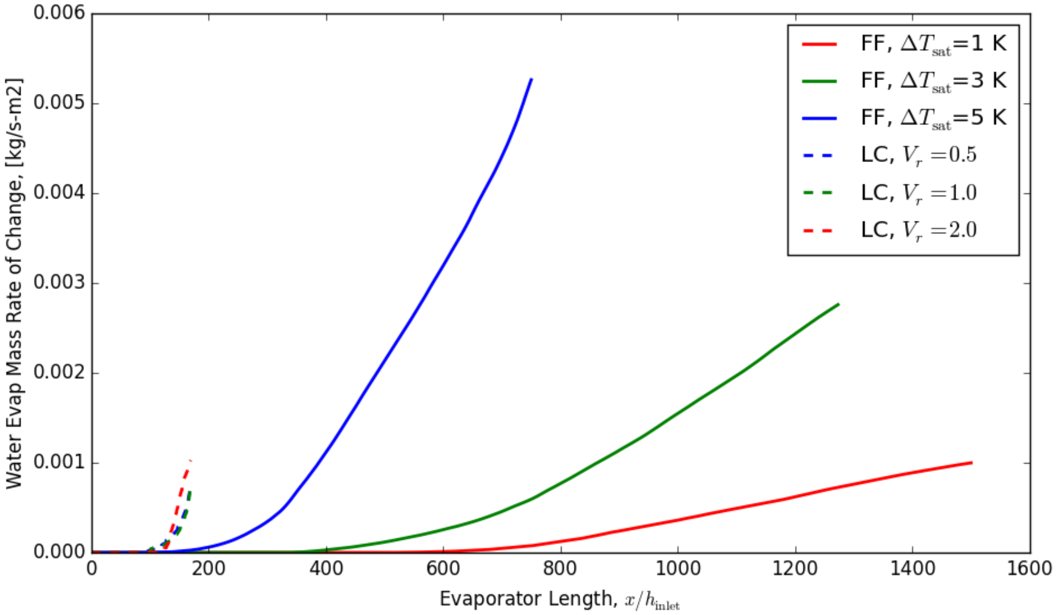

Figure 6.3: Comparison of Newtonian falling film and liquid curtain global liquid mass evaporation rates for evaporator lengths of increasing size.

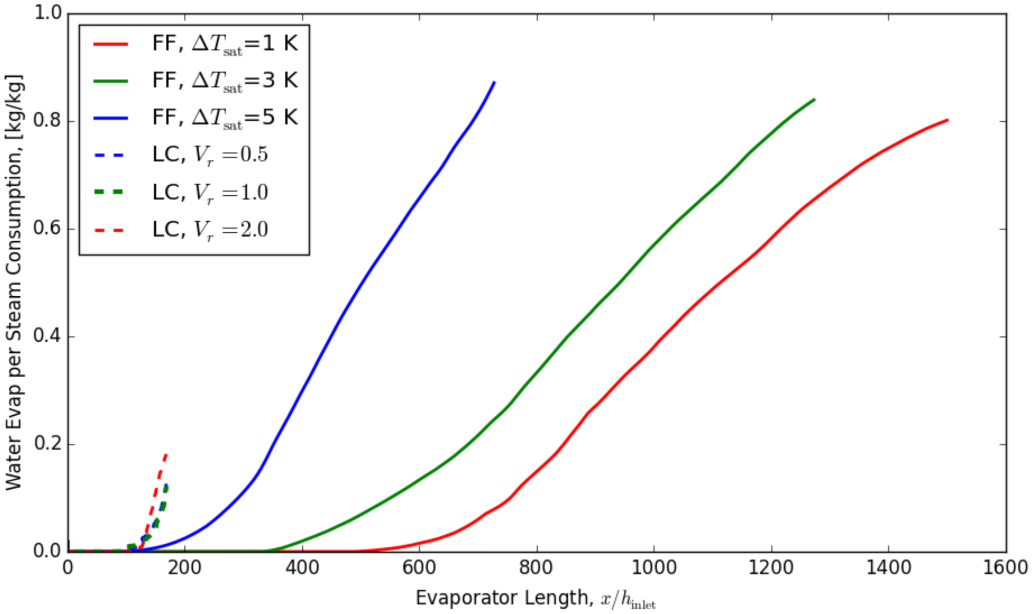

Figure 6.4: Comparison of Newtonian falling film and liquid curtain steam efficiency for evaporator lengths.

in the falling film simulation with a high wall excess temperature of 5 K. Although the liquid curtain simulation has a lower overall steam efficiency, its efficiency increases closer to the inlet than the two lower wall excess temperature falling film simulations. In fact, the curve for steam efficiency between the steam efficiency for the liquid curtain and the most efficient falling film simulation have very similar curves. One would expect that the liquid curtain evaporator domain could simply be extended to achieve a similar steam efficiency curve. However, in this regard, the liquid curtain evaporator is at a disadvantage to the falling film evaporator.

The velocity of a falling film is regulated by the nature of being in contact with the evaporator wall. This means that on average the streamwise velocity of the film will be near the Nusselt film velocity. So, increasing the evaporator domain by doubling its length would double the residence time the film spends in the evaporator. However the liquid curtain has a continuously increasingly streamwise velocity profile, shown in Section 5.3.1, the free fall velocity profile. For typical evaporator lengths used in paper mills and typical film values of water or black liquor, this means that doubling the evaporator length would only increase the residence time of the film in the evaporator by 40 % to 43 %. This makes it challenging to try to achieve the steam efficiencies of the falling film simulations, because the most direct way of increasing time in the evaporator is handicapped.

From the comparison of global steam consumption rate for black liquor simulations in Figure 6.5, it can be seen that the liquid curtain simulation have a much higher steam usage than the calculated values for the black liquor falling film.

The liquid mass evaporation rates for the black liquor simulations is shown in Figure 6.6. Here it can be seen that for short domain lengths, the liquid curtain is able to have much higher rates than the falling film. Figure 6.7 shows comparisons of steam efficiency for black liquor falling film and liquid curtain simulations. From the comparison, the black liquor falling film evaporator systems is still more efficient than

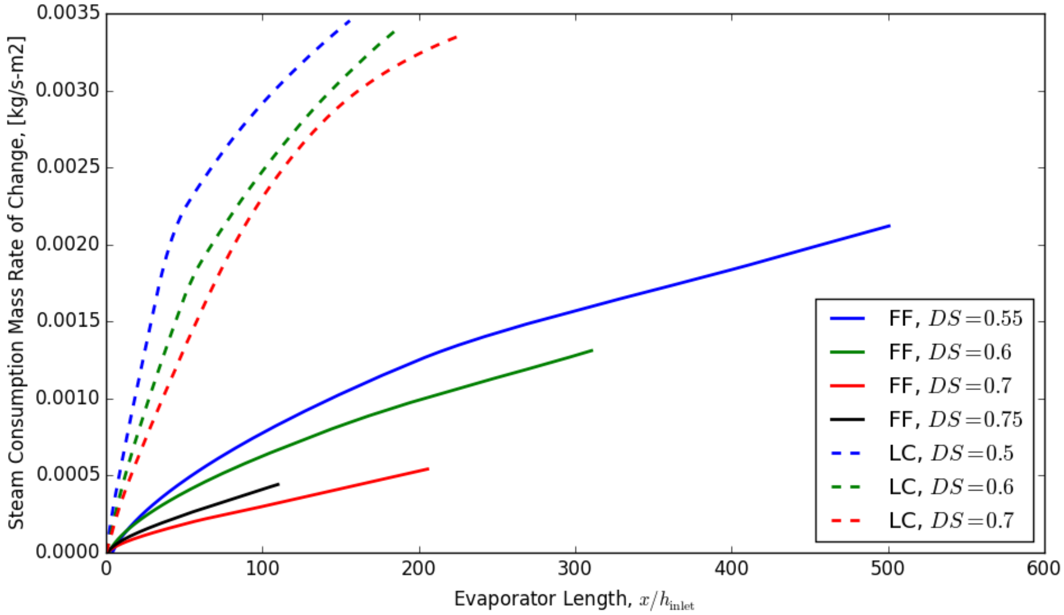

Figure 6.5: Comparison of black liquor falling film and liquid curtain global steam consumption rates for evaporator lengths of increasing size.

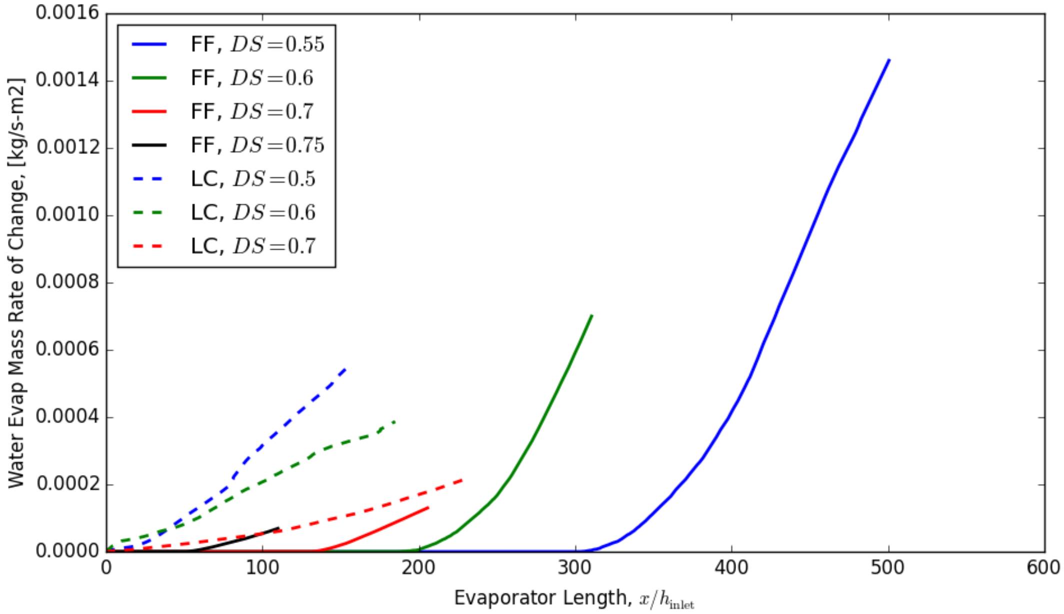

Figure 6.6: Comparison of black liquor falling film and liquid curtain global liquid mass evaporation rates for evaporator lengths of increasing size.

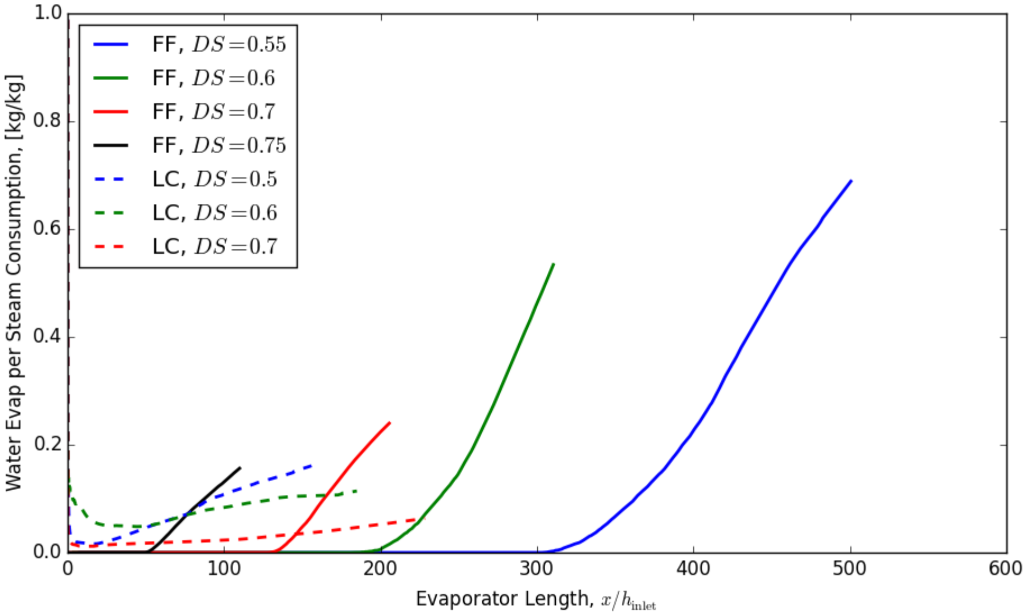

Figure 6.7: Comparison of black liquor falling film and liquid curtain steam efficiency for evaporator lengths.

the falling liquid curtain arrangement among the evaporator lengths tested. However at low dry solids content, the liquid curtain is able to achieve a much higher steam efficiency earlier in the domain than the falling film. At the cost of much steam, the liquid curtain evaporator is able to achieve very high liquid mass evaporation rates compared to the falling film arrangement.

6.3 3-D Effects

The falling film simulations in this study are modeled as a 2-D flow. The thickness of the film is quite small, 0.5 mm to 4 mm, and the diameter of the evaporator pipe is an order of magnitude larger 60 mm. This disparity allows for the assumption to be made that the change in radius between the top and bottom of the film is so small compared to the radius of the pipe that the cylindrical nature of the cross section of the flow can be neglected. And instead, the film is treated as a 2-D flow down a vertical plane.

From previous work it can be estimated that circumferential variations in the hydrodynamics are present as early in the domain as a streamwise distance of 0.67 m for flow of dry solids content 40 % [39]. Falling film simulations in this work are of a domain length up to 1.2 m, so for long simulations there will be some circumferential effect on film interface that is not accounted for by the 2-D nature of theses simulations. Eventually, as the evaporator domain grows in length the effect of fluid flow in the azimuthal direction will begin to effect the films heat transfer and hydrodynamics. It is uncertain what effect this additional component of the hydrodynamics would have on heat transfer and evaporation of the film, whether it would tend to promote or discourage evaporation.

The 2-D liquid curtains in this study are modeled as if there are no changes in the spanwise direction. This is an ideal assumption and will lead to over-predicting the length of the sheet before breakup. In a actual 3-D flow, a perforation that forms in the sheet and it will grow in diameter due to surface tension. This means the perforation will spread along the streamwise and spanwise direction. In the 2-D simulation the portion of fluid modeled lacks the disruption of these growing perforation that might have formed along side the slice of fluid in the spanwise direction. The lack of these disruptions will allow the liquid curtain to reach a longer length before breakup occurs than would have normally be possible.

In addition to perforations, surface tension acting on the far-end spanwise edges will also have a destabilizing influence on the liquid curtains. Ripples that form on the far edge of the sheet grow due to the pull of surface tension and encroach on the inner region of the sheet. In the 2-D simulations, the assumption is made that the slice of fluid being modeled is far away from the With regards to the effectiveness of evaporation as a liquid curtain, it has been shown that evaporation rates are higher downstream of the breakup location than upstream. This means that the 3-D effects, all of which cause the liquid curtain to breakup more quickly, will allow the liquid curtain evaporator to benefit from the enhanced evaporation after breakup for a larger portion of the flow domain.

CHAPTER 7

CONCLUSIONS

7.1 Conclusions

From this work, a computational model has been developed to accurately model the flow structure and transport in the black liquor evaporation process. The goal of this study is to use the computational model to investigate the hydrodynamics and transport phenomena of falling films and liquid curtains. The model has been extended to incorporate the non-Newtonian black liquor properties at dry solids content above 50 %. This study examines: the wave structure and transport for a falling film and falling liquid curtain of Newtonian fluid and non-Newtonian black liquor and the effect the breakup of a falling liquid curtain has on the heat transfer and evaporation. The ultimate purpose of these considerations is to obtain a viable method of condensing black liquor while reducing or eliminating the occurrence of soluble scale formation.

7.1.1 Falling Film Evaporation

From the simulations in the work it was found that the crosswise average temperature for the falling film is inversely related to the film Reynolds number. It was also shown that increasing the forcing frequency had the effect of decreasing the surface temperature of the film. This relationship is likely caused by the proliferation of large humps that form in the film as the forcing frequency increases, and these large humps contain fluid that is far removed from the heat transfer surface. As the forcing frequency increases the number of the large humps increases and stretches of thin film that span these large humps shrink in size. This leads to a larger portion of the fluid interface that is farther away from the heat transfer site.

Evaporation from a falling film evaporator has an entrance length through which no evaporation takes place, after which the evaporation rate can grow very rapidly. The length of the entrance region is inversely related to the wall excess temperature. For higher wall excess temperatures, the heat is able to propagate through the fluid in a shorter streamwise distance and begin the evaporation at the fluid interface. Higher wall excess temperatures also cause a more rapid growth in the evaporation rate. In practice in the paper mill, the use of very high wall excess temperatures is kept in check by the desire to conserve steam.

One surprising result was that the slope for which steam efficiency changed with evaporator length was nearly the same for all three simulations of wall excess temperature. This suggests that attempting to increase the evaporator efficiency by increasing its length is effective but independent of wall excess temperature.

7.1.2 Liquid Curtain Heat Transfer and Evaporation

Simulations of a liquid curtain showed a small evaporation rate that occurred starting at the inlet of the domain. This evaporation rate grew slowly along the streamwise direction and then peaked in the region immediately following the breakup location. After this peak, the evaporation rate reduces to the pre-breakup value and continues to grow along the streamwise direction throughout the rest of the domain.

A key component in evaporator systems is the amount of time the liquid is exposed to the heat transfer source. One of the primary ways of increasing residence time in the evaporator is simply to make the domain longer. In this regard liquid curtains face a significant disadvantage to falling films, because liquid curtains have a continually increasing streamwise velocity while falling films have a regulated streamwise velocity. Increasing the domain length has a diminishing effect on increasing a liquid curtains time in the evaporator. Doubling the length of a falling film evaporator double its residence time, however for a liquid curtain doubling the evaporator length only increases it residence time by about 41 %.

Black liquor liquid curtain simulations with high dry solids content showed a lower evaporation rate along the streamwise direction than liquors with lower dry solids content. This resistance to evaporation probably has two contributing factors. The first is that density increases with dry solids content. This extra density means that high dry solids flows face more resistance to increase the temperature about the saturation value. And secondly, high dry solids flows resist breakup and the liquid curtain remains intact longer in the domain. This decreases the overall evaporation as there is less distance for the liquid curtain to benefit from the higher evaporation rates in the post-breakup region. Liquid curtain breakup enhances evaporation. Delaying that process hampers the evaporative capabilities of the liquid curtain.

7.1.3 Comparison of Evaporation Methods

It is found that, in general, falling film evaporators have a much higher liquid evaporation rate than evaporating as a liquid curtain. However falling film evaporators have an entrance length with no evaporation, and liquid curtains allow for evaporation to start occurring right at the inlet. If reducing length of the evaporator is a priority, liquid curtain evaporators can obtain a higher evaporation rate than falling films within the same distance. Reducing the length of the evaporator may be of interest to paper mills since the main expense of evaporators is cost of their materials.

Broadly, falling film evaporation has a higher steam efficiency than a liquid curtain evaporator. This is true of both Newtonian fluids and black liquor. However, for short evaporator lengths the rate at which water is removed from a liquid curtain evaporator is much greater, but at the cost of a higher steam consumption rate. And in the region of short evaporator lengths, the stream efficiency of a liquid curtain can exceed that of a falling film. For low dry solids flows with short evaporator lengths, falling film and liquid curtain evaporators can have comparable steam efficiency.

For the black liquor falling film simulations, the slope for which steam efficiency of the evaporator grew as the domain of the evaporator increased approached a similar value regardless of dry solids content. In the black liquor liquid curtain simulations this is not the case. Increasing the domain length has a diminishing effect on increasing steam efficiency as dry solids content increases.

The results show that most effective evaporation method is to use falling film evaporators with a long domain and a wall temperature greatly above saturation temperature. However, higher evaporation rates for liquid curtain occur closer to the inlet than falling film due to heat transfer occurring at the evaporation site. But the cost of this higher evaporation rate is a much greater steam consumption. This suggests that liquid curtain evaporators may be of use in the paper mill if the shorter domains allowed by the liquid curtain allow for a reduced materials cost of the evaporator, or if there is a space constraint in the mill. Liquid curtain evaporators may also be effective if the extra steam consumption used by the evaporator is an acceptable trade-off for the higher evaporation rates.

7.2 Future Recommendations

7.2.1 Exploiting Liquid Curtain Breakup

A limited range of operation parameters was discussed in this work. It is possible that differing how the liquid curtain is formed, or changing the arrangement of the steam envelope boundary conditions could drive the breakup location close to the inlet. This would allow the liquid curtain evaporation to take better advantage of the domain length.

Liquid curtain flows are also hampered by their increasing velocity profile due to free fall. This profile means that increasing the streamwise length of domain only increases the film residence time in the evaporator by a fraction. Clever arrangement of the steam inlet boundary condition could be used to increase the aerodynamic drag on the droplets formed by the liquid curtain and thereby increase the liquid residence time in the evaporator.

7.2.2 Falling Film Heated by Steam

One of the key advantages of the liquid curtain is that heat transfer is occurring at the interface which will be the evaporation site. This same effect could be studied for a falling film by using a film that is flowing down a vertical, unheated wall, surrounded by steam. In this arrangement, evaporation could begin to occur at the inlet of the domain, similar to the liquid curtain. However the falling film has a key advantage over the liquid curtain, residence time in the evaporator. Because liquid curtains move at an ever increasing free fall speed, increasing the evaporator length in an effort to increase in residence time in the evaporator has a diminishing effect. The velocity of a falling film is regulated because it is in contact with the stationary wall, so increasing the the evaporator length leads to a proportional increasing in residence time. This line of investigation would also want to determine if scale in black liquor still forms on an unheated wall. And if paper mills could more effectively manage this type of scale, since it would not have any direct negative effects on the heat transfer process.

7.2.3 Crystal Fluid-Solid Interaction

Black liquor is not a homogeneous substance, it contains many type of particles in suspension. The inclusion of solid crystal particles into the film flow would allow for a more accurate picture of the film hydrodynamics by accounting for the forces through the fluid-solid interaction. For the falling film, this information would be important for understanding how crystals in the flow migrate to the heat transfer surface. And determining if any preventative measure could be taken to condition to the flow inhibit salts contacting the evaporator wall. For the liquid curtain, the inclusion of particles in the flow would allow for a more accurate depiction of a black liquor liquid curtain stability. Particles in the film that come in contact with the fluid interface create perforation in the sheet which are known to known to kick off the disintegration process. A major challenge to overcome for this investigation is the difference is scales between the bulk film flow and the flow around a particle in the fluid.

7.2.4 Crystallization Model

The computational model can accurately account for the hydrodynamics and heat transport of the black liquor film. And species enrichment due to evaporation from the liquid film can be described as well. The next direct step is to include an accurate model for the crystallization and dissolution of soluble salts from black liquor experiments. This model could be used to predict precipitation in the film, and will be instrumental for understanding the complex process in the film, such as evaporator surface soluble scale fouling. The ability to predict where salts will form and how they move with the film is key to being able to design evaporators that can reduce scale formation and promote good heat transfer.

REFERENCES

[1] Taylor, G. I. and Howarth, L., "The dynamics of thin sheets of fluid. I. water bells," *Proc. R. Soc. A*, vol. 253, pp. 289–295, December 1959.

[2] Taylor, G., "The dynamics of thin sheets of fluid. II. waves on fluid sheets," *Proc. R. Soc. A*, vol. 253, pp. 296–312, December 1959.

[3] Taylor, G., "The dynamics of thin sheets of fluid. III. disintegration of fluid sheets," *Proc. R. Soc. A*, vol. 253, pp. 313–321, December 1959.

[4] Squire, H. B., "Investigation of the instability of a moving liquid film," *Br. J. Appl. Phys.*, vol. 4, pp. 167–169, June 1953.

[5] Lin, S. P., "Stability of a viscous liquid curtain," *J. Fluid Mech.*, vol. 104, pp. 111–118, 1981.

[6] Lin, S. P. and Roberts, G., "Waves in a viscous liquid curtain," *J. Fluid Mech.*, vol. 112, pp. 443–458, 1981.

[7] Lin, S. P., Lian, Z. W., and Creighton, B. J., "Absolute and convective instability of a liquid sheet," *J. Fluid Mech.*, vol. 220, pp. 673–689, 1990.

[8] Teng, C. H., Lin, S. P., and Chen, J. N., "Absolute and convective instability of a viscous liquid curtain in a viscous gas," *J. Fluid Mech.*, vol. 332, pp. 105–120, 1997.

[9] Spielbauer, T. M. and Aidun, C. K., "Mechanisms of liquid sheet breakup and the resulting drop size distributions. part I," *TAPPI Journal*, pp. 136–142, February 1992.

[10] Spielbauer, T. M. and Aidun, C. K., "Mechanisms of liquid sheet breakup and the resulting drop size distributions. part II," *TAPPI Journal*, pp. 195–200, March 1992.

[11] McCarthy, K. L. and Merson, R. L., "Finite element method to model steam infusion heat transfer to a free falling film," *J. Food Process Eng.*, vol. 11, pp. 43–54, 1989.

[12] Nusselt, W., "Die oberflachenkondensation des wasserdampfes," *Zeitschrift des Vereines Deutscher Ingenieure*, vol. 60, no. 27, pp. 541–546, 1916.

[13] Nusselt, W., "Die oberflachenkondensation des wasserdampfes," *Zeitschrift des Vereines Deutscher Ingenieure*, vol. 60, no. 28, pp. 569–575, 1916.

[14] Nosoko, T. and Miyara, A., "The evolution and subsequent dynamics of waves on a vertically falling liquid film," *Phys. Fluids*, vol. 16, no. 4, pp. 1118–1126, 2004.

[15] Kunugi, T. and Kino, C., "Dns of falling film structure and heat transfer via mars method," *Computers & Structures*, vol. 83, pp. 455–461, 2005.

[16] Brown, D. R., "A study of the behavior of a thin sheet of moving liquid," *J. Fluid Mech.*, vol. 10, pp. 297–305, 1961.

[17] Aidun, C. K., "Mechanics of a free–surface liquid film flow," *J. Appl. Mech.*, vol. 54, pp. 951–954, December 1987.

[18] Spielbauer, T. M. and Aidun, C. K., "The wave-thinning and breakup of liquid sheets," *Transactions of ASME*, vol. 116, pp. 728–734, December 1994.

[19] Bond, W. N., "The surface tension of a moving water sheet," *Proc. Phys. Soc.*, vol. 47, pp. 549–558, April 1935.

[20] Huang, J. C. P., "The break-up of axisymmetric liquid sheets," *J. Fluid Mech.*, vol. 43, no. 2, pp. 305–319, 1970.

[21] Clanet, C. and Villermaux, E., "Life of a smooth liquid sheet," *J. Fluid Mech.*, vol. 462, pp. 307–340, 2002.

[22] Dorman, R. G., "The atomization of liquid in a flat spray," *Br. J. Appl. Phys.*, vol. 3, pp. 189–192, 1952.

[23] Finnicum, D. S., Weinstein, S. J., and Ruschak, K. J., "The effect of applied pressure on the shape of a two-dimensional liquid curtain falling under the influence of gravity," *J. Fluid Mech.*, vol. 225, pp. 647–665, 1993.

[24] Schmid, P. J. and Henningson, D. S., "On the stability of a falling liquid curtain," *J. Fluid Mech.*, vol. 463, pp. 163–171, 2002.

[25] Grand, N. L., Brunet, P., Lebon, L., and Limat, L., "Propagating waves pattern in a falling liquid curtain," *Phys. Rev. E*, vol. 74, no. 2, 2006.

[26] Dombrowski, N. and Jones, W. R., "The aerodynamic instability and disintegration of viscous liquid sheets," *Chem. Eng. Sci.*, vol. 18, pp. 203–214, 1963.

[27] Fraser, R. P., Dombrowski, N., and Rouley, J. H., "The atmoization of a liquid sheet by an impinging air stream," *Chem. Eng. Sci.*, vol. 18, pp. 329–353, 1963.

[28] Hirt, C. W. and Nichols, B. D., "Volume of fluid (vof) method for the dynamics of free boundaries," *J. Comput. Phys.*, vol. 39, pp. 201–225, January 1987.

[29] Hardt, S. and Wondra, F., "Evaporation model for interfacial flows based on a continuum-field representation of the source terms," *J. Comput. Phys.*, vol. 227, no. 11, pp. 5871–5895, 2008.

[30] Rusche, H., *Computational Fluid Dynamics of Dispersed Two-Phase Flows at High Phase Fractions*. PhD thesis, Imperial College of Science, December 2002.

[31] Brackbill, J. U., Kothe, D. B., and Zemach, C., "A continuum method for modeling surface tension," *J. Comput. Phys.*, vol. 100, pp. 335–354, 1992.

[32] Schrage, R. W., *A Theoretical Study of Interphase Mass Transfer*. New York: Columbia University, 1953.

[33] Frederick, W. J., *Kraft Recovery Boilers*, ch. Black Liquor Properties, pp. 61–99. TAPPI Press, 1997.

[34] Zaman, A. and Fricke, A., "Steady shear flow properties of high solids softwood kraft black liquors: effects of temperature, solids concentrations, lignin molecular weight and shear rate," *Chem Eng Comm*, vol. 139, pp. 201–221, 1995.

[35] Zaman, A. A. and Fricke, A. L., "Viscosity of black liquor up to 130 degrees c and 84% solids," *AIChE Forest Prod Sym Proc*, pp. 59–77, 1991.

[36] OpenCFD, *OpenFOAM Programmer's Guide*, 1.7.1 ed., August 2010.

[37] OpenCFD, *OpenFOAM User's Guide*, 1.7.1 ed., August 2010.

[38] Doro, E. O. and Aidun, C. K., "Interfacial waves and the dynamics of backflow in falling liquid films," *J. Fluid Mech.*, vol. 726, pp. 261–284, 2013.

[39] Doro, E. O., *Computational modeling of falling liquid film free surface evaporation*. PhD thesis, Georgia Institute of Technology, 2012.

[40] Dietze, G. F., Al-Sibai, F., and Kneer, R., "Experimental study of flow separation in laminar falling liquid films," *J. Fluid Mech.*, vol. 637, p. 73, September 2009.

[41] Haar, D. T., *Collected Papers of P.L. Kapitza, Vol. 2*. Elsevier Science, 2013.

[42] Alekseenko, S. V., Nakoryakov, V. Y., and Pokusaev, B. G., "Wave formation on a vertical falling liquid film," *AIChE J.*, vol. 31, pp. 1446–1460, September 1985.

[43] Smith, M. K., "The mechanism for the long-wave instability in thin liquid films," *J. Fluid Mech.*, vol. 217, p. 469, 1990.

[44] Johansson, M., Vamling, L., and Olausson, L., "Heat transfer in evaporating black liquor falling film," *Int. J. Heat Mass Transfer*, vol. 52, pp. 2759–2768, May 2009.

[45] Johansson, M., Leifer, I., Vamling, L., and Olausson, L., "Falling film hydrodynamics of black liquor under evaporative conditions," *Int. J. Heat Mass Transfer*, vol. 52, pp. 2769–2778, May 2009.

[46] Chen, F. C. and Gao, Z., "An analysis of black liquor falling film evaporation," *Int. J. Heat Mass Transfer*, vol. 47, pp. 1657–1671, 2004.

[47] Chun, K. R. and Seban, R. A., "Heat transfer to evaporating liquid films," *J. Heat Transfer*, vol. 93, p. 391, 1971.

[48] Alhusseini, A. A., Tuzla, K., and Chen, J. C., "Falling film evaporator of single component liquids," *Int. J. Heat Mass Transfer*, vol. 41, no. 12, pp. 1623–1632, 1998.